FEATURES OF MAGNETO-ABRASIVE MACHINING OF TAPS

Victor MAIBORODA,* Dmytro TARHAN,* Dmytro DZHULII,* Ivanna SLOBODIANIUK*

*Institute of Mechanical Engineering, National Technical University of Ukraine 'Igor Sikorsky Kyiv Polytechnic Institute',
37, Prosp. Peremohy, Kyiv, 03056, Ukraine

maiborodavs@gmail.com, tarakan.com@ukr.net, dmytro.dzhulii@gmail.com, ivannavalentinovna@gmail.com

Abstract: The features of magneto-abrasive machining of taps for metric thread cutting were investigated. The calculation method of integral intensity of the magneto-abrasive machining of the working surfaces of the taps by the quantitative values of normal and tangential components of moving speed of the quasi-stable volumes of the magneto-abrasive tool was developed. Based on the results of calculations, it was possible to predict the probable influence of the taps' location in the working zone on the quality and efficiency of machining their working surfaces. The calculation method is relevant for taps of all diameters with a profile angle of 60°. The working surfaces of the tool would not be effectively machined if the location angle of taps to the plane of the working zone of the machine equals 20–60°. Depending on the expected major polishing or strengthening effect of magneto-abrasive machining, the taps are required to be located at an angle of 60–90° to the plane of the working zone of the machine.

Keywords: Tap, magneto-abrasive machining, cutting tools, machining intensity, polishing effect, strengthening effect

1. INTRODUCTION

Taps are widely used for the formation and machining of an internal metric thread. They are used on different types of machines that provide rotational and translational motions (Patel et al., 2011). However, while using taps, some problems do occur, such problems as rapid wear, teeth chipping, size loss, binding and breakdown of the tool due to inefficient removal of chips, high cutting forces or inadequate strength (Benga et al., 2009; Gultekin and Ihsan, 2016; Pereira et al., 2020; Piska and Sliwkova, 2015; Saito et al., 2016). One of the promising finishing technologies for improving the quality and working capacity of the cutting tool (CT) is magneto-abrasive machining (MAM) (Baron, 2008; Hashimoto et al., 2016; Jain et al., 2007; Mori et al., 2003; Singh et al., 2013; Vahdati and Rasouli, 2016). Investigation of influence of the MAM process on the state of microgeometry of details showed that it is appropriate to use at the final stages of production. This method allows the occurrence of combined influence on the state of the surface layer, controllably change its physical and mechanical properties, microgeometry as the working surfaces and the cutting edges of the tool (Baron, 2008; Denkena et al., 2014; Karpuschewski et al., 2009; Maiboroda et al., 2012a,b, 2017; Olt et al., 2018; Payam et al., 2016; Shadab et al., 2017; Tikal, 2009; Wu et al., 2016; Yamaguchi et al., 2014).

The geometry of working part of the taps, particularly their cutting edges, has a complex space shape. The modes and conditions of MAM of the taps will be significantly different from the machining modes of other cutting tools (Baron, 2008; Denkena et al., 2014; Karpuschewski et al., 2009; Keksin, 2013; Maiboroda et al., 2012, 2017; Maksarov and Keksin, 2018). A great influence on the quality indexes of the tools have features of location of the taps in the working zone of the machine, rotation speed, value of magnetic induction, type and fraction of the magneto-abrasive

powder. Information on the study of influence of the location and rotation speed of taps during MAM process on the intensity and quality of machining their complex surfaces is lacking. The papers Dzhulii and Maiboroda (2008), Jayswal et al. (2005), Keksin (2013), Kim and Choi (1995) and Kwak (2012) give the methodology and certain results of the process simulation and determination of parameters of MAM, which have an influence on the quality of surfaces. Improvement of the calculation methodology, which is aimed at determining the intensity of machining of working surfaces of taps, depending on such parameters as the location in the working zone of the machine and the rotation speed, will allow performing prediction and optimization of the method of MAM of this tool.

The goal of the research is to study the features of MAM of taps in the ring-type working zone and conditions for effective machining of their working surfaces and cutting edges.

2. MATHEMATICAL MODEL OF THE MAM PROCESS OF THE TAPS

The mathematical model of the MAM process of the taps with an angle between the flanks equal to 60 degrees was developed for machines with a circular arrangement of the working area (Maiboroda et al., 2017). The model was developed to determine the probable normal V_n and tangential V_τ components of the moving speed of individual quasi-stable volumes of the magneto-abrasive tool (MAT), which come in contact with machined surface at each investigated point of working part of tap and for identifying specific zones during machining. The diagram of taps' positioning in this type of machine is shown in Fig. 1. On the diagram, p is the angle of mandrel inclination, which is measured in a tangent plane to the plane of the working zone of the machine, q is the angle of

rotation of the mandrel relative to the tangent plane to the ring-type working zone. For the mathematical modelling of the MAM process, we set the following coordinate systems:

− the coordinate system $X_W Y_W Z_W$ is connected with a ring-type working zone and rotates with a frequency ω_W around Z_W axis;

− the coordinate system $X_M Y_M Z_M$ is connected with the mandrel. An axis Z_M is the axis of rotation of the mandrel. This coordinate system rotates around Y_W axis by an angle p, as well as around the vertical axis Z_W by an angle q, which allows inclining the tap by an arbitrary angle in the working zone. The coordinate system $X_M Y_M Z_M$ is offset relative to the vertical axis Z_W of the working zone of the machine by the value of A – the radius of the middle part of the annular working zone;

− the coordinate system $X_T Y_T Z_T$ is connected with the machined tap and rotates at a speed ω_M around the axis Z_M.
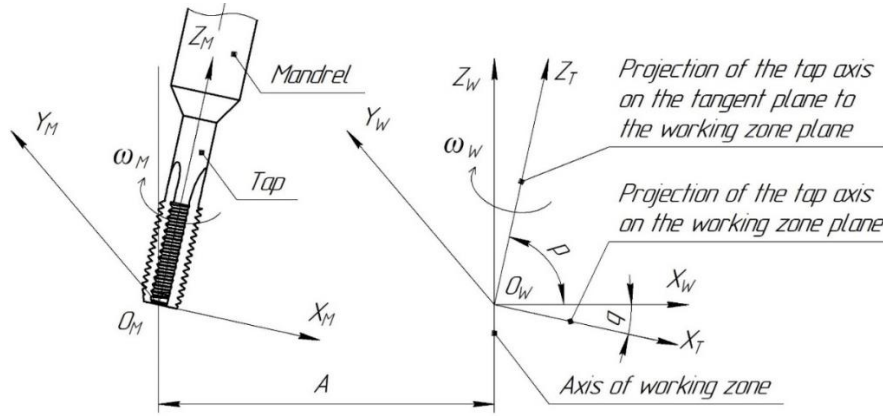

Fig. 1. Diagram of location of coordinate systems in mathematical modelling of the process

For determining the coordinates of a given point P and the direction of the vector of normal N in the coordinate system of the mandrel when the tap is rotated about its own axis by the angle ε, we use the rotation matrix of the vector by the angle $M(\varepsilon)$:

$$\mathbf{M}(\boldsymbol{\varepsilon}) = \begin{pmatrix} \cos\varepsilon & -\sin\varepsilon & 0 \\ \sin\varepsilon & \cos\varepsilon & 0 \\ 0 & 0 & 1 \end{pmatrix} \tag{3}$$

$$\mathbf{P}_M = \mathbf{M}(\boldsymbol{\varepsilon}) \cdot \mathbf{P} \tag{4}$$

$$\mathbf{N}_M = \mathbf{M}(\boldsymbol{\varepsilon}) \cdot \mathbf{N} \tag{5}$$

The coordinates of the given point P and the direction of the vector of normal N in the coordinate system of the annular working zone at the inclination of the mandrel by the angle p and the rotation by the angle q are defined as:

$$\mathbf{M}(\boldsymbol{p}) = \begin{pmatrix} 1 & 0 & 0 \\ 0 & \sin p & -\cos p \\ 0 & \cos p & \sin p \end{pmatrix} \tag{6}$$

$$\mathbf{M}(\boldsymbol{q}) = \begin{pmatrix} \cos q & -\sin q & 0 \\ \sin q & \cos q & 0 \\ 0 & 0 & 1 \end{pmatrix} \tag{7}$$

$$\mathbf{P}_W = \mathbf{M}(\boldsymbol{p}) \cdot \mathbf{M}(\boldsymbol{q}) \cdot \mathbf{P}_M + A \tag{8}$$

$$\mathbf{N}_W = \mathbf{M}(\boldsymbol{p}) \cdot \mathbf{M}(\boldsymbol{q}) \cdot \mathbf{N}_M \tag{9}$$

where $M(p)$ is the matrix of the rotation of the vector by the angle p; $M(q)$ is the matrix of the rotation of the vector by the angle q; A-radius of the annular working zone.

We determine the speed of moving the point around the axis of the annular working zone V_W using the equation:

$$\mathbf{R}_W = \begin{bmatrix} (\mathbf{P}_W)_0 \\ (\mathbf{P}_W)_1 \\ 0 \end{bmatrix} \tag{10}$$

$$\mathbf{V}_W = w_W \times \mathbf{R}_W \tag{11}$$

where R_W is the distance from the given point on the working surface of the tap to Z_W axis of the annular working zone.

We determine the linear speed of moving the point around the axis of the mandrel V_M using the below equation:

$$\mathbf{R}_M = \begin{bmatrix} (\mathbf{P}_M)_0 \\ (\mathbf{P}_M)_1 \\ 0 \end{bmatrix} \tag{12}$$

$$\mathbf{V}_M = \mathbf{M}(\boldsymbol{p}) \cdot \mathbf{M}(\boldsymbol{q}) \cdot (w_M \times \mathbf{R}_M) \tag{13}$$

where R_M is the distance from the point to the mandrel axis Z_M.

The absolute speed of moving of the point V is defined as:

$$\mathbf{V} = \mathbf{V}_W + \mathbf{V}_M \tag{14}$$

The angle β between the vector of speed and the vector of normal to the surface at the concrete point of the working surface is determined as:

$$\beta = \cos^{-1}\left(\frac{\mathbf{V} \cdot \mathbf{N}_W}{|\mathbf{V}| \cdot |\mathbf{N}_W|}\right) \tag{15}$$

Then, the value of normal Vn and tangential $V\tau$ components of the moving speed of quasi-stable volumes of MAT in the investigated point of the working surface of the taps is determined as:

$$V_n = |\mathbf{V}| \cdot \cos\beta \tag{16}$$

$$V_\tau = |\mathbf{V}| \cdot \sin\beta \tag{17}$$

Depending on the direction of the speed vectors of the probable relative movement of the quasi-stable volumes of the MAT, that are in contact with the surface of the taps, a different nature

of their interaction is possible. Namely, there may be either a predominant polishing process, or a process of strengthening the surface layer, or even a machining process may be absent, when the surface of the tool is located in the 'shadow zone'. This occurs when the angle between the normal vector to the surface in which this point or region lies, and the vector of speed V is greater than 90°. Thus, the active components of speed, where $V_n > 0$ and $V_\tau > 0$ can be defined as:

$$V_n act(\varepsilon) = |\mathbf{V}| \cdot \cos(act\beta_n(\varepsilon)) \tag{18}$$

$$V_\tau act(\varepsilon) = |\mathbf{V}| \cdot \sin(act\beta_\tau(\varepsilon)) \tag{19}$$

where $act\beta_n$ and $act\beta_\tau$ are the angles at which the surface is machined effectively. When the angle β is in the range 0–90°, then $act\beta_n$ and $act\beta_\tau$ is equal to it. In other cases, $act\beta_n = \frac{\pi}{2}$, $act\beta_\tau = 0$.
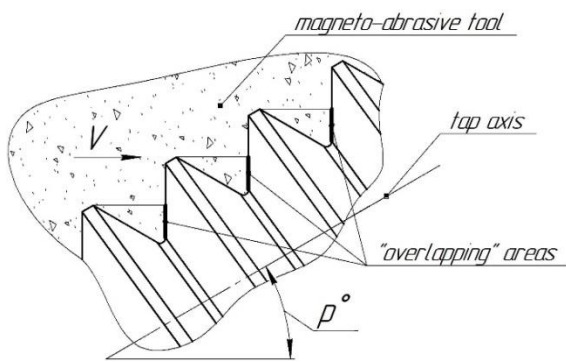

Fig. 2. The zone of 'overlapping' of the cutting edge by the teeth, which located in the front
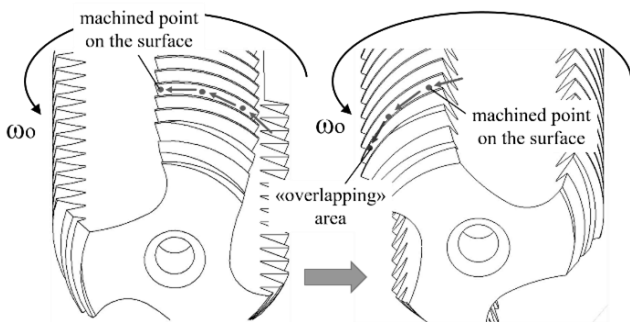

Fig. 3. Pass of the point on the surface to the 'overlapping' area

At the MAM of taps at different angles p to the working zone, there is an effect of 'overlapping' of the tooth and the cutting edge by other teeth, which are located in the front (Fig. 2, 3).

In this zone, there are no $V_n act(\varepsilon)$ and $V_\tau act(\varepsilon)$, so the MAO process is ineffective. To determine the quantitative evaluation of the active normal and tangential components of the speed of the working surfaces of the tap, it is necessary to determine the angles of rotation of the tool around its own axis, at which the zone of 'overlapping' of the machined points of the surface begins and ends. To determine the value of the angle φ of beginning of the 'overlapping', the graphical simulation of the formation of the 'overlapping' zone in the MAM was carried out (Fig. 4).

From the end surface of the tool, the plane P_1 on the figure shows the diameter of tap D and the diameter d along which the studied point of the surface moves. In plane P_2 and $P3$, the above

diameters are represented by graphic modelling at an angle p to the plane of the machine working area. In figure, it is shown that R is the radius of the tooth of the working part of the tap, which overlaps with the next tooth during the machining; r is the radius on the surface of the overlapped tooth, on which is located the investigated point of the surface; a is the distance from the top of the tooth, which overlaps with the plane perpendicular to the tap axis, on which the investigated point is located.

At machining by the angle p to the plane of the working zone, the 'overlap' of the investigated point on the surface begins at the point H_3 and ends at a point, which is symmetrical to H_3 relative to the axis Y_3.

To determine the coordinates of the point of beginning of the 'overlap' H_3 in the $X_3 Y_3$ coordinate system, it is necessary to find the intersection point of the two ellipses. For this purpose, we use the equation of these ellipses:

$$\frac{X_3^2}{R^2} + \frac{(Y_3 + a \cdot \sin p)^2}{(R \cdot \cos p)^2} = 1 \tag{20}$$

$$\frac{X_3^2}{r^2} + \frac{Y_3^2}{(r \cdot \cos p)^2} = 1 \tag{21}$$

Solving the system of equations from (20) and (21), we receive the coordinates of the point of beginning of the 'overlap' in the coordinate system $X_3 Y_3$ and find the coordinates of the point of beginning 'overlap' H_1 in the coordinate system $X_1 Y_1$:

$$X_1 = X_3 \tag{22}$$

$$Y_1 = \frac{Y_3}{\cos p} \tag{23}$$

For finding the angle φ by which it is necessary to rotate the tap so the point of the surface falls into the 'overlapping' area, we find the angle between the axis $\overrightarrow{O_1 Y_1}$ and the vector $\overrightarrow{O_1 H_1}$:

$$\cos\varphi = \frac{\overrightarrow{O_1 Y_1} \cdot \overrightarrow{O_1 H_1}}{|\overrightarrow{O_1 Y_1}| \cdot |\overrightarrow{O_1 H_1}|} \tag{24}$$

$$\varphi = \cos^{-1}\left(\frac{\overrightarrow{O_1 Y_1} \cdot \overrightarrow{O_1 H_1}}{|\overrightarrow{O_1 Y_1}| \cdot |\overrightarrow{O_1 H_1}|}\right) \tag{25}$$

At the MAM, with location of taps by the some angle to the plane of the working area p, the 'overlap' of the machined point of the tooth begins at the tap rotation around its own axis by the definite angle φ and ends when the angle of rotation reaches (360°- φ).

Note that it is necessary to take into account the cases when the system of equations (20, 21) has no solution, that is, when the machined point is always in the 'overlapping' zone or never gets there.

This means that taking into account the presence of the 'shadow zone' and of the 'overlapping' zone, it is possible to determine the active normal and tangential components of the speed of quasi-stable MAT volumes relative to the back surface of the taps. In the investigated point, when the tap rotates at $\varphi \leq \varepsilon \leq (360° - \varphi)$, $V_n act = 0$ and $V_\tau act = 0$, in other cases, the active components are determined by (18, 19).

By determining the nature of the interaction of quasi-stable volumes of MAT with processed elements, we calculate the integral intensity of the machining as a quantitative estimate, which characterize the energy aspect of the interaction of grains and

their groups with the machined surfaces by the values $V_n act(\varepsilon)$ and $V_\tau act(\varepsilon)$. They are defined as the sum of active speeds for a separate component for the point of the machined surface for the complete turn of the tap around its own axes.

According to the calculations of the integral intensity of the machining $V_n act(\varepsilon)$ and $V_\tau act(\varepsilon)$, one can predict the predominant nature of the machining. Therefore, in order to ensure efficient machining, it is necessary to control the ratio between the tangential and normal components of the interaction speed of the MAT with the working surfaces of the taps, which depend on the parameters of the tool location in the machines with the annular arrangement of the working zones.

The calculation method is relevant for taps of all diameters with a profile angle of 60°. The ratio of $V_n act(\varepsilon)$ to $V_\tau act(\varepsilon)$ will be the same regardless of the taps' diameter.
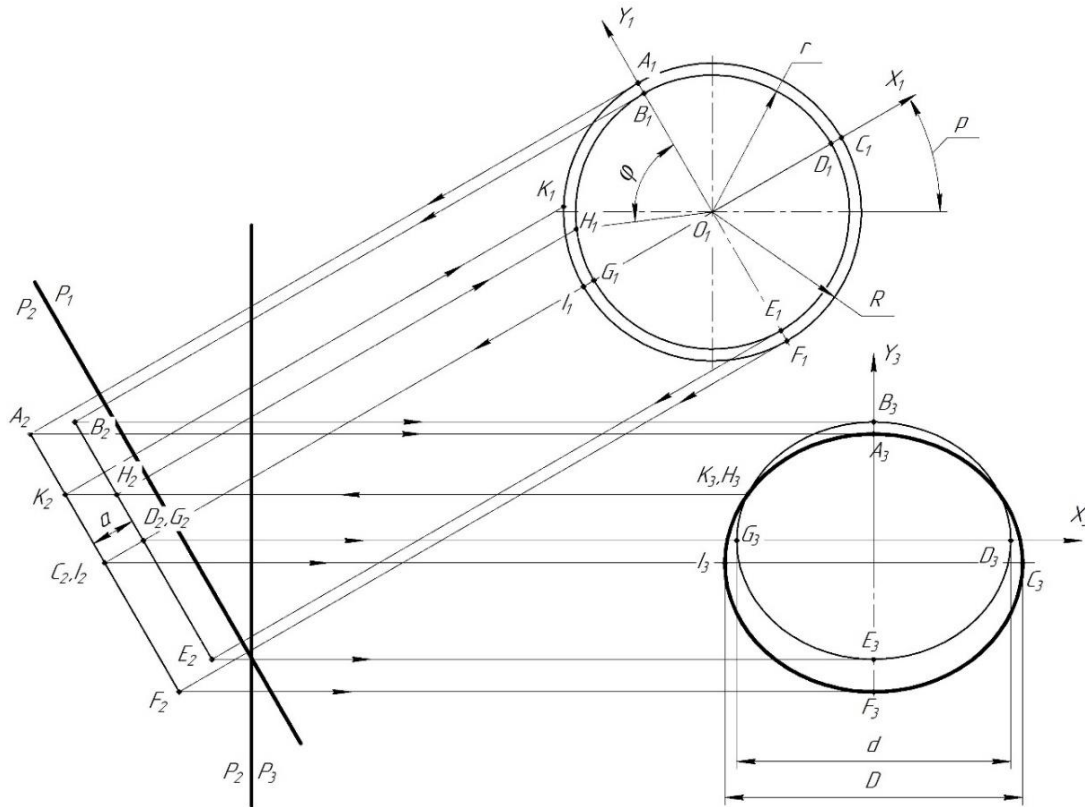

Fig. 4. Graphical diagram for determining the 'overlapping' zone

3. RESULTS OF ANALYTICAL CALCULATIONS

Integral intensities of machining on the back surface of taps M10, made according to DIN 352, at various values of angle *p* were calculated. The points at which were determined the integral intensities of components the machining speed on the back surface are shown in Fig. 5.
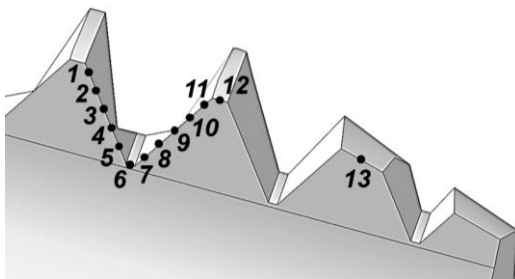

Fig. 5. Points on the cutting edge for which the calculations were made

Points 1–5 and 7–11 are located on the cutting edge of the tooth profile, points 6 and 12 on the cutting edge of the inner and outer diameters of the taps, respectively. Point 13 is located on the cutting edge of the taper lead; therefore, we consider that there is no 'overlapping' zone for this point.

The results of calculations of the integral intensity of the components of the machining speed according to the method described above on the back surface of the working part of the taps in the clockwise rotation mode at different angles of the taps' location to the plane of the working zone are presented in the form of histograms in Fig. 6, 7.

It is shown that effective machining of all surfaces of the working part of the taps occurs at the angle of the tool inclination to the plane of the working zone *p* = 60–90°. That is, the MAM of taps by *p* = 20–60° is not effective, because some of the surfaces are in the 'overlapping' zone where there is no active interaction with the MAT.

For the range of angle *p* = 60–90°, additional calculations of integral intensity were carried out for the full cycle of machining – both in the rotation mode of the taps clockwise and in the opposite direction. The results of calculations are presented in Fig. 8, 9.
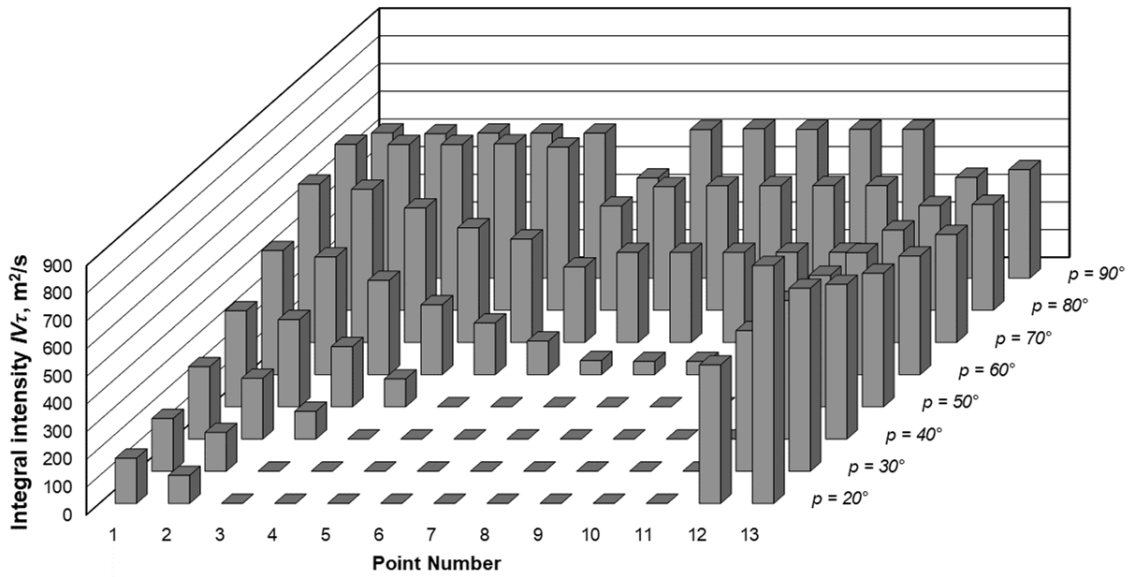
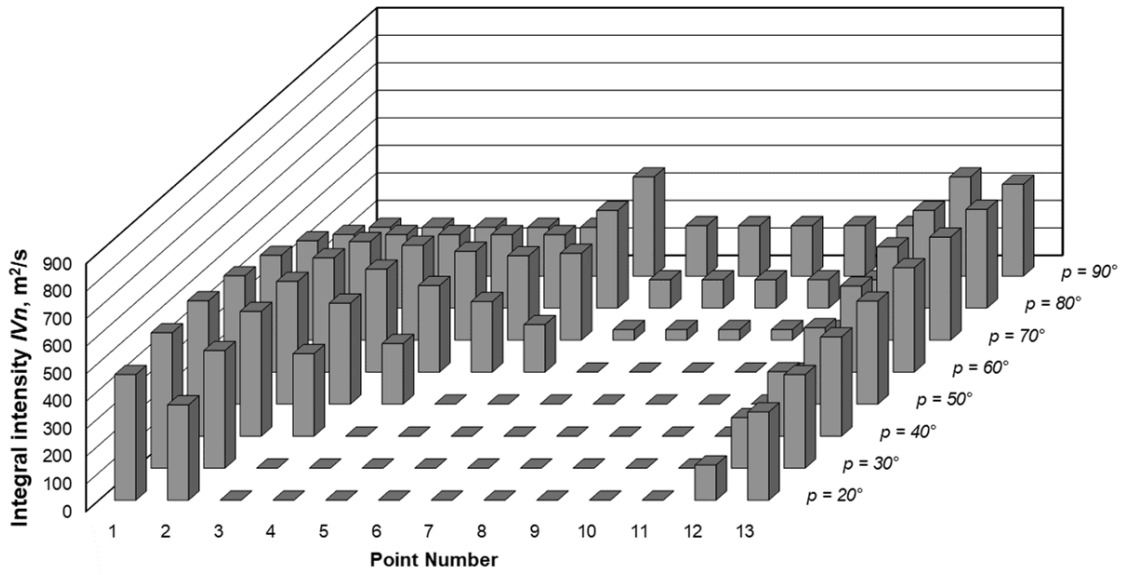**Fig. 6.** Integral intensity of machining IV_τ on the back surface at p = 20–90°

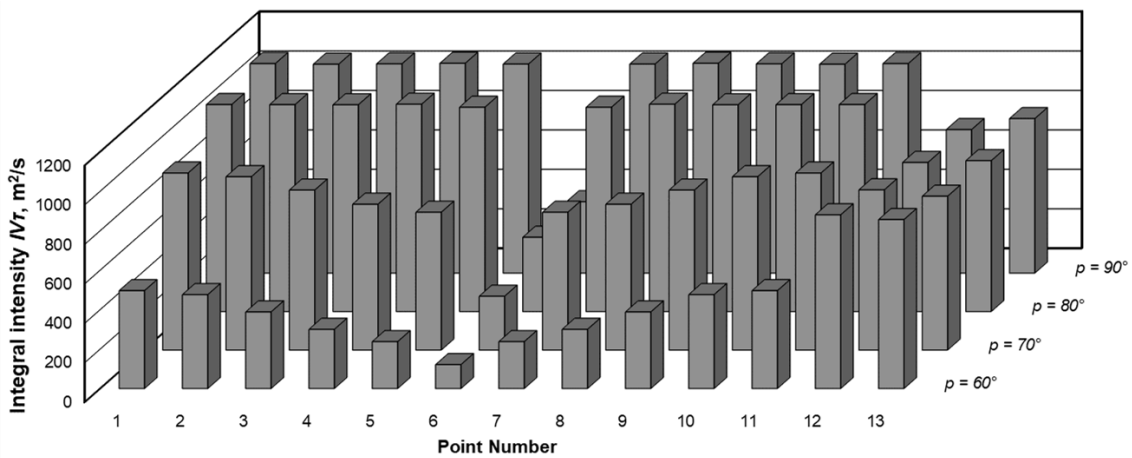**Fig. 7.** Integral intensity of machining IV_n on the back surface at p = 20–90°

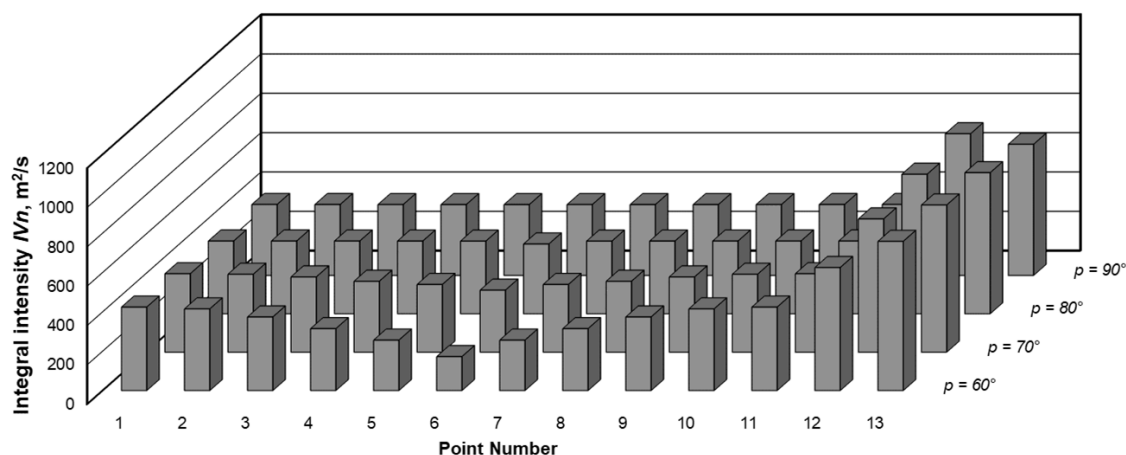**Fig. 8.** Integral intensity of machining IV_τ on the back surface for the full cycle of machining at p = 60–90°

Fig. 9. Integral intensity of machining IV_n on the back surface for the full cycle of machining at p = 60–90°

Figure 10 shows the values of ratios of the integral intensities of processing IV_τ to IV_n at different points of the cutting edge of the taps, depending on the angle p.
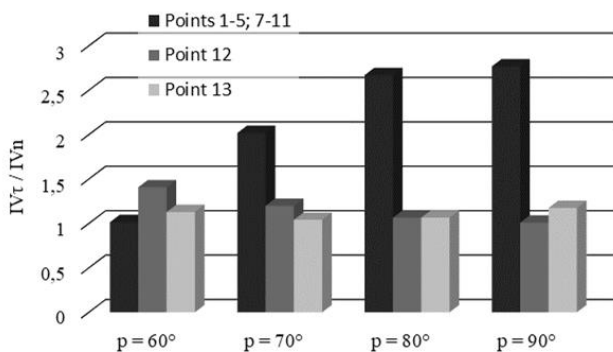

Fig. 10. Average value IV_τ / IV_n

It is established that at p = 60°, equal polishing and strengthening effect of MAT is observed on the flank surfaces of the teeth, and with increasing the angle p, the polishing is prevalent. On the cylindrical surface of the teeth, the polishing effect of the MAT decreases and aligns with the strengthening as the angle p increases. At taper lead, the prevailing polishing interaction of MAT with the surface is observed at p = 60° and p = 90°.

4. CONCLUSIONS

The method of calculating the quantitative assessment of action of the quasi-stable volumes of MAT on the working surfaces of taps during magneto-abrasive machining is developed. The peculiarities of the MAM process of the taps in the conditions of the ring type working zones, depending on the features of their location in the working zone, were determined. It was established that based on the results of calculations, it is possible to predict the probable effect of location of the taps in the working zone on the quality of machining their working surfaces. The calculation method is relevant for taps of all diameters with a profile angle of 60°. It was shown that when taps are located at the angle p = 20–60° to the plane of the working zone, not all surfaces would effectively interact with the MAT. Effective magneto-abrasive machin-

ing of taps is appropriate to perform under conditions of their location at an angle of 60–90° to the plane of the working zone. For receiving the prevalent polishing effect, the inclination angle of the taps should be equal to 80–90°, and for the strengthening, it should be equal to 60–70°.

REFERENCES

1. **Baron Y.M.** (2008), *Finishing, improvement of wearing and hardening using magnetic field*, Create space independent publishing platform, Saint-Petersburg.
2. **Benga G., Ciupitu I., Stanimir A.** (2009), Correlation between cutting forces and tool wear when thread tapping AISI P20 hardened steel. *Annals of DAAAM and Proceedings of the International DAAAM Symposium*, 1753–1754.
3. **Denkena B., Kohler J., Schindler A.** (2014), Behavior of the magnetic abrasive tool for cutting edge preparation of cemented carbide end mills. *Production Engineering – Research and Development*, Vol. 8, 627–633.
4. **Dzhulii D., Maiboroda V.** (2008), Analysis of conditions of magneto-abrasive machining of multisided not sharpened hard-alloy plates at theirs free disposition in the working zones of the ring type machine (in Ukrainian), *Transactions of Kremenchuk Mykhailo Ostrohradskyi national university*, Vol. 48, 27–31.
5. **Gultekin U., Ihsan K.** (2016) The effects of cutting conditions on the cutting torque and tool life in the tapping process for AISI 304 stainless steel, *Materials and technology*, 50, 275–280.
6. **Hashimoto F., Yamaguchi H. et al.** (2016), Abrasive fine-finishing technology. *CIRP Annals - Manufacturing technology*, 65, 597–620.
7. **Jain N.K., Jain V.K., Jha S.** (2007), Parametric optimization of advanced fine-finishing processes. *The International Journal of Advanced Manufacturing Technology*, 34 (11–12), 1191–1213.
8. **Jayswal S.C., Jain V.K., Dixit P.M.** (2005), Modeling and simulation of magnetic abrasive finishing process, *The International Journal of Advanced Manufacturing Technology*, 26, 477–490.
9. **Karpuschewski B., Byelyayev O., Maiboroda V.** (2009), Magneto-abrasive machining for the mechanical preparation of high-speed steel twist drills, *CIRP Annals – Manufacturing Technology*, 58 (1), 295–298.
10. **Keksin A.I.** (2013), Methods of increasing the quality of the thread pitches, *Agronomy Research*, 11 (1), 139–146.
11. **Kim J.D., Choi M.S.** (1995), Simulation for the prediction of surface-accuracy in magnetic abrasive machining, *Journal of Materials Processing Technology*, 53, 630–642.
12. **Kwak J.S.** (2012) Mathematical model determination for improvement of surface roughness in magnetic-assisted abrasive polishing of

nonferrous AISI316 material, *Transactions of Nonferrous Metals Society of China*, 22, 845–850.

13. **Maiboroda V., Dzhulii D., Tkachuk I., Byelyaev O.** (2012a), Magneto-abrasive machining of end-cutting tool in a large magnetic gaps with using the restore elements, *Scientific journal of the Ternopil State Technical University*, 4 (68), 133–141.

14. **Maiboroda V., Slobodyanyuk I., Dzhuliy D.** (2017), *Magneto-abrasive machining of parts with complex shapes (in Russian)*, «Ruta» Publ., Zhitomir.

15. **Maiboroda V., Tkachuk I., Minitska N., Dzhulii D.** (2012b), Magneto-abrasive machining drills of high-speed steel, *Reliability of the tool and optimization of technological systems*, 31, 271–279.

16. **Maksarov V.V., Keksin A.I.** (2018) Technology of magnetic-abrasive finishing of geometrically-complex products, *IOP Conference Series-Materials Science and Engineering*, 327, Article Number: UNSP 042068.

17. **Mori T., Hirota K., Kawashima Y.** (2003), Clarification of magnetic abrasive finishing mechanism. *Journal of Materials Processing Technology*, 143–144, 682–686.

18. **Olt J., Maksarov V., Keksin A.** (2018) Internal thread cutting process improvement based on cutting tools treatment by composite powders in a magnetic field, *Journal of Silicate Based and Composite Materials*, 70, 128–131.

19. **Patel H.J., Patel B.P., Patel S.M.** (2011), A review on thread tapping operation and parametric study, *International Journal of Engineering Research and Applications*, 2, 109–113.

20. **Payam S., Hamid S.M., Bahram M.** (2016) Study of magnetic abrasive finishing for AISI321 stainless steel, *Materials and Manufacturing Processes*, 31 (15), 2023–2029

21. **Pereira I.C., Vianello P.I., Boing D.** (2020) An approach to torque and temperature thread by thread on tapping, *The International Journal of Advanced Manufacturing Technology*, 106, 4891–4901.

22. **Piska M., Sliwkova P.** (2015) Surface parameters, tribological tests and cutting performance of coated HSS taps, *Procedia Engineering*, 100, 125–134.

23. **Saito Y., Takiguchi S., Yamaguchi T.** (2016) Effect of friction at chip-tool interface on chip geometry and chip snarling in tapping process, *International Journal of Machine Tools and Manufacture*, 107, 60–65.

24. **Shadab A., Swati G., Prabhat Chand Y., Singh D.K.** (2017), Optimization of process parameters affecting surface roughness in magnetic abrasive finishing process, *Materials and Manufacturing Processes*, 32(15), 1723–1729.

25. **Singh D. K., Jayswal S.C., Jain, V.K.** (2013) Magnetic abrasive finishing (MAF), *Micromanufacturing processes*, Chapter 8, 155-182.

26. **Tengyun C., Sutherland J.W.** (2002), Investigation of thread tapping load characteristics through mechanistic modelling and experimentation, *International Journal of Machine tools and Manufacture*, 42, 1527–1538.

27. **Tikal F.** (2009), *Cutting edge processing. Objectives, process and measurement methods. Reports from industry and research (in German)*, Kassel University Press GmbH, Kassel.

28. **Vahdati M., Rasouli S.A.** (2016) Study of magnetic abrasive finishing on freeform surface, *Transactions of the Institute of metal finishing*, 94, 294–302.

29. **Wu J., Zou Y., Sugiyama H.** (2016), Study on finishing characteristics of magnetic abrasive finishing process using low-frequency alternating magnetic field, *The International Journal of Advanced Manufacturing Technology*, 85, 585–594.

30. **Yamaguchi H., Srivastava A., Tan M., Hashimoto F.** (2014), Magnetic abrasive finishing of cutting tools for high-speed machining of titanium alloys, *CIRP Journal of Manufacturing Science and Technology*, 7(4), 299–304

Andrzej Koszewnik
Experimental Validation of Equivalent Circuit Modelling of the Piezo-Stripe Harvester Attached to the SFSF Rectangular Plate

DOI 10.2478/ama-2020-0002

EXPERIMENTAL VALIDATION OF EQUIVALENT CIRCUIT MODELLING
OF THE PIEZO-STRIPE HARVESTER ATTACHED TO THE SFSF RECTANGULAR PLATE

Andrzej KOSZEWNIK*

*Faculty of Mechanical Engineering, Department of Robotics Systems and Mechatronics, Wiejska 45C, 15-351 Białystok, Poland

a.koszewnik@pb.edu.pl

Abstract: Plate-like structures with attached piezo-patch elements are widely used in marine, aerospace and civil infrastructure applications to power small devices with low power demand or used for monitoring of vibration structures. In order to assess the feasibility of an energy harvesting system to generate power output from a harvester, an accurate electromechanical model of the piezo-patch harvester attached to a 2D structure in modal coordinates is required. Taking into account this fact, this study is focused on the analysis of the piezo-harvester orientations on the SFSF (Simply Supported-Free-Simply Supported-Free) plate undergoing forced dynamic excitation. The results obtained from the numerical analysis of a smart structure led to determining quasi-optimal piezo-harvester location on the structure, and next, to determining a multi-mode representation of the equivalent circuit model. The experimental set-up carried out on the lab stand properly verified the parameters of the ECM model. Finally, the proposed approach can be used for the structural health monitoring of vibration of some 2D mechanical structures like the front wall of a dishwasher.

Keywords: Aluminium plate, piezo-harvester, energy harvesting system, modal analysis, Equivalent Circuit Model (ECM)

1. INTRODUCTION

The number of applications of self-powered wireless sensors and health monitoring systems has been growing increasingly because the external power requirement has reduced to the micro-watt range in the past two decades (Koszewnik, 2019; Hu and Zhang, 2011). As a result, vibration-based energy harvesting systems have become a promising approach to provide constant power supply of low power electronics (Roundy et al., 2003). Taking into account the scope of some references, it is well known that this effect can be achieved by using different types of transduction mechanisms like electromagnetic (Naifar et al., 205; A,nrożiewicz et al., 2020), electrostatic (Chiu and Tseng, 2008; Lee et al., 2009), magnetostrictive (Wang and Yuan, 2008) and piezoelectric (Okosun et al., 2019; Koszewnik and Wernio, 2016). However, only piezoelectric energy harvesting transducers have drawn more attention due to the ease of their fabrication and the possibility to be applied in microsystems and macroscale devices (Cook-Chennault et al., 2007).

Generally, the piezoelectric energy harvesting systems are strongly focused on analysing 1D structures with piezo-ceramic layers, due to the fact that they are easy to model and implement (Borowiec, 2015). For this reason, analytical and numerical models of cantilever beams with a perfectly bonded piezo-harvester have been extensively developed by several research groups. For instance, analytical distributed–parameter modelling of beams for chaotic vibration with experimental set-up were presented in reference (Litak et al., 2009), while modelling of a self-resonating energy harvester system of cantilever beams with identification and experimental investigations in Aboulfotoh et al. (2017). In other practical implementations, the EH system is used to monitor water pipes as a novel technology for leak detection (Okosun et al., 2019).

As compared to the number of studies dealing with piezoelectric harvester beams, research on 2D structures with an attached piezoceramic patch harvester is very limited (Gosiewski, 2008). For instance, Marqui presented an electromechanical finite element model for a PEH embedded in a cantilever plate, and later on extended this model with airflow excitation problems by electroelastic coupling for energy harvesting from aeroelastic flutter (De Marqui, 2011). We have found a similar application in the paper published by Anton, who was the first to design and investigate novel piezoelectric devices installed on UAV platforms. For instance, the author in reference (Anton Nove, 2019) showed a piezoelectric patch with a thin-film battery as a multifunctional self-charging device for scavenging energy. Later, the same author presented a hybrid device, containing piezo-electric stripes, macro-fibre and piezo-fibre composites, that allows harvesting energy from wing vibrations (Anton, 2011).

The results obtained in these investigations led to further development of this research area and their applications for civil structures. For instance, Harne modelled electroelastic dynamics of a vibrating panel with a corrugated piezoelectric spring and then analysed this corrugated harvester device by attaching it to a panel of public bus (Hantre, 2012, 2013). In other papers, authors used vibration energy harvesting devices for monitoring a full-scale bridge as a 2D structure undergoing forced dynamic vibrations generated by vehicle or passenger trains going over them (Cahill et al., 2014,2018). An additional advantage of this is the fact that the harvested energy can be used to sufficiently power other small devices with low power demand.

The results obtained from the above papers and monitoring of civil infrastructure (bridge) by using longitudinally located piezo

harvesters gave motivation to analyse the harvester locations and orientations on the structure and assess the energy harvesting system effectiveness. In order to do this, firstly, the mechanical strains of the structure considered in this paper were analysed for two perpendicular directions. This allowed to indicate the best piezo-harvester locations and orientations on the structure and determine the electromechanical model of the whole structure. Additionally, the experimental test carried out on the lab stand allowed to verify the numerical results and showed that this approach can be used to assess voltage generating by the piezo-harvester. As a result, the proposed approach enables exploiting the harvesting capabilities of the piezoelectric patch-based harvester attached to a thin rectangular plate with any linear and nonlinear electrical components. Moreover, multi-vibration mode equivalent circuit model of the PZT patch-based harvesters, determined in this way, also allow to simplify the optimization pro-

cess of these systems in order to maximize the power output. As a result, the proposed approach filled the gap in modelling EH systems for 2D structures, and it enables designing structural health monitoring systems of some structures, like dishwashers.

2. ANALYTICAL DISTRIBUTED PARAMETER MODEL OF SFSF PLATE WITH HARVESTER

The analytical distributed-parameter model of the SFSF plate with a perfectly bonded piezo patch harvester is presented in this Section. For this purpose, all parameters of the whole smart structure are firstly collected in Tab. 1, and then, the model of this structure based on the parameters and by using the Kirchhoff's plate theory is determined.
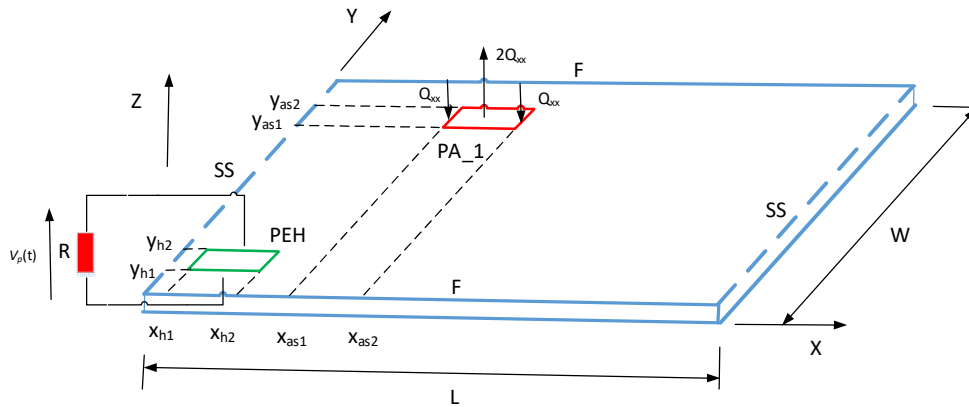

Fig. 1. The host plate with piezo-patches working as a harvester (PEH) and actuator – PA_1

Tab. 1. Parameters of the host structure and piezo-stripes (Koszewnik, 2016)

Parameter	Plate		Piezo-element	Actuator QP20N	Harvester V21BL
Length [m]	L	0.4	l_p / l_{peh}	0.05	0.048
Width [m]	W	0.2	w_p / w_{peh}	0.025	0.0125
Thickness [m]	h_{plate}	0.0002	h_a / h_{peh}	0.000782	0.000787
Young module [GPa]	E_b	70	E_p	0.18	0.18
Density [kg/m³]	ρ_{plate}	2720	ρ_p	7200	7200
strain constant of piezo [pm/V]	-	-	d_{33}	-125	-
piezoelectric stress/charge constant [pC/m²]	-	-	e_{31}	-	-6.5

As it can be seen in Fig. 1, the plate is excited to vibrations by the piezo actuator covering the surface of the plate at corners (xas1,yas1) and (xas2,yas2). As a result, the whole plate is excited to vibration by the bending moment Mx(x,y) at the position of the actuator. The piezo-harvester (PEH) with the length of (l_{peh}), the width of (w_{peh}) and the thickness of (h_{peh}), was additionally integrated with the structure at the positions (xh1,yh1) and (xh2, yh2) in order to measure voltage from the vibrations. As a result, by assuming an external electrical load (a resistive load R), and the piezo-stripe element coupling with the host structure only electromechanically, the transverse vibration of the smart plate can be expressed in the following form (De Marqui, 2011):

$$D\left(\frac{\partial^4 w(x,y,t)}{\partial x^4} + 2\frac{\partial^4 w(x,y,t)}{\partial x^2 y^2} + \frac{\partial^4 w(x,y,t)}{\partial x^4}\right) + c\frac{\partial w(x,y,t)}{\partial t} + \rho_{peh}h_{peh}\frac{\partial^2 w(x,y,t)}{\partial t^2}$$

$$-\Gamma V_p(t)\left\{\begin{matrix}\left[\dfrac{d\delta(x-x_{h1})}{dx} - \dfrac{d\delta(x-x_{h2})}{dx}\right] \times [H(y-y_{h1}) - H(y-y_{h2})] + \\ \left[\dfrac{d\delta(y-y_{h1})}{dy} - \dfrac{d\delta(y-y_{h2})}{dy}\right] \times [H(x-x_{h1}) - H(x-x_{h2})]\end{matrix}\right\} = \left[\frac{\partial^2 M_X(x,y)}{\partial x^2}\right] \qquad (1)$$

where h_{peh} denotes the thickness of the harvester, ρ_{peh} – the density of the harvester, D – the flexural rigidity of the considered plate, δ(x), δ(y) – the Dirac delta function along the X and Y axes, respectively, Vp(t) – voltage across the external resistive load R, while Γ – the electromechanical coupling term ($\Gamma = e_{31}(\frac{h_{plate}+h_{pe}}{2})$).

sciendo

Andrzej Koszewnik
Experimental Validation of Equivalent Circuit Modelling of the Piezo-Stripe Harvester Attached to the SFSF Rectangular Plate

DOI 10.2478/ama-2020-0002

The considered plate, according to Fig. 1, has two simply supported edges oriented longitudinally to the Y axis whose boundary conditions are written in Eq. (2). As a result, considering these conditions, the eigen vectors of this structure are determined and expressed as:

$$w(x,y) = 0; \quad \frac{\partial^2 w(x,y)}{\partial x^2} + v\frac{\partial^2 w(x,y)}{\partial y^2} = 0; \qquad (2)$$
for $x = 0, L$

$$w(x,y) = \Theta_i \left[\begin{pmatrix} A_i ch\alpha_i y + B_i sh\alpha_i y + \\ C_i \alpha_i ch\alpha_i y + D_i \alpha_i sh\alpha_i y \end{pmatrix} \sin\alpha_i x \right] \qquad (3)$$

where: $\alpha_i = \frac{i\pi}{L}$, i is i-th mode shape, A_i, B_i, C_i, D_i - the coefficients of the vertical deflection individually determined for each mode shape, Θ_i - the modal amplitude constant.

Next, substituting the obtained Eq. (3) for Eq. (1) led to solving the eigenvalue problem of the smart plate for short circuit conditions (R→0). Then, the natural frequency ω_{mn} of the structure is simplified to the following form:

$$\omega_{mi} = \omega_i = \frac{\lambda_i \pi^2}{L^2}\sqrt{\frac{D}{\rho_p h_p}} \qquad (4)$$

where: λ_i is the frequency parameter of an undamped plate.

From the energy harvesting system point of view, determining the differential equation of the coupled circuit dynamics is also an important step. For this purpose, the constitutive equation that governs the electrical circuit of the system has the following form:

$$C_p \frac{dV_p(t)}{dt} + \frac{V_p}{R} + \Gamma \left[\int_{y_{h1}}^{y_{h2}} \int_{x_{h1}}^{x_{h2}} \left(\frac{\partial^3 w(x,y,t)}{\partial x^2 \partial t} + \frac{\partial^3 w(x,y,t)}{\partial y^2 \partial t} \right) dxdy \right] = 0 \qquad (5)$$

where the capacitance of the piezo-patch is defined as:

$$C_p = \frac{\bar{\varepsilon}_{33}(x_{h2}-x_{h1})(y_{h2}-y_{h1})}{h_{peh}} \qquad (5a)$$

By following the modal analysis procedure for Eq. (1) and Eq. (5), the electromechanically coupled ordinary differential equations of a 2D structure in modal coordinates can be written as:

$$\frac{d^2\eta_{mi}(t)}{dt^2} + 2\xi_{mi}\omega_{mi}\frac{d\eta_{mi}(t)}{dt} + \omega^2_{mi}\eta_{mi}(t) - \tilde{\Gamma}_{mi}v(t) = f_{mi}(t)_1 \qquad (6a)$$

$$C_p \frac{dV_p(t)}{dt} + \frac{V_p(t)}{R} + \sum_{m=1}^{\infty}\sum_{n=1}^{\infty} \tilde{\Gamma}_n \frac{d\eta_{mi}(t)}{dt} = 0 \qquad (6b)$$

where: ω_{mi} – the undamped short circuit of natural frequency for *mith* vibration mode, ξ_{mi} – the modal damping ratio, $f_{mi}(t)_1$ – the modal force derived from the piezo-actuator, $\tilde{\Gamma}_i$ – the modal electromechanical coupling term.

Then, both modal electromechanical coupling term and modal excitation force given by Eq. (6a) for the considered SFSF plate are expressed in the form:

$$\tilde{\Gamma}_i = \Gamma \left[\int_{y_{h1}}^{y_{h2}} \frac{\partial\phi_i(x,y)}{\partial x}\bigg|_{x_{h1}}^{x_{h2}} dy + \int_{x_{h1}}^{x_{h2}} \frac{\partial\phi_i(x,y)}{\partial y}\bigg|_{y_{h1}}^{y_{h2}} dx \right] \qquad (7)$$

$$f_{mi}(t)_1 = f_i(t)_1 =$$

$$\int_0^W \int_0^L f(t)\delta(x - x_{as1})\delta\left(y - \frac{y_{as2} - y_{as1}}{2}\right)\phi_i(x,y)dxdy +$$

$$\int_0^W \int_0^L f(t)\delta(x - x_{as2})\delta\left(y - \frac{y_{as2} - y_{as1}}{2}\right)\phi_i(x,y)dxdy +$$

$$2\int_0^W \int_0^L f(t)\delta\left(x - \frac{x_{as2} - x_{as1}}{2}\right)\delta\left(y - \frac{y_{as2} - y_{as1}}{2}\right)\phi_i(x,y)dxdy \qquad (8)$$

Further analysis of the plate with integrated piezo-stripes in modal coordinates (Eq. (6a) and Eq. (6b)) leads to calculating the steady-state voltage response V(t) through the resistive load R expressed as:

$$V_p(\omega)$$
$$= \frac{-j\omega \sum_{m=1}^{N}\sum_{i=1}^{N} \frac{C\tilde{\Gamma}_i}{\omega_{mi}^2 + 2j\xi_{mi}\omega_{mi}\omega - \omega^2}}{j\omega C_p + \frac{1}{R} + \sum_{m=1}^{N}\sum_{i=1}^{N} \frac{j\omega\tilde{\Gamma}_i^2}{\omega_i^2 + 2j\xi_{mi}\omega_{mi}\omega - \omega^2}} \qquad (9)$$

where:

$$C = F_0\phi_i\left(x_{as1}, \frac{y_{as2} - y_{as1}}{2}\right) + F_0\phi_i\left(x_{as2}, \frac{y_{as2} - y_{as1}}{2}\right)$$

$$-2F_0\phi_i\left(\frac{x_{as2} - x_{as1}}{2}, \frac{y_{as} - y_{as1}}{2}\right) + F_0\phi_i\left(\frac{x_{as4} - x_{as3}}{2}, y_{as3}\right) +$$

$$F_0\phi_i\left(\frac{x_{as4} - x_{as3}}{2}, y_{as4}\right) - 2F_0\phi_i\left(\frac{x_{as4} - x_{as3}}{2}, \frac{y_{as4} - y_{as3}}{2}\right)$$

3. FINITE ELEMENT MODEL

The numerical investigations of a rectangular aluminium plate with piezo-elements (harvester and actuator) attached to its surface were performed to determine a multi vibration mode equivalent circuit representation of the piezoelectric patch harvester connected to the resistive load. For this purpose, firstly, the eigenvalue problem of the structure is solved in the range of frequency up to 250 Hz containing the first five lowest mode shapes, because these modes are used to design a vibration control system of this structure in Koszewnik (2018) and Koszewnik and Gosiewski (2016). This led to the division of modes into odd and even ones and indicating which group of the lowest modes is the best one from the energy harvesting point of view.

In the next step, a proper harvester location on the plate is determined based on the analysis of mechanical strain fields and values of forces generated by the piezo-actuator for chosen mode shapes. In this study, the plate and piezo-stripes are modelled as a plane element (PLANE42), while epoxy glue as a spring-damper element (COMBIN14). As a result, the obtained numerical model is divided into 435 elements, each of them 25 mm long and 12.5 mm wide. By following the modal analysis procedure, the first five eigenvectors corresponding to eigenvalues are determined. The obtained mode shapes with natural frequencies are shown in Fig. 2.
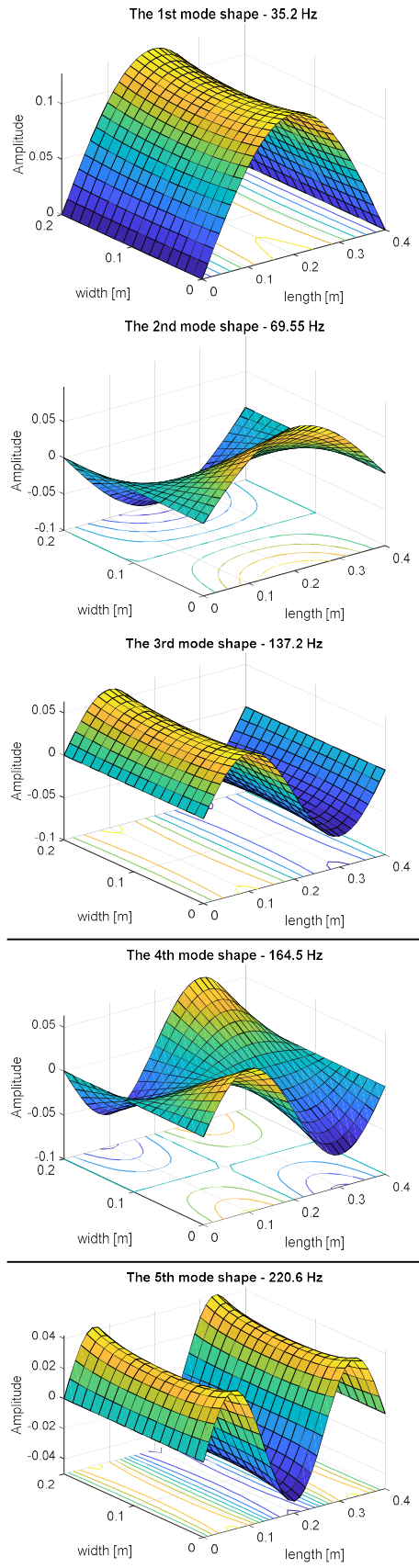
Fig. 2. The first five mode shapes of the transverse deformation for the SFSF plate in the frequency range 1–250 Hz (Koszewnik, 2018).

the overall surface with the maximum deflection placed at the half-length of this structure corresponding with the frequency of 35.2 Hz. In the case of two next modes, each of them has one node line in two perpendicular directions, respectively. The second mode (f2 = 69.5 Hz) has a node line longitudinally to Y axis at the centre of the plate, while the third mode (f3 = 137.2 Hz) at the centre of the X direction. Other modes (fourth and fifth) are totally different. The fourth mode has nodal lines located at the centre of the plate in both directions X and Y, respectively, while the fifth mode (f5 = 220.6 Hz) has also two nodal lines but they are located longitudinally to the Y axis.

Further analysis of modes' shapes in regard to the amount and direction of the nodes lines leads to assigning two kinds of modes, called 'odd modes' and 'even modes', respectively. As a result, the group of 'odd modes' is represented by only symmetrical modes located along the Y axis, while the 'even modes' – by modes symmetrically only along the X axis or screw-symmetrically versus X and Y axis.

The specified groups of mode shapes in the indicated frequency range 1–250 Hz allowed to determine a proper harvester location and orientation on the structure. For this purpose, the FE model was used again to calculate bending strain fields of the plate in two perpendicular directions X and Y, respectively.
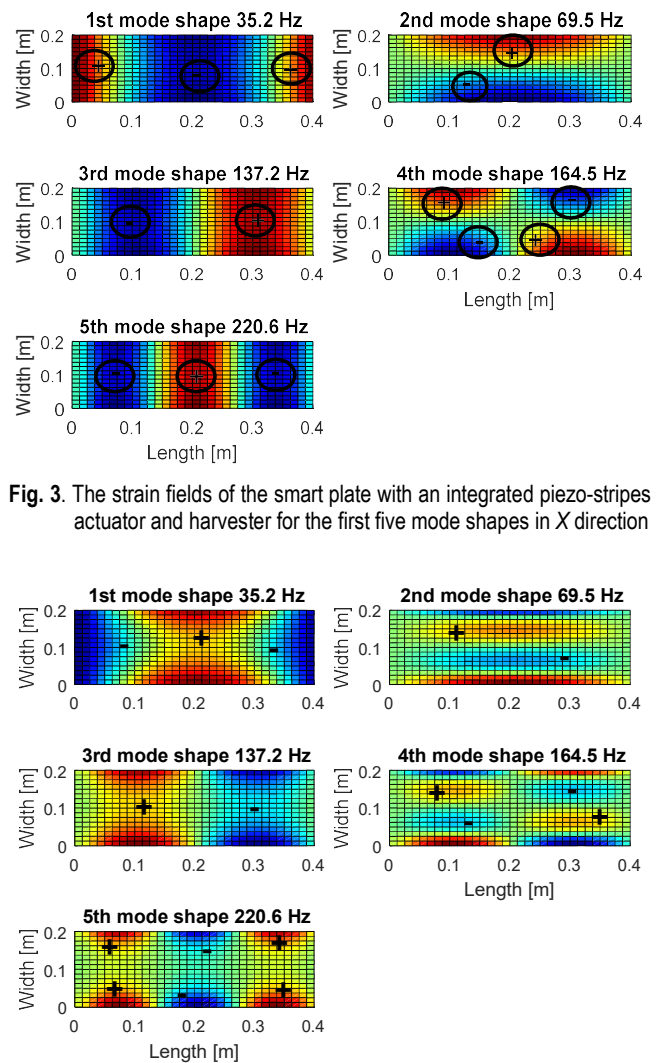

Fig. 3. The strain fields of the smart plate with an integrated piezo-stripes actuator and harvester for the first five mode shapes in *X* direction

Fig. 4. The strain fields of considered plate with an actuator and harvester for the first five mode shapes in *Y* direction

Fig. 2 shows the first five mode shapes of the transverse deformation of the smart plate with SFSF boundary conditions. As it can be seen in Fig. 2, the fundamental mode shape is in-phase on

The analysis of the obtained results shows that modal bending strain fields have strain nodal lines in both directions except for the fundamental mode of the plate first mode. From the energy harvesting point of view, it is a crucial problem because the output voltage is proportional to the strains. This implies that the output voltage generated by the harvester decreases dramatically when the piezoelectric stripe has a strain nodal line. Taking into account the electromechanical phenomena called voltage cancellation, it can be noticed that the longitudinal harvester orientations on the plate to the Y axis are less beneficial for the multi-vibration analysis. The harvester location in the proposed location (X = 0.10 m, Y = 0.05 m or X = 0.10 m, Y = 0.15 m) can be an exception, however, only for the second and the fourth modes. The strain fields in these areas are in-phase or out-of-phase. As a result, orienting the harvester only longitudinally to the X axis can be a better solution in this case. It is the consequence of the fact that this element can generate electrical outputs for almost all locations in the structure. Finally, the piezo harvester with a negligible effect on the strain distribution is placed at the left-lower quadrant of the plate in the distance of X = 20 mm from the simply-supported edge and Y = 50 mm from the free edge.

The indicated harvester locations and orientations on the host structure lead to calculating the modal value of the electromechanical coupling term Γ. For this purpose, based on Eq. (7), the modal value of this coefficient was calculated for each considered mode shapes. The obtained values of the electromechanical coupling term are collected and shown in Tab. 2.

Tab. 2. The value of modal elecromechanical coupling term determined for the five lowest natural frequencies

Mode shape	The electromechanical coupling term $\tilde{\Gamma}_i$
1st	-0.1231e-4
2nd	-0.0331e-4
3rd	-0.0593e-4
4th	-0.3096e-4
5th	-0.0604e-4

The modal force generated by the piezo-actuator is another parameter needed to calculate the DC voltage. For this purpose, the numerical model with a piezo-actuator located in the chosen places (see red rectangle in Fig. 5) on the plate are used again. In addition, the process of determining the piezo-actuator location is described in details in [22]. Each time it was assumed that the voltage applied to the piezo-actuators electrodes was 180 V, it allowed to generate a unit force in the indicated placement of the actuator and next, calculate the modal force fi(t) given by Eq. (8).

The analysis of the obtained results, presented in Fig. 5, show a significant increase of the modal forces values, especially for the odd modes. As a result, the process of determining a multi-mode representation of the Equivalent Circuit Model (ECM) is performed only for the first three odd mode shapes of the smart structure.

The obtained numerical results of the steady-state response of DC voltage are compared with a ECM model and shown in Fig. 9.
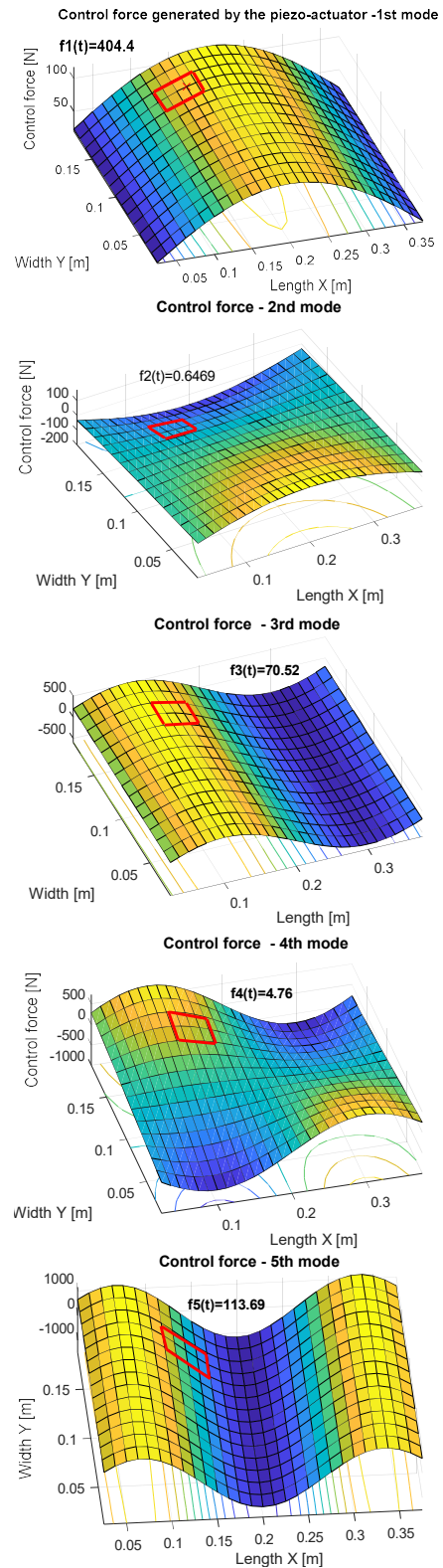

Fig. 5. The maximum amplitude of the modal force calculated for the piezo-actuator for the first five mode shapes

4. EQUIVALENT CIRCUIT MODELLING

The obtained distributed-parameters of the piezo-harvester integrated to the top surface of a 2D mechanical structure allowed to predict the power output with a good accuracy . It was achieved for the case when a linear component (e.g., resistor) is connected

to the system. Then, an equivalent circuit model (ECM) of the structure in the multi-mode is described by a finite number of lumped-parameters representing each vibration mode. In this case, the ECM model is composed of only three subsystems corresponding to the first odd mode shapes each of whom is described by the second order model. As a result, taking into account the electromechanical behaviour of the harvester, each vibration mode of the harvester is expressed by its capacitance (Cp), resistive load (R) and inductance (L), respectively. By applying Kirchhoff's Voltage Law to the multi-vibration mode circuit and by analogy with Eq. (6a), the parameters of the ECM model are identified and given by Eq. (10). Tab. 3 gives a summary of the analogy between the analytical distributed-parameter expression and the ECM, while Fig. 6 shows the comparison of both models, mechanical and ECM, in the frequency range of 1–250 Hz.

$$G_{ECM}(s) = \frac{s^3}{(s^2+4.42s+4.89e4)(s^2+9.24s+.55e5)(s^2+2.23s+.54e6)} \quad (10)$$

Tab. 3. Analogy between mechanical and electrical model of the piezo-stripe harvester

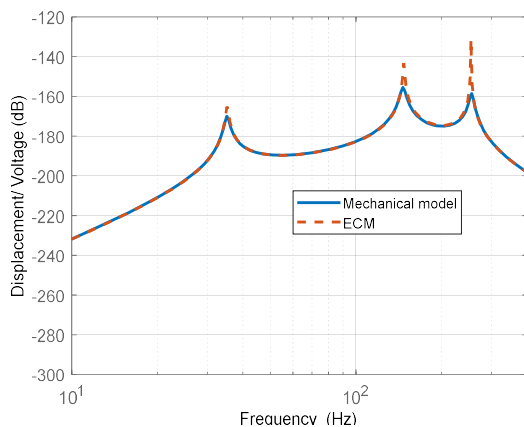| Parameters of mechanical model: $G_n(s)=\dfrac{W_n(s)}{F_n(s)}=\dfrac{k_n}{s^2+2\xi_n\omega_n s+\omega_n^2}$ where:	Parameters of ECM $G_{ECM,n}(s)=\dfrac{I_n(s)}{U_n(s)}=\dfrac{s}{Ls^2+R_n s+(1/C_n)}$ where:
Modal point force: $f_i(t)$	Modal voltage source: $V_i(t)$
1	Inductance: $L_i(t)$
$2\xi_{mi}\omega_{mi}$	Resistance: $R_i(t)$
$(1/\omega_{mi})^2$	Capacitance: $C_i(t)$
Γ_i	Transformer ratio: N_i
Modal time response: $\eta_{mi}(t)$	Electric charge: $Q_i(t)$
$\eta_{mi}(t)/dt$	Current $I_i(t)$

Fig. 6. The comparison of the amplitude plot of the mechanical model (experimental model) and the ECM model in the frequency domain containing three odd lowest frequencies' resonances

5. MODEL VALIDATION OF THE HARVESTER FOR THE STANDARD AC-DC PROBLEM

In this Section, an equivalent circuit model of an SFSF plate with perfectly bonded piezo-stripes QP20N and V21BL representing an actuator and a harvester is validated for the AC-DC stand-

ard problem from the electrical point of view (see Fig. 9b). In order to do this, the harvester on the lab stand, as it is shown in Fig. 7, is connected to a conditioning system EHE004 complex with a full-wave rectifier, a smoothing capacitor Cp = 100 μF and also the resistive load of R = 100 kΩ.
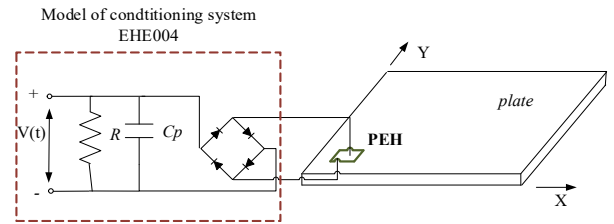

Fig. 7. The piezo-harvester V21BL connected to the EHE004 module

The experimental lab stand presented in Fig. 8a was also equipped with a bipolar voltage amplifier SVR-150bip/3 and a Digital Signal Analyzer (DSA). The amplifier is used to apply voltage (180 V) to the actuator, while the analyser – to measure and record the voltage output from the system.
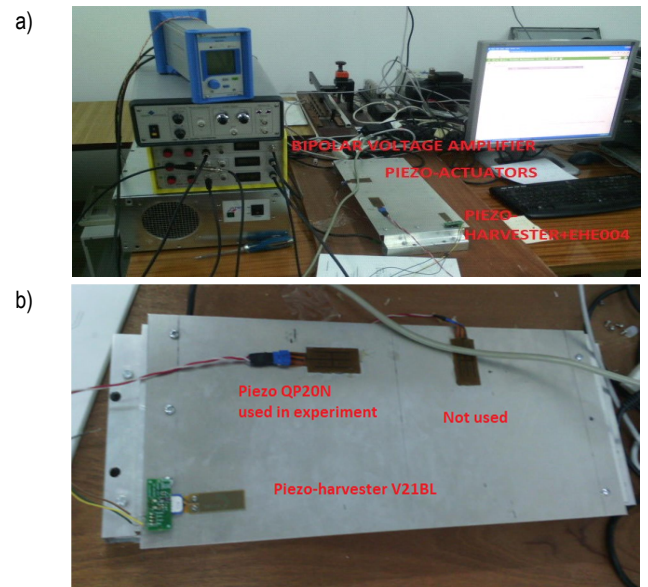

Fig. 8. a) The photo of the laboratory stand, b) the photo of a smart plate with piezo-elements (actuators QP10N and harvester V21BL) located on their top surface

The experimental set-up is carried out in a number of steps. In the first one, the structure is excited to vibration by using the piezo-actuator. For this purpose, a harmonic excitation signal in the form $u(t)$ = 2.5sin($2\pi f t$) is generated from DSA for a chosen natural frequency f_i of the structure (f_1 = 35.2 Hz, f_3 = 137.2 Hz, f_5 = 252.0 Hz), and next, it is applied to the actuator by the voltage amplifier. As a result, different values of the modal excitation force F_0 are obtained. From the measurement point of view, the vibration of the structure is measured by the harvester. The obtained AC voltage signals are rectified by the conditioning system EHE004 and then recorded by DSA. As a result, three steady state responses of DC voltages are obtained and shown in Fig. 9. In addition, the recorded signals are compared with the steady state response of DC voltages of ECM.

a)

b)

c)
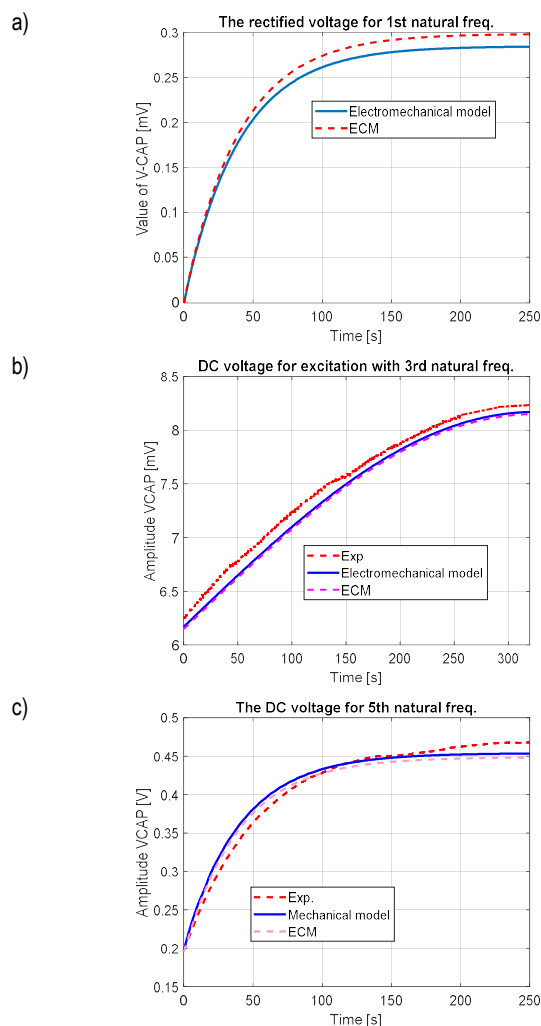
Fig. 9. Comparison of numerical (electromechanical model - blue line, Equivalent Circuit Model (ECM) - pink dash line) and experimental value (red dash line) of DC voltage obtained for the system excited to vibration with: a) 1st natural frequency, b) 3rd natural frequency, and c) 5th natural frequency

In the second step, the DC voltage is chosen as an indicator of the harvester effectiveness. Taking into account this indicator, it can be noticed that experimental results properly verified the numerical results. Especially, it is visible in Fig. 9b and Fig. 9c, where the values of voltage responses in the steady-state (8.5 mV for 3rd mode and 0.45 V for 5th mode) are close to the results obtained for ECM. In the case of the excitation system with the first natural frequency, the recorded voltage (less than 0.2 mV) was significantly lower than other result, and it was neglected. Further analysis of the obtained results showed that the filter capacitor Cp used in the system was not discharged enough. This leads to appearance of the offset value of DC voltages between tests. As a result, voltages for the electromechanical model and the equivalent circuit model were recalculated considering the ripple voltage and the capacitor discharge process. The corrected plots are shown in Fig. 9.

6. SUMMARY AND CONCLUSIONS

The thin SFSF plate with perfectly bonded piezo-patches is presented in the paper. Taking into account the chosen bounda-

ry conditions, the possibilities of the considered mechanical structure and the equivalent model to harvest energy are investigated. For this purpose, as the first step, the analysis of modes' shapes is carried out. The obtained results shown in Fig. 2 allowed to divide the considered modes into two groups according to the appearing node lines. In the next one, the bending strain fields of the smart plate in two perpendicular directions X and Y are considered. The numerical results shown in Fig. 3 and Fig. 4 indicated proper harvester locations and orientations on the structure for multi-vibration analysis. The calculated modal electromechanical coupling terms for the indicated harvester location allowed to assess the value of the steady state response of the DC voltage for an analytical model.

The obtained numerical results showed the effectiveness of the energy harvesting system only for the structure undergoing forced vibrations with only the first three odd natural frequencies. Taking into account this behaviour of the system, a multi-mode representation of the ECM model was determined only for the chosen vibration modes. By applying Kirchhoff's law and analogizing with Eq. (6a), parameters of the ECM model were determined.

Experimental tests carried out on the lab stand properly verified simulations results (see Fig. 9). The recorded steady state responses of DC voltage shows low effectiveness of the energy harvesting system beyond the case shown in Fig. 9c. This was caused by bigger dynamic strains' distributions appearing along the shorter edge of the plate. As a result, the generated voltage from the structure excited to vibration with the first or third natural frequency is not greater than 10 mV.

Summarizing, the performed investigations indicated that the harvester orientation on the 2D structure has its impact on the EH system properties. Further investigations of these systems connected with non-linear electrical components of the equivalent circuit model can lead to the increase of applying these systems in various types of civil infrastructure, especially in a range of structural health monitoring systems or powering other small devices with low power demand. Thus, taking the proposed approach into account, future research will be focused on an EH system located on the front wall of a dishwasher without a bitumen damper. As a result, this will lead to obtaining structural health monitoring systems of such mechanical structures.

REFERENCES

1. **Aboulfotoh N., Wallscheck J., Twiefel J., Bergman L.**, (2017), Toward understanding the self-adaptive dynamics of a harmonically forced beam with a sliding mass, *Archive of Applied Mechanics*, 87(4), 699–720.
2. **Ambrożkiewicz B., Litak G., Wolszczak P.**, (2020), Modelling of Electromagnetic Energy Harvester with Rotational Pendulum using Mechanical Vibrations to Scavenge Electrical Energy, *Applied Sciences*, 10(2), 671.
3. **Anton Novel SR.**, (2009), Piezoelectric Energy Harvesting Devices for Unmanned Aerial Vehicles, *Smart Material Structures*, 1–10.
4. **Anton SR.,** (2011), Multifunctional Piezoelectric Energy Harvesting Concepts, Doctoral Thesis, Virginia Polytechnic Institute and State University.
5. **Borowiec M.,** (2015), Energy harvesting of cantilever beam system with linear and nonlinear piezoelectric model, *The European Physical Journal – Special Topics*, 224, 2771–2786.
6. **Cahill P., Nuallian N., Jackson N., Mathewson A., Karoumi R., Pakrashi V.,** (2014), Energy Harvesting from Train-Induced Response in Bridges, *ASCE Journal of Bridge Engineering*, 04014034.

7. **Cahill P., Nuallian N., Jackson N., Mathewson A., Karoumi R., Pakrashi V.**, (2018), Vibration energy harvesting based monitoring of an operational bridge undergoing forced vibration and train passage, *Mechanical System and Signal Processing*, 106, 265–283

8. **Chiu Y., Tseng V.,** (2008), A capacitive vibration-to-electricity energy converter with integrated mechanical switches, *Journal of Micromechanics and Microengineering*, 18(10), 104004.

9. **Cook-Chennault K., Thambi N., Sastry S.,** (2007), Powering MEMS portable devices – a review of non-regenerative and regenerative power supply systems with special emphasis on piezoelectric energy harvesting systems, *Smart Material and Structures*, 16(3), 043001.

10. **De Marqui C.,** (2011), Modelling and analysis of piezoelectric energy harvesting from aeroelastic vibrations using the doublet-lattice method, *Trans. ASME Journal of Vibration Acoustic*, 133, 011003.

11. **Gosiewski Z.,** (2008), Analysis of Coupling Mechanism in lateral/torsional Rotor Vibrations, *Journal of Theoretical and Applied Mechanics*, 46(4), 829–844.

12. **Hanre RL.**, (2012), Concurrent attenuation of and energy harvesting from, surface vibrations: experimental verification, and model validation*, Smart Material Structures*, 21, 035016.

13. **Hanre RL.,** (2013), Development and testing of a dynamic absorber with corrugated piezoelectric spring for vibration control and energy harvesting applications, *Mechanical System and Signal Processing*, 36(2), 604–617.

14. **Hu Y. , Zhang Y.** (2011), Self-powered system with wireless data transmission, *Nano Letters*, 11(6), 2572–2577.

15. **Koszewnik A**. (2016), The optimal vibration Control of the Plate Structure by using piezo-actuators, Proceedings of the 17th IEEE International Carpathian Control Conference (ICCC), Tatrzanska Lomnica, Slovakia, 358–363

16. **Koszewnik A.** (2018), The Design of Vibration Control System for Aluminum Plate with Piezo-stripes based on residues analysis of model, *European Physical Journal Plus*, 133:405.

17. **Koszewnik A.** (2019), Analytical Modelling and Experimental Validation of an Energy Harvesting System for the Smart Plate with an Integrated Piezo-Harvester, *Sensors*, 19, 812.

18. **Koszewnik A., Gosiewski Z**. (2016) Quasi-optimal locations of piezo-elements on a rectangular plate, *European Physical Journal Plus*, 2016, 131:232.

19. **Koszewnik A., Wernio K.** (2016), Modelling and Testing of the piezoelectric beam as energy harvesting beam, *Acta Mechanica et Automatica*, 10(4), 291–295.

20. **Lee Ch., Lim Y.M., Yang B.** (2009), Theoretical comparison of the energy harvesting capability among various electrostatic mechanisms from structure aspect, *Sensor Actuator A*, 156(1), 208–216.

21. **Litak G., Borowiec M., Fischer M., Przystupa W**., (2009), Chaotic response of a quarter car model forced by a road profile with a stochastic component, *Chaos, Solutions and Fractals*, 9, 2448–2456.

22. **Naifar S., Bradai S., Viehweger C., Kanoun O**., (2015), Response analysis of a nonlinear magnetoelectric energy harvester under harmonic excitation, *The European Physical Journal – Special Topics*, 224, 2879–2908.

23. **Okosun F., Cahill P.,Hazra B., Pakrashi V**., (2019), Vibration-based leak detection and monitoring of water pipes using output–only Piezoelectric Sensors, *European Physical Journal – Special Topics*, 228, 1659–1675.

24. **Roundy W., Wright P., Rabaey J**., (2003), A study of low level vibrations as a power source for wireless sensor nodes*, Computer Communications*, 26, 1131–1144.

25. **Wang L., Yuan F.G.,** (2008), Vibration energy harvesting by magnetostrictive material, *Smart Materials and Structures*, 17, 045009.

A CIRCULAR INCLUSION AND TWO RADIAL COAXIAL CRACKS WITH CONTACTING FACES IN A PIECEWISE HOMOGENEOUS ISOTROPIC PLATE UNDER BENDING

Heorgij SULYM,* Viktor OPANASOVYCH,** Ivan ZVIZLO,** Roman SELIVERSTOV,*** Oksana BILASH****

*Faculty of Mechanical Engineering, Department of Mechanics and Applied Computer Science Application,
Bialystok University of Technology, ul. Wiejska 45 C, 15-351 Bialystok, Poland
**Faculty of Mechanics and Mathematics, Department of Mechanics,
Ivan Franko National University of L'viv, Universytetska St. 1, L'viv, 79000, Ukraine
***Faculty of Applied Mathematics and Informatics, Department of Programming,
Ivan Franko National University of L'viv, Universytetska St. 1, L'viv, 79000, Ukraine
****Faculty Training Specialists Battle (Operational) Software, Department of Engineering Mechanics,
Hetman Petro Sahaidachnyi National Army Academy, Heroes of Maidan Street, 32, L'viv, Ukraine

sulym@pb.edu.pl, viktor.opanasovych@lnu.edu.ua, zvizloivan@gmail.com, roman.seliverstov@lnu.edu.ua, oksana.opanasovych@gmail.com

received 5 December 2019, revised 19 March 2020, accepted 23 March 2020

Abstract: The bending problem of an infinite, piecewise homogeneous, isotropic plate with circular interfacial zone and two coaxial radial cracks is solved on the assumption of crack closure along a line on the plate surface. Using the theory of functions of a complex variable, complex potentials and a superposition of plane problem of the elasticity theory and plate bending problem, the solution is obtained in the form of a system of singular integral equations, which is numerically solved after reducing to a system of linear algebraic equations by the mechanical quadrature method. Numerical results are presented for the forces and moments intensity factors, contact forces between crack faces and critical load for various geometrical and mechanical task parameters.

Keywords: Bending, plate, interfacial zone, radial cracks, contact force, complex potentials, moment intensity factors, limit load

1. INTRODUCTION

Plate-shaped structural items are widely used in engineering. They may contain technological finite inclusions. There is also the possibility of cracking during operation. Cracks often greatly reduce plate's performance characteristics and may cause the structural item to destroy. In the presence of bending deformations, crack faces contact each other. It leads to significant redistribution of the stress-strain state near the crack tip (Shatsky, 1988; Kwon, 1989; Young and Sun, 1992; Dempsey et al., 1998; Opanasovych et al., 2012; Sulym et al., 2018) compared to neglecting the effect of crack closure.

Stress-strain state of biomaterial cracked plates and cracked plates with holes and inclusions under tension or/and bending is investigated by a variety of approaches and models (Wang and Nasebe, 2000; Hsieh and Hwu, 2002; Nielsen et al., 2012; Bäcker et al., 2015; Maksymovych and Illiushyn, 2017; Shao-Tzu and Li, 2017; Liu et al., 2018; Nguyen and Hwu, 2018; Sulym et al., 2018; Kuz' et al., 2019; Shiah et al., 2019 etc.).

Bending of a piecewise homogeneous, isotropic plate with a straight interfacial zone and a straight crack with contacting faces is investigated in Opanasovych and Slobodyan (2007).

The aim of this research is to investigate biaxial bending of a piecewise homogeneous isotropic plate with circular interfacial zone and two radial coaxial cracks on the assumption of crack closure along a line on one of the plate surfaces. Using methods of theory of functions of a complex variable together with complex potentials of classical plate bending theory and plane problem of elasticity theory, the solution of this problem is reduced to simultaneous singular integral equations, which are numerically solved. The forces and moments intensity factors, the contact forces between faces of cracks and the limiting plate load are analysed. Their graphical dependencies on various task parameters are plotted.

2. PROBLEM STATEMENT

Consider an infinite, piecewise homogeneous, isotropic plate with circular rigid inclusion and two coaxial radial cracks, whose faces are free from external loading. Let $2h$ is the plate thickness, R is the radius of the inclusion, and $2l_k$ is the length of the kth crack ($k = 1, 2$). The plate is under the action of uniformly distributed bending moments at infinity. Suppose the crack faces smoothly contact alone a line on the upper surface of the plate.

The origin of the chosen Cartesian coordinate system $Oxy\breve{z}$ is in the center of the circular rigid inclusion, the xy-plane coincides with the middle plane of the plate and the cracks are oriented along the x-axis. In the xy-plane, we introduce the polar coordinates (r, θ) with pole O and polar axis Ox. The x-coordinates of crack centres are $x_1 = R + d_1 > R + l_1$ and $x_2 = -R - d_2 < -R - l_2$, where d_k is a distance from the centre of the kth crack to the interfacial line. The x-coordinates of cracktips are a_i and $b_i (i = 1, 2)$. In the middle plane $S^+(S_1)$ and $S^-(S_2)$ refer to the

areas inside and outside the inclusion, respectively, L_1 denotes the union of straight line segments of two cracks, and L – the interfacial contour. M_x^∞ and M_y^∞ stand for distributed bending moments at infinity (Fig. 1).
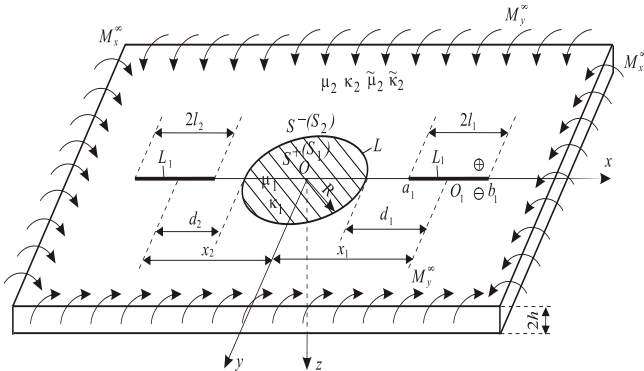

Fig. 1. Plate geometries and load scheme

Due to crack closure, the solution is a superposition of the solutions of two problems (Shatsky, 1988): the classical bending problem and the plane problem of elasticity theory under the following boundary conditions:

$$\sigma_{yy}^\pm = -\frac{N}{2h}, \sigma_{xy}^\pm = P_y^\pm = 0, M_y^\pm = M_y = hN, x \in L_1, \quad (1)$$

$$\partial_x[u_y] + h[\partial_{xy}^2 w_2] = 0, x \in L_1, \quad (2)$$

$$P_{r1} = P_{r2}, \ M_{r1} = M_{r2}, \ (r, \theta) \in L, \quad (3)$$

$$u_{r1} = u_{r2}, \ u_{\theta 1} = u_{\theta 2}, (r, \theta) \in L, \quad (4)$$

$$w_1 = w_2, \partial_r w_1 = \partial_r w_2, \ (r, \theta) \in L, \quad (5)$$

where: N – contact force between crack faces, σ_{xy} and σ_{yy} – stress tensor components, $u_{\theta j}$ and u_y – displacement vector components of plane problem (here and further $j = 1, 2$), w_j – deflection of the plate, M_{rj} and M_y – bending moments, P_y and P_{rj} – generalized Kirchhoff shear forces, $[f] = f^+ - f^-$ (superscripts '+' i '–' stand for limits of function f as a point of the middle plane approaches the cracks, $y \to \pm 0$), $\partial_a = \partial/\partial a$.

3. SOLUTION OF PLATE BENDING PROBLEM

We introduce complex potentials (Prusov, 1975) for areas S_j and set them as follows:

$$\Phi_{3j}(z) = \Phi_3^{(j)}(z) + \widetilde{\Phi}_1(z) + \widetilde{\Gamma},$$

$$\Psi_{3j}(z) = \Psi_3^{(j)}(z) + \widetilde{\Psi}_1(z) + \widetilde{\Gamma}',$$

where: $z = x + iy, i = \sqrt{-1}, \Phi_3^{(j)}(z)$ and $\Psi_{3j}(z)$ – holomorphic in S_j functions, $\widetilde{\Phi}_1(z)$ and $\widetilde{\Psi}_1(z)$ – vanished at infinity functions, which are holomorphic outside the cracks, $\widetilde{\Gamma} = -\frac{M_y^\infty + M_x^\infty}{4D_2(1+\nu_2)}, \widetilde{\Gamma}' = \frac{M_y^\infty - M_x^\infty}{2D_2(1-\nu_2)}, D_j = \frac{2Q_j}{3(1-\nu_j^2)}, \ Q_j = E_j h^3, \ E_j$ – elastic modulus, ν_j – Poisson's ratio.

Using the functions (Prusov, 1975) $\widetilde{\Omega}_1(z) = -\overline{\widetilde{\Phi}}_1(z) - z\overline{\widetilde{\Phi}}_1{}'(z) - \overline{\widetilde{\Psi}}_1(z)$ and $\Phi_3^{(j)}(z) = -\overline{\Phi}_3^{(j)}\left(\frac{R^2}{z}\right) +$

$\frac{R^2}{z}\overline{\Phi}_3^{(j)}{}'\left(\frac{R^2}{z}\right) + \frac{R^2}{z^2}\overline{\Psi}_3^{(j)}\left(\frac{R^2}{z}\right)$, in which $z \in S_{3-j}$, we can express the basic formulas of the classical plate bending theory in the form:

$$2\widetilde{\Gamma} - \frac{\bar{z}}{z}\widetilde{\Gamma}' + \Phi_3^{(j)}(z) - f_3^{(j)}(z) + \widetilde{\Phi}_1(z) + \tilde{f}_1(z) = \tilde{g}_j, \quad (6)$$

$$(\tilde{\kappa}_j - 1)\widetilde{\Gamma} + \frac{\bar{z}}{z}\widetilde{\Gamma}' + \tilde{\kappa}_j\Phi_3^{(j)}(z) + f_3^{(j)}(z) + \tilde{\kappa}_j\widetilde{\Phi}_1(z) - \tilde{f}_1(z) = \tilde{f}_j, \quad (7)$$

$$(\tilde{\kappa}_2 - 1)\widetilde{\Gamma} - \widetilde{\Gamma}' + \tilde{\kappa}_2\widetilde{\Phi}_1(z) + \tilde{f}_2(z) + \tilde{\kappa}_2\Phi_3^{(2)}(z) - g_3^{(2)}(z) = f_2, \quad (8)$$

$$2\widetilde{\Gamma} + \widetilde{\Gamma}' + \widetilde{\Phi}_1(z) - \tilde{f}_2(z) + \Phi_3^{(j)}(z) - g_3^{(2)}(z) = \partial_x g, \quad (9)$$

where:

$$\tilde{f}_1(z) = \left(1 + \frac{\bar{z}}{z}\right)\widetilde{\Phi}_1(z) + \frac{\bar{z}}{z}\tilde{f}_2(z),$$

$$\tilde{f}_2(z) = \widetilde{\Omega}_1(\bar{z}) - (z - \bar{z})\overline{\widetilde{\Phi}_1'(z)},$$

$$f_3^{(j)}(z) = \frac{R^2}{r^2}\Phi_3^{(j)}\left(\frac{R^2}{\bar{z}}\right) - \left(1 - \frac{R^2}{r^2}\right)\left\{\overline{\Phi_3^{(j)}(z)} - \bar{z}\overline{\Phi_3^{(j)}{}'(z)}\right\},$$

$$g_3^{(2)}(z) = \left(1 + \frac{R^2}{\bar{z}^2}\right)\overline{\Phi_3^{(2)}(z)} + z\overline{\Phi_3^{(2)}{}'(z)} - \frac{R^2}{\bar{z}^2}\left\{\Phi_3^{(2)}\left(\frac{R^2}{\bar{z}}\right) - \bar{z}\Phi_3^{(2)}{}'(z)\right\}, z = re^{i\theta}, \tilde{\kappa}_j = (3 + \nu_j)/(1 - \nu_j),$$

$$g = \partial_x w_2 + i\partial_y w_2,$$

$$\tilde{g}_j = -\frac{i}{z}\partial_\theta\left(\left(\partial_r w_j + \frac{i}{r}\partial_\theta w_j\right)e^{i\theta}\right),$$

$$\tilde{f}_j = 2\tilde{\mu}_j\left\{-M_r - ic_j' - iH_{r\theta} - i\int_0^s N_r(\tau)d\tau\right\},$$

$$f_2 = -2\tilde{\mu}_2\left\{M_y + i\tilde{c}' + iH_{xy} + i\int_{-l_j}^\tau N_y(\tau)d\tau\right\},$$

$$\tilde{\mu}_j = 1/\left(2D_j(1 - \nu_j)\right), c_j' \text{ and } \tilde{c}' - \text{ real constants.}$$

If the expansions of function $\Phi_3^{(1)}(z)$ and its analytic continuation in a series $\Phi_3^{(j)}(z) = \tilde{A}_0' + \tilde{A}_1'z + \dots (z \to 0)$ and $\Phi_3^{(1)}(z) = \tilde{B}_0' + \tilde{B}_1'z^{-1} + \dots (z \to \infty)$ are valid, the conditions (Prusov, 1975) $\tilde{B}_1' = 0$ and $\tilde{B}_0' = -\overline{\tilde{A}_0'}$ are fulfilled too.

On account of boundary value problem (1)–(2) and formula (8), we obtain a linear conjugation problem:

$$\left(\tilde{\kappa}_2\widetilde{\Phi}_1(t) - \widetilde{\Omega}_1(t)\right)^+ - \left(\tilde{\kappa}_2\widetilde{\Phi}_1(t) - \widetilde{\Omega}_1(t)\right)^- = 0, t \in L_1$$

whose solution is:

$$\widetilde{\Omega}_1(z) = \tilde{\kappa}_2\widetilde{\Phi}_1(z). \quad (10)$$

On the basis of (9), taking into account representation (10) and boundary conditions (1)–(2), we form the following linear conjugation problem:

$$\widetilde{\Phi}_1^+(t) - \widetilde{\Phi}_1^-(t) = Q_1(t), t \in L_1.$$

The solution of this problem is:

$$\widetilde{\Phi}_1(z) = \frac{1}{2\pi i}\int_{L_1}\frac{Q_1(t)}{t - z}dt,$$

where $Q_1(t) = \partial_x[\partial_x w_2 + i\partial_y w_2]/(1 + \tilde{\kappa}_2)$.

From the boundary conditions (5) and formula (6). we obtain one more linear conjugation problem:

Heorgij Sulym, Viktor Opanasovych, Ivan Zvizlo, Roman Seliverstov, Oksana Bilash
A Circular Inclusion and Two Radial Coaxial Cracks with Contacting Faces in a Piecewise Homogeneous Isotropic Plate under Bending

DOI 10.2478/ama-2020-0003

$$\left(\Phi_3^{(1)}(t) + \Phi_3^{(2)}(t)\right)^+ - \left(\Phi_3^{(1)}(t) + \Phi_3^{(2)}(t)\right)^- = 0, t \in L$$

with the solution:

$$\Phi_3^{(1)}(z) + \Phi_3^{(2)}(z) = -\overline{\tilde{A}_0'}. \tag{11}$$

Introducing a function:

$$\tilde{\Phi}(z) = \begin{cases} ic - (\underline{AA}_3 + \underline{AA}_4)\tilde{\Gamma} + \tilde{F}_1(z) + F_3^{(1)}(z), \\ \qquad\qquad z \in S^+, \\ -\underline{AA}_4 \frac{R^2}{z^2}\tilde{\Gamma}' + \tilde{F}_2(z) + F_3^{(2)}(z), z \in S^-, \end{cases} \tag{12}$$

where: $\tilde{F}_1(z) = -\underline{AA}_3\tilde{\Phi}_1(z)$, $F_3^{(j)}(z) = \tilde{\mu}_{3-j}\tilde{\kappa}_j\Phi_3^{(j)}(z) - \tilde{\mu}_j\Phi_3^{(3-j)}(z)$, $\tilde{F}_2(z) = \underline{AA}_4\Big\{\Big(1 + \frac{R^2}{z^2}\Big)\overline{\tilde{\Phi}}_1\Big(\frac{R^2}{z}\Big) + \frac{R^2}{z}\Big\{\tilde{\kappa}_2\tilde{\Phi}_1\Big(\frac{R^2}{z}\Big) - \Big(z - \frac{R^2}{z}\Big)\overline{\tilde{\Phi}}_1'\Big(\frac{R^2}{z}\Big)\Big\}\Big\}$, $c = 2\tilde{\mu}_1\tilde{\mu}_2(c_1' - c_2')$, $\tilde{g} = -\tilde{A}_1/\tilde{A}_2$, $\tilde{A}_j = \tilde{\mu}_j + \tilde{\mu}_{3-j}\tilde{\kappa}_j$, $\underline{AA}_3 = \tilde{\mu}_1\tilde{\kappa}_2 - \tilde{\mu}_2\tilde{\kappa}_1$, $\underline{AA}_4 = \tilde{\mu}_2 - \tilde{\mu}_1$, with respect to the boundary conditions (3) and formula (7), we make sure it is a solution of the linear conjugation problem $\tilde{\Phi}^+(t) - \tilde{\Phi}^-(t) = 0$ $(t \in L)$, which can be written as

$$\tilde{\Phi}(z) = \tilde{B} + \tilde{\mu}_2\overline{\tilde{A}_0'}, \tag{13}$$

where: $\tilde{B} = i\underline{AA}_4\overline{B_1}$, $B_1 = \frac{1}{2\pi}\int_{L_1} t^{-1}Q_1(t)dt$.

On the basis of (11) and (12) with respect to (13), we obtain:

$$\Phi_3^{(1)}(z) = -\Phi_3^{(2)}(z) - \overline{\tilde{A}_0'}, z \in S_j,$$

$$\Phi_3^{(2)}(z) = \begin{cases} \frac{1}{\tilde{A}_1}\{\tilde{F}_1(z) + ic - \tilde{B}\} - \Big(\frac{\tilde{A}_3}{\tilde{g}} + \tilde{A}_4\Big)\tilde{\Gamma} - \\ \qquad\qquad \tilde{A}_5\overline{\tilde{A}_0'}, \ z \in S^+, \\ \frac{1}{\tilde{A}_2}\{\tilde{B} - F_2(z)\} - \tilde{g}\tilde{A}_4\frac{R^2}{z^2}\tilde{\Gamma}', \ z \in S^-, \end{cases} \tag{14}$$

where: $\tilde{A}_4 = \underline{AA}_4/\tilde{A}_1$, $\tilde{A}_3 = \underline{AA}_3/\tilde{A}_2$, $\tilde{A}_5 = \tilde{\mu}_2(1 + \tilde{\kappa}_1)/\tilde{A}_1$.

Since $\Phi_3^{(1)}(0) = \tilde{A}_0'$, in view of (14), we can write:

$$\text{Re}\tilde{A}_0' = \frac{\tilde{A}_{12}}{1 - \tilde{A}_4}\big(\tilde{\Gamma} + \text{Im}\, B_1\big), \frac{c}{\tilde{A}_1} + \tilde{A}_5\text{Im}\,\tilde{A}_0' = \tilde{a}\text{Re}B_1,$$

where: $\widetilde{A}_{12} = \tilde{A}_4 - \tilde{A}_3/\tilde{g}$, $\tilde{a} = \tilde{A}_3/\tilde{g} + \tilde{A}_4$.

From the boundary conditions (1)–(2) and formula (8), we finally obtain the following integral equations:

$$\sum_{k=1}^2 \int_{-1}^1 \{Y_{k1}[K_{mk}(\eta,\xi) + L_{mk}(\eta,\xi)]\}d\eta = \tilde{c}_m', \tag{15}$$

$$\sum_{k=1}^2 \int_{-1}^1 \{Y_{k2}N_{mk}(\eta,\xi)\}d\eta = \tilde{m}hN_m(\xi)/M_y^\infty + P_m(\xi), \tag{16}$$

where:

$$Y_k(t) = Q_1Q_2(l_k t + x\_k)/M_y^\infty = Y_{k1}(t) + Y_{k2}(t),$$

$$\tilde{m} = -1/\big(\tilde{D}_2(1 - \nu_2)\big), \tilde{D}_2 = 2/\big(3\,(1 - \nu_2^2)\big),$$

$$P_m(\xi) = -\tilde{m} + \frac{\tilde{g}\tilde{A}_4 B}{X_m^2}\Big(\tilde{\kappa}_2 + 1 - \frac{3}{X_m^2}\Big) - \frac{2A\tilde{A}_{12}}{X_m^2(1 - \tilde{A}_4)},$$

$$A = -(\rho + 1)/\big(4\tilde{D}_2(1 + \nu_2)\big), B = -\tilde{m}(1 - \rho)/2,$$

$$K_{mk}(\eta,\xi) = -\frac{1}{\pi}\Big\{\tilde{\gamma}_2\tilde{\lambda}_k\widetilde{K}_{mk}(\eta,\xi) + \frac{\tilde{\lambda}_k}{2}\Big\{\frac{\tilde{g}\tilde{A}_4}{T_k}\Big(1 + \frac{1}{X_m^2}\Big) + \frac{1}{2X_m^2}\Big(\tilde{a} - \frac{\tilde{A}_5\tilde{A}_{12}}{\tilde{A}_4-1}\Big) + Q_{km}\Big[\tilde{g}\tilde{A}_4\Big(\frac{\tilde{\gamma}_2^2}{X_m} - X_m - \frac{3}{X_m^3}\Big) - \frac{\tilde{A}_3}{\tilde{g}X_m}\Big] + \tilde{g}\tilde{A}_4 Q_{km}^2\Big(X_m + \frac{4}{X_m} - \frac{5}{X_m^3}\Big) - \frac{2\tilde{g}\tilde{A}_4}{X_m}\Big(X_m - \frac{1}{X_m}\Big)^2 Q_{km}^3\Big\}\Big\},$$

$$\widetilde{K}_{mk}(\eta,\xi) = (T_k - X_m)^{-1}, \tilde{\gamma}_1 = 1 + \xi_1, \tilde{\gamma}_2 = -1 - \xi_2,$$

$$T_k = \tilde{X}_k + \tilde{\lambda}_k\eta, X_m = \tilde{X}_m + \tilde{\lambda}_m\xi, \tilde{\lambda}_k = l_k/R, \xi_k = d_k/R,$$

$$\rho = M_x^\infty/M_y^\infty, N_{mk}(\eta,\xi) = L_{mk}(\eta,\xi) - K_{mk}(\eta,\xi),$$

$$L_{mk}(\eta,\xi) = -\frac{\tilde{\lambda}_k}{2\pi}\Big\{\frac{1}{T_k}\Big(\tilde{\kappa}_2\tilde{g}\tilde{A}_4 - \frac{1}{X_m^2}\Big(\tilde{A}_4 - \frac{\tilde{a}}{2} - \frac{\tilde{A}_5\tilde{A}_{12}}{2(\tilde{A}_4-1)}\Big)\Big) + \tilde{\kappa}_2\tilde{g}\tilde{A}_4 Q_{km}\Big[\frac{3}{X_m^3} - X_m - \frac{2}{X_m} + Q_{km}\Big(X_m - \frac{2}{X_m} + \frac{1}{X_m^3}\Big)\Big]\Big\},$$

$Y_{k1}(t), Y_{k2}(t)$– real functions, $Q_{km} = 1/(T_kX_m - 1)$.

Equations (15) and (16) must be solved under the additional conditions:

$$\int_{-1}^1 Y_k(\eta)d\eta = \int_{-1}^1 \eta Y_{k1}(\eta)d\eta = 0 , k = 1, 2, \tag{17}$$

which assume that rotational displacements and deflection of the plate have to be single-valued when bypassing the contours of cracks.

Note that if the crack closure is neglected, the system of singular integral equations (15)–(17) takes $N_m(\xi) = 0$.

4. SOLUTION OF PLANE PROBLEM

We introduce Kolosov–Muskhelishvili complex potentials (Muskhelishvili, 1966) for areas S_j and represent them in the form:

$$\Phi_{Pj}(z) = \Phi_P^{(j)}(z) + \Phi_1(z), \Psi_{Pj}(z) = \Psi_P^{(j)}(z) + \Psi_1(z),$$

where: $\Phi_1(z), \Psi_1(z)$ – vanished at infinity functions, which are holomorphic outside the cracks; $\Phi_P^{(j)}(z), \Psi_P^{(j)}(z)$ – holomorphic functions in S_j. Moreover, at large $|z|\Phi_P^{(2)}(z) = O(1/z^2)$ and $\Psi_P^{(2)}(z) = O(1/z^2)$.

Similar as the previous chapter, we also introduce the following functions (Prusov, 1962):

$$\Phi_P^{(j)}(z) = -\overline{\Phi}_P^{(j)}\Big(\frac{R^2}{z}\Big) + \frac{R^2}{z}\overline{\Phi}_P^{(j)\prime}\Big(\frac{R^2}{z}\Big) + \frac{R^2}{z^2}\overline{\Psi}_P^{(j)}\Big(\frac{R^2}{z}\Big)$$

$$\tilde{\Omega}_1(z) = -\overline{\tilde{\Phi}}_1(z) - z\overline{\tilde{\Phi}}_1'(z) - \overline{\tilde{\Psi}}_1(z), z \in S_{3-j}.$$

Then a stress-strain state of the plate is given by the equations:

$$\sigma_{rr} + i\sigma_{r\theta} = \Phi_P^{(j)}(z) - f_P^{(j)}(z) + f_1(z), \tag{18}$$

$$2\mu_j\partial_\theta(u_x + iv_y) = iz\big[\kappa_j\Phi_{Pj}(z) + f_P^{(j)}(z) - f_1(z)\big], \tag{19}$$

$$\sigma_{yy} - i\sigma_{xy} = \Phi_{Pj}(z) + f_2(z) + g_P^{(2)}(z), \tag{20}$$

$$2\mu_2\partial_x(u_x + iv_y) = \kappa_2\Phi_{Pj}(z) - f_2(z) - g_P^{(2)}(z), \tag{21}$$

where: $\kappa_j = (3 - \nu_j)/(1 + \nu_j)$, $\mu_j = E_j/\big(2(1 + \nu_j)\big)$–

shear modulus, $f_1(z) = (1 + \bar{z}/z)\Phi_1(z) - \bar{z}/z\, f_2(z)$, $f_2(z) = \Omega_1(\bar{z}) + (z - \bar{z})\overline{\Phi_1'(z)}$, functions $f_P^{(j)}(z)$ and $g_P^{(2)}(z)$ can be obtained from expressions for $f_3^{(j)}(z)$ and $g_3^{(2)}(z)$ from (7), (9) by replacing index '3' by 'P'.

Formulas (6)–(9) in the bending problem and corresponding dependencies (18)–(21) in plane problem have the same structure. The boundary conditions (1)–(5) are also similar for both problems. Hence, by using the approach from the previous chapter, we find:

$$\Phi_1(z) = \Omega_1(z) = \frac{1}{2\pi i}\int_{L_1}\frac{g'(t)}{t - z}dt,$$

$$\Phi_P^{(1)}(z) = -\Phi_P^{(2)}(z) - \overline{A_0'}, z \in S_j,$$

$$\Phi_P^{(2)}(z) = \begin{cases} (F_1(z) - B)/A_1 - A_5\overline{A_0'}, z \in S^+, \\ (B - F_2(z))/A_2, z \in S^-, \end{cases}$$

where: $g'(x) = \frac{2\mu_2}{1 + \kappa_2}\partial_x[u_x + iu_y], A_5 = \frac{\mu_2}{A_1}(1 + \kappa_1)$,

$A_0' = \frac{B_5}{2\pi i}\int_{L_1}\frac{1}{t}\left[\left(A_4^2 - \frac{A_3}{g}\right)g'(t) + A_4\left(\frac{A_3}{g} - 1\right)\overline{g'(t)}\right]dt$,

$B_5 = (1 - A_4^2)^{-1}$, expressions for $B, F_1(z), F_2(z), \widetilde{AA}_3, \widetilde{AA}_4$, $g, A_n(n = 1, 4)$ are obtained from the corresponding expressions for $\tilde{B}, \tilde{F}_1(z), \tilde{F}_2(z), \underline{AA}_3, \underline{AA}_4, \tilde{g}, \tilde{A}_n(n = 1, 4)$ by the substitution $Q_1(t) \to g'(t), \tilde{\Phi}_1(z) \to \Phi_1(z), \tilde{\mu}_k \to \mu_k$, $\tilde{\kappa}_k \to \kappa_k, \tilde{A}_k \to A_k$ $(k = 1, 2)$.

In view of the boundary conditions (1)–(2), an unknown derivative of displacement jump across the crack faces $g'(x)$ is obtained by solving the integral equations:

$$\sum_{k=1}^2\int_{-1}^1 G_{k2}(\eta)[R_{mk}(\eta, \varepsilon) - S_{mk}(\eta, \varepsilon)]d\eta = 0, \tag{22}$$

$$\sum_{k=1}^2\int_{-1}^1 G_{k1}(\eta)M_{mk}(\eta, \varepsilon)d\eta = -\pi h N_m(\varepsilon)/(2M_y^\infty), \tag{23}$$

at $|\varepsilon| < 1, m = 1, 2$ and satisfying that displacements have to be single-valued when bypassing the contour of each crack:

$$\int_{-1}^1 G_k(\eta)d\eta = 0, k = 1, 2. \tag{24}$$

Formulas (20)–(22) have the following notations:

$R_{mk}(\eta, \varepsilon) = \lambda_k\left\{\tilde{R}_{mk}(\eta, \varepsilon) - \frac{A_4 g Q_{km}}{2\tilde{X}_m}\left\{\frac{1}{X_m} - \left(\frac{1}{X_m^2} + 1\right)\left[X_m + \frac{1}{X_m} - \tilde{X}_m Q_{km}\right] + 2\tilde{X}_m\left[\frac{2Q_{km}}{X_m^2} + \frac{1}{X_m^2} - \frac{\tilde{X}_m Q_{km}^2}{X_m}\right]\right\}\right\}$,

$M_{mk}(\eta, \varepsilon) = R_{mk}(\eta, \varepsilon) + S_{mk}(\eta, \varepsilon), \quad \tilde{X}_m = X_m - 1/X_m$,

$S_{mk}(\eta, \varepsilon) = -\frac{\tilde{\lambda}_k}{2}\left\{\frac{1}{T_k}\left(\frac{B_9}{X_m^2} + gA_4\right) - gA_4 Q_{km}\left[X_m - \frac{1}{X_m^3} - \tilde{X}_m Q_{km} + \frac{Q_{km}+2}{X_m^2}\right]\right\}, \quad G_k(\eta) = \frac{h^2}{M_y^\infty}g'(l\eta) = G_{k1}(\eta) + iG_{k2}(\eta), B_8 = A_5 B_5\left(\frac{A_3}{g} - 1\right), B_9 = A_4 + A_5 B_5\left(A_4^2 - \frac{A_3}{g}\right)$.

5. SUPERPOSITION OF SOLUTIONS

By substituting $N_{mk}(\varepsilon)$, which is obtained from (23) into (16), we get:

$$\sum_{k=1}^2\int_{-1}^1\{Y_{k2}N_{mk}(\eta, \varepsilon) + \beta_1 G_{k1}(\eta)M_{mk}(\eta, \varepsilon)\}d\eta = P_m(\varepsilon), |\varepsilon| < 1, m = 1, 2, \tag{25}$$

where $\beta_1 = 2\tilde{m}/\pi$.

Satisfying the boundary condition (2) leads to:

$$Y_{k2}(\eta) = \beta G_{k1}(\eta), \tag{26}$$

where: $\beta = -(1 + \kappa_2)(1 + \nu_2)/(1 + \tilde{\kappa}_2)$.

Based on the analysis of system of equations (15), (17), (22)–(24), (25) and (26) we conclude that $c_k' = 0$, $G_{k2}(\eta) = Y_{k1}(\eta) = 0$ $(k = 1, 2)$, that is, the solution of the problem is reduced to a system of singular integral equations, which consists of the following equation:

$$\sum_{k=1}^2\int_{-1}^1\{\beta N_{mk}(\eta, \varepsilon) + \beta_1 M_{mk}(\eta, \varepsilon)\}G_{k1}(\eta)d\eta = P_m(\varepsilon), |\varepsilon| < 1, m = 1, 2, \tag{27}$$

and equation (24).

Note that at $E_1 = 0$, this system turns into the system of integral equations from the research by Opanasovych and Slobodyan (2007).

6. NUMERICAL ANALYSIS

By using the mechanical quadrature method (Panasyuk et al., 1976), the system of singular integral equations (27), (24) is reduced to the following system of linear algebraic equations:

$$\frac{\pi}{M}\sum_{k=1}^2\sum_{m=1}^M Y_{km}[\beta N_{mk}(\eta_m, \varepsilon_r) + \beta_1 M_{mk}(\eta_m, \varepsilon_r)]d\eta = P_m(\varepsilon_r), m = 1, 2, r = \overline{1, M-1},$$

$$\sum_{m=1}^M Y_{km}(\eta) = 0, k = 1, 2,$$

where $Y_{km} = \sqrt{1 - \mu^2}G_{k1}(\eta_m), \quad \eta_m = \cos\frac{(2m-1)\pi}{2M}, \quad \varepsilon_r = \cos\frac{\pi r}{M}$.

The crack-tip stress distribution is given in research by Panasyuk et al. (1976). Formulas for the reduced moments intensity factors are:

$$K_M^{*\pm} = \frac{K_M^\pm}{M_y^\infty\sqrt{l}} = \mp\frac{2}{\beta_2(1 - \nu_2)M}\sum_{m=1}^M(-1)^{m+1+\frac{(M-1)}{2}(1\mp1)}Y_{km}\cot^{\mp1}\frac{(2m-1)\pi}{4M},$$

Where: $K_M^\pm$ are the bending moment intensity factors (twisting moment intensity factors are equal to 0); $\beta_2 = 3(1 + \nu_2)/(3 + \nu_2)$, '+' and '−' correspond to tips b_i and $a_i (i = 1, 2)$, respectively.

Note that reduced forces intensity factors $K_N^{*\pm} = \frac{hK_N^\pm}{M_y^\infty\sqrt{l}}$ are related to $K_M^{*\pm}$ as $K_N^{*\pm} = \beta_2 K_M^{*\pm}$, where $K_N^\pm$ are the forces intensity factors.

The critical value of the moment at which the plate collapses is calculated by the formula (Osadchuk, 1985):

$$\tilde{M}^\pm = \frac{M_y^\infty}{2h}\sqrt{\frac{\pi l}{2\gamma_* E_2}} = \left(K_M^{*\pm}\sqrt{\beta_2^2 + \beta_2}\right)^{-1},$$

where: γ_* is the density of an active surface energy of the plate material.

Numerical analysis is carried out at $\nu_1 = \nu_2 = 0.3$ and $l_1 = l_2 = l$. The values of $\tilde{n} = E_1/E_2$ are 0.1, 0.5, 1, 2, 10, 0.001, 1000 for lines labelled by 1, 2, 3, 4, 5, 6, and 7, respectively. In Figures 3 and 4, dashed lines correspond to the case when crack closure is neglected.

Fig. 2 illustrates the graphical dependence of the reduced contact force $N^* = hN/M_y^\infty$ between crack faces on the dimen-

Heorgij Sulym, Viktor Opanasovych, Ivan Zvizlo, Roman Seliverstov, Oksana Bilash
A Circular Inclusion and Two Radial Coaxial Cracks with Contacting Faces in a Piecewise Homogeneous Isotropic Plate under Bending

DOI 10.2478/ama-2020-0003

sionless coordinate $\xi = x_1/l$ at $d_1 = d_2 = d$, $\varepsilon = d/R = 1$, $\lambda = l/R = 0.8$ and $M_x^\infty/M_y^\infty = 1$.

Graphical dependencies of the reduced moment intensity factor K_M^* on $\varepsilon = d/R$ for tips a and b at $d_1 = d_2 = d$, $\lambda = l/R = 0.8$ and $M_x^\infty/M_y^\infty = 0.5$ are shown in Fig. 3.

Fig. 4 presents the graphical dependence of the reduced critical moment $\widetilde{M}$ on the relative distance from the second crack to the interface $\varepsilon_2 = d_2/R$ at $\lambda = l/R = 0.7$, $\varepsilon_1 = d_1/R = 1$ and $M_x^\infty/M_y^\infty = 1$.
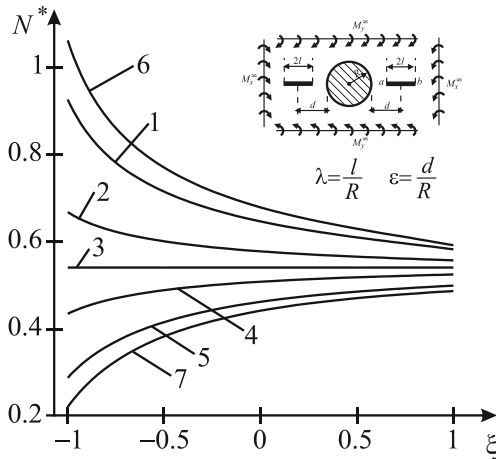
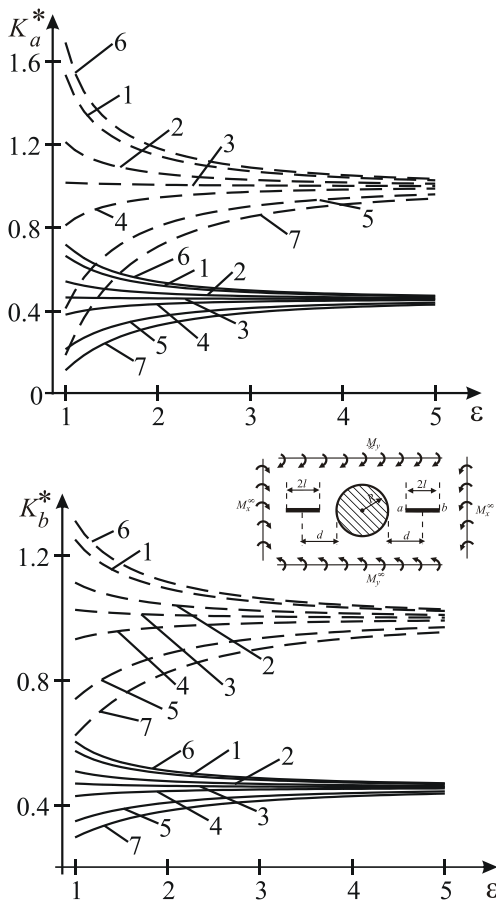**Fig. 2.** Dependence of the reduced contact force on the distance between interface and cracks

Fig. 3. Dependences of the reduced moment intensity factor on $\varepsilon = d/R$ in tip a (K_a^*) and b (K_b^*)
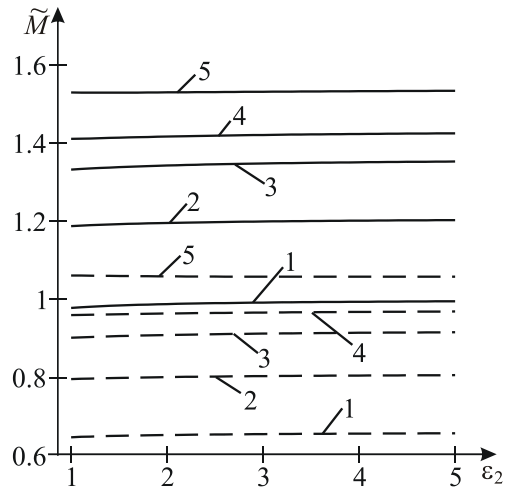

Fig. 4. Dependence of the reduced critical moment on the relative distance between second crack and interfacial line

7. CONCLUSIONS

The obtained dependencies show that if the inclusion is more rigid than the plate, the values of reduced contact force, intensity factors and critical moment are smaller than the corresponding values in case of a homogeneous plate. The situation is reversed for the pliable (in comparison with the plate) inclusion. The highest values are reached for the hole, the minimal ones – for the rigid plate.

Taking into account the contact of the crack faces leads to a decrease in the coefficients of the moment intensity and an increase in the ultimate load compared to the case when the contact of the crack faces is not taken into account. Crack closure consideration leads to decreasing of the moment intensity factors and to increasing of limit load.

REFERENCES

1. **Bäcker D., Kuna M., Häusler C.** (2015), Eigenfunctions of crack problems in the Mindlin plate theory, *ZAMM – Journal of Applied Mathematics and Mechanics*, 95(8), 763–777.
2. **Dempsey J. P., Shekhtman I. I., Slepyan L. I.** (1998), Closure of a through crack in a plate under bending, *International Journal of Solids and Structures*, Vol. 35, No. 31-32, 4077–4089.
3. **Hsieh M. C., Hwu C.** (2002), Anisotropic elastic plates with holes/cracks/inclusions subjected to out-of-plane bending moments, *International Journal of Solids and Structures*, 39 (19), 4905–4925
4. **Kuz' I. S., Moroz O. I., Kuz' O. N.** (2019), Strength of elastoplastic plates containing square holes (inclusions) and cuts (thin inclusions) under uniaxial tension, *Materials Science*, Vol. 54, No. 4, 603–609.
5. **Kwon Y. W.**(1989),Finite analysis of crack closure in plate bending. *Computers and Structures*, Vol. 32, No. 4, 1439–1445.
6. **Liu Z., Chen X., Yu D., Wang X.** (2018), Analysis of semi-elliptical surface cracks in the interface of bimaterial plates under tension and bending, *Theoretical and Applied Fracture Mechanics*, 93, 155–169.
7. **Maksymovych O., Illiushyn O.** (2017), Stress calculation and optimization in composite plates with holes based on the modifiedintegral equation method, *Engineering Analysis with BoundaryElements*, 83, 180–187.
8. **Muskhelishvili N. I.** (1966), Some basic problems of the mathematical theory of elasticity (in Russian), Nauka, Moscow.

9. **Nguyen, V. T., Hwu, C.** (2018), Multiple holes, cracks, and inclusions in anisotropic viscoelastic solids, *Mechanics of Time-Dependent Materials*, 22(2), 187–205.

10. **Nielsen C. V., Legarth B. N., Niordson C. F.** (2012), Extended FEM modeling of crack paths near inclusions, *International Journal for Numerical Methods in Engineering,* 89(6), 762–785.

11. **Opanasovych V. K., Slobodyan M. S.** (2007), Bending of a piecewise homogeneous plate with straightinterfacial crack with contactingfaces (in Ukrainian), *Mathematical Methods and Physicomechanical Fields*, 50(1), 168–177.

12. **Opanasovych V. K., Yatsyk I. M., Sulym H. T.** (2012), Bending of Reissner's plate containing a through-the-thickness crack by concentrat ed moments taking into account the width of a contact zone of its faces, *Journal of Mathematical Science*, 187(5), 620–634.

13. **Osadchuk V. A.** (1985), Stress-strain state and limit equilibrium of cracked shells (in Russian), Naukova dumka, Kyiv.

14. **Panasyuk V. V., Savruk M. P., Datsyshyn A. P.** (1976), Stress propagation near the cracks in plates and shells (in Russian), Naukova dumka, Kyiv.

15. **Prusov I. A.** (1962), Some problems of the thermoelasticity (in Russian), Belarus. Univ., Minsk.

16. **Prusov I. A.** (1975), The method of conjugation in the theory of plates (in Russian), Belarus. Univ., Minsk.

17. **Shao-Tzu C., Li H**. (2017), Boundary-based finite element method for two-dimensional anisotropic elastic solids with multiple holes and cracks, *Engineering Analysis with Boundary Elements*, 79, 13–22.

18. **Shatsky I. P.** (1988), Bending of a plate weakened by a crack with contacting faces (in Ukrainian), *Rep. of AS of USSR, Series Phys. Math. and Tech. Sci.*, 7, 49–51.

19. **Shiah, Y-C., Hwu, C., Yao, J. J.** (2019), Boundary element analysis of the stress intensity factors of plane interface cracks between dissimilarly adjoined anisotropic materials,*Engineering Analysis with Boundary Elements*, 106, 68–74.

20. **Sulym H., Opanasovych V., Slobodian M., Bilash O.** (2018), Combined Bending with Tension of Isotropic Plate with Crack Considering Crack Banks Contact and Plastic Zones at its Tops*, Acta Mechanica et Automatica*, Vol. 12, No. 2(44), 91–95.

21. **Sulym H., Opanasovych V., Slobodian M., Yarema Y.** (2018), Biaxial Loading of a Plate Containing a Hole and Two Co-Axial Through Cracks*, Acta Mechanica et Automatica*, Vol. 12, No. 3(45), 237–242.

22. **Wang X., Nasebe N.** (2000), Bending of a thin plate containing a rigid inclusion and a crack, *Engineering Analysis with Boundary Elements*, 24(2), 145–153.

23. **Young M. J., Sun C. T.**(1992),Influence of crack closure on the stress intensity factor in bending plates – A classical plate solution, *International Journal of Fracture*, 55, 81–93.

.

AUTOMOTIVE MR SHOCK ABSORBER BEHAVIOUR CONSIDERING TEMPERATURE CHANGES: EXPERIMENTAL TESTING AND ANALYSIS

Łukasz JASTRZĘBSKI*, Bogdan SAPIŃSKI*, Arkadiusz KOZIEŁ*

*Mechanical Engineering and Robotics, Department of Process Control,
AGH University of Science and Technology, Al. Adama Mickiewicza 30, 30-059 Kraków, Poland

lukasz.jastrzebski83@gmail.com, deep@agh.edu.pl, arkadiuszkoziel93@gmail.com

Abstract: This study investigates the automotive magnetorheological (MR) shock absorber behaviour in conditions of changing temperature. Its temperature-dependent behaviour was quantified between ambient and maximal operating temperatures of the device. Aspects addressed include the temperature dependence of the control coil resistance in the absorber, the influence of operating current level on control coil temperature and the temperature dependence of the absorber force response and energy dissipation in the system. The results of experiments enabled us to evaluate the mechanical performance of the absorber at varied temperatures.

Key words: MR Shock Absorber, Temperature, Current, Coil Resistance, Force, Energy

1. INTRODUCTION

Magnetorheological (MR) shock absorbers are used in suspensions of passenger cars and sports vehicles to improve the ride comfort by controlling undesired vibrations. Studies of MR shock absorber behaviour have identified several major determinants of the output force (response), such as mechanical and magnetic hysteresis, control circuit dynamics, driver dynamics, temperature, flow losses, friction and nonlinear relationship between the material's yield stress and the induced flux (Bajkowski and Skalski, 2012; Strecker et al., 2015; Gołdasz et al., 2018; Gołdasz and Sapiński, 2019; Kubik and Gołdasz, 2019). These factors need to be taken into account when designing control systems for the device (Choi et al., 2005; Sims, 2006; McKee et al., 2018). Specifically, there are three key effects of rising temperature on the MR shock absorber force output (Batterbee and Sims, 2009). The first effect involves the reduction of the yield force corresponding to a reduction in the MR fluid's yield stress. The second one is decrease in the slope of the post-yield force–velocity response associated with reduction in the MR fluid's viscosity. The third effect involves the reduction of the force–velocity hysteresis loop size, associated with a change in the absorber's stiffness caused by the ring accumulator pressure.

The present study aims to investigate the temperature factor in the Magnetic Ride absorber in cars of series Audi TT Quatro. This factor is of great importance when the MR device experiences large temperature variations (Gordaninejad and Breese, 1999). The objective of this work is to evaluate the absorber's behaviour under the condition of varied temperature through experiments. The resulting behaviour of the Magnetic Ride absorber will be taken into account by the authors when designing temperature-sensitive controller.

This study is organised as follows. In Section 2, we provide the characteristics of the Magnetic Ride absorber and test facili-

ties. In Section 3, the experimental procedure is summarised for the experiments conducted in the constant climate cabinet with no piston displacement, and then when the absorber is subjected to a particular excitation via piston displacements and constant current inputs. Section 4 covers the experimental results and discussion of the temperature effects on the absorber behaviour. Conclusions are given in the Section 5.

2. STRUCTURE AND FORCE RESPONSES OF THE ABSORBER

The structural design of the absorber is shown in Fig. 1, which reveals a typical mono-tube flow-mode damper configuration with an annular gap. Geometrical parameters of the device are: piston stroke 178 mm, outer diameter of the cylinder 50 mm, the length with the piston in compression position 381 mm and the length with the piston in rebound position 559 mm. The cylinder is filled with 277 cm^3 of MR fluid. The absorber comprises an accumulator 65 cm^3 in volume, filled with nitrogen. The maximal current in the control coil should not exceed 5 A. The device ought to be operated in the temperatures ranging from −30 °C to 100 °C.
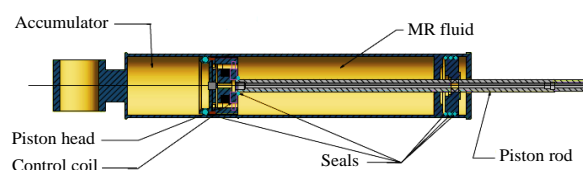
Fig. 1. Schematic diagram

Fig. 2 shows typical plots of force response F vs piston position x (Jastrzębski and Sapiński, 2017). These plots were obtained under

the applied input in the form of triangular piston displacement of amplitude 75 mm and frequency 0.5 Hz, corresponding to the constant velocity of the piston 150 mm/s, both in the rebound phase and in the compression phase. The absorber's force output in the stroke centre position is found to be 335 N at current I = 0 A, whilst under the maximal current I = 5 A in the control coil, the force response is increased 14-fold in relation to that registered under the conditions of no power supply.
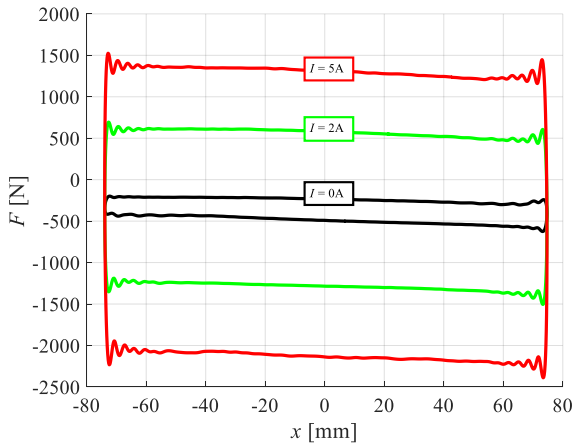

Fig. 2. Force vs piston position

3. TEST FACILITIES AND EXPERIMENTS

In the first stage, the experiments were performed to explore temperature dependence of the control coil resistance in the shock absorber. The experimental setup shown in Fig. 3 comprises an SB11/160/80 constant climate chamber manufactured by Weiss Technik (WEISS TECHNIK, 2019) and a Fluke8846A precision resistance multimeter (FLUKE, 2019). The constant climate chamber allows the temperature to be controlled and maintained at a constant level in the range 20 ºC–100 ºC.
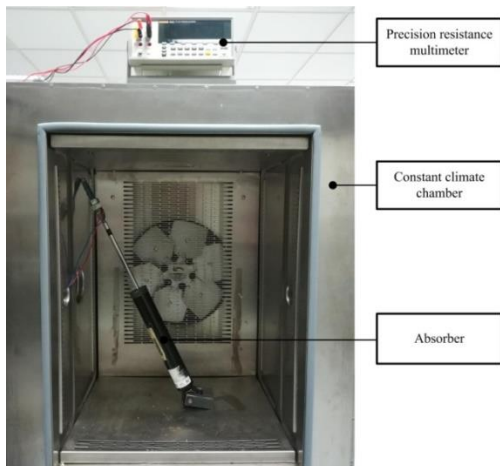

Fig. 3. Test facility with the constant climate chamber

The second cycle of experiments were conducted to determine the relationship between the cylinder temperature in the shock absorber and the temperature of the control coil under the current inputs 1, 2, 3, 4 and 5 A. The case was analysed in which the piston remained immobile at its maximal position in the rebound phase and when it moved at the fixed rate 150 m/s in the

compression phase and the rebound phase. The applied triangular input inducing the piston motion around its mid-position had an amplitude A = 75 mm and frequency f = 0.5 Hz. When the applied current levels were 1, 2, 3 and 4 A, the experiment lasted 180 s; with the applied current level at 5 A, the experiment took 480 s (the time required by the cylinder in the shock absorber to reach the temperature of 100 ºC). The cylinder temperature was determined with the use of a thermovision camera, whilst the temperature of the control coil was calculated based on changes in the coil winding's resistance. All experiments were conducted in the test facility shown schematically in Fig. 4 and incorporating an MTS 810 testing system (MTS, 2019) and a current controller (Sapiński et al., 2012), complete with the power supply and the measurement data acquisition system. The current controller is fitted with integrated circuits used for voltage and current measurement in the control coil of the shock absorber and an in-built PID controller. The controller enables the coil to be supplied with currents up to 7 A. Piston displacements and the damping force delivered by the shock absorber were measured with the sensors in the MTS 810 tester machine. The data acquisition system comprises an RT-DAC PCI card (INTECO, 2019) and a PC operated under Windows 7 in the MATLAB/Simulink environment. The temperature of the cylinder in the shock absorber was measured using the Flir E40 thermovision camera (FLIR, 2019).
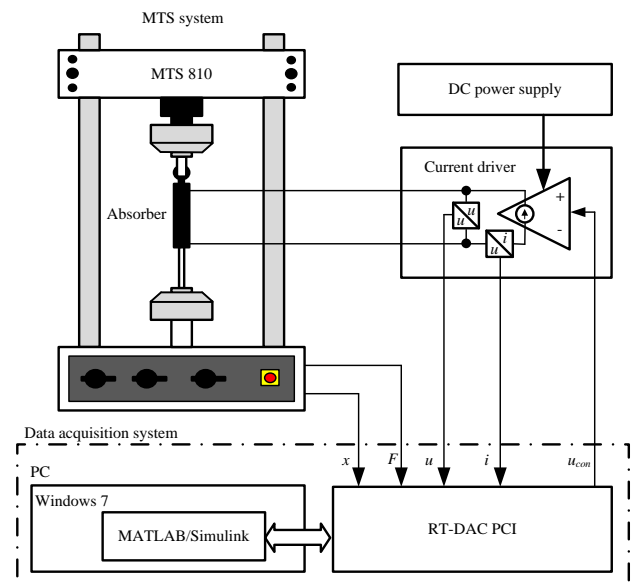

Fig. 4. Test facility with MTS testing system

4. RESULTS AND DISCUSSION

Experimental results summarised in three sub-sections clearly demonstrate how temperature influences the resistance of control coils and how the current level in the coil impacts on the changes in the coil and cylinder temperatures under the condition when the piston should remain immobile, thus revealing the temperature dependence of the mechanical performance of the device.

4.1. Influence of temperature on control coil resistance

The constant climate chamber in which the temperature was maintained constant throughout the experimental procedure is

shown in Fig. 3. Temperature could be varied in the range from 20 ºC to 100 ºC, at 5 ºC intervals. In order to uniformly heat the entire volume of the shock absorber to reach the preset temperature, the absorber was maintained inside the chamber for 1 hour. Afterwards, measurements were taken of the control coil resistance and the temperature inside the chamber was raised at the predetermined rate. The resistance of the cable connecting the absorber with the power drive was duly accounted for in the measurement procedure.
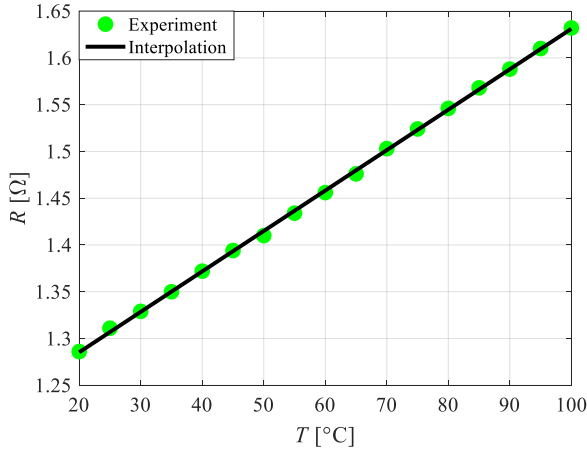

Fig. 5. Coil resistance vs temperature

Experimental data are plotted in Fig. 5. It appears that control coil resistance R is linearly related to the absorber's temperature T. At 20 ºC, the coil resistance becomes 1.276 Ω, and at 100 ºC, it is found to be 1.643 Ω. Based on the data obtained (indicated in green markers in Fig. 5) and recalling the least square method, the following coefficients were derived accordingly: a = 0.00459 Ω/°C and b = 1.184 Ω of the linear function (see black continuous line), as shown in Equation (1).

$$R = a \cdot T + b \tag{1}$$

For electric conductors, resistance can be expressed as:

$$R = R_0 (1 + \alpha \cdot \Delta T) \tag{2}$$

where R_0 is the conductor resistance at the reference temperature T_0, α is the temperature coefficient of resistance and ΔT is the temperature change from T_0 to T.

Recalling Equations (1) and (2), the temperature coefficient of resistance was derived accordingly: α = a/b = 3.88 × 10⁻³ 1/ºC. Its value is nearing that listed in physical tables for copper wire from which the control coil is made: α_{CU} = 3.9· × 10⁻³ 1/ºC. At T_0 = 0 ºC, the calculated coil resistance is: R_0 = b = 1.184 Ω. Temperature T of the coil can be derived recalling Equation (3) and resistance readouts R.

$$T = \frac{1}{\alpha} \left(\frac{R}{R_0} - 1 \right) \tag{3}$$

Temperature of the control coil derived from Equation (3) is closer to that of the MR fluid in the gap in the shock absorber than to the temperature on the cylinder surface. An increase in the temperature of MR fluid can be attributed to thermal energy arising due to friction during the fluid flow in the gap and to thermal energy associated with current flow in the control coil.

4.2. Influence of current level on the control coil temperature

Experiments were conducted using the test facility shown in Fig. 4. Throughout the experimental procedure, the piston rod in the shock absorber stayed in the rebound position and remained immobile. Resistance of the control coil R was derived based on the voltage u and current i readouts.

The obtained results are plotted in Figs 6–10. Fig. 6 shows the time histories of the control coil resistance R during heating associated with DC current I. Fig. 7 plots the time history of control coil temperature T, derived from Equation (3).
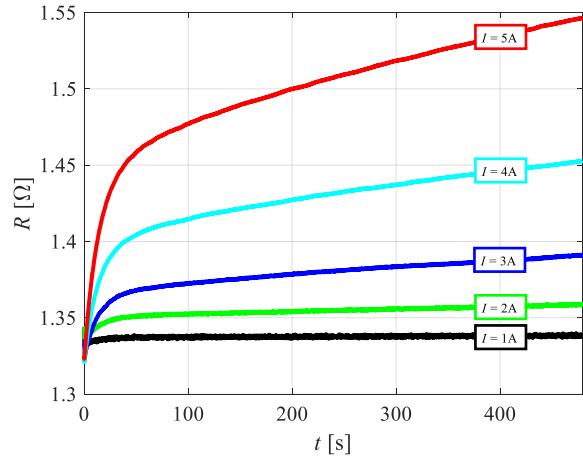

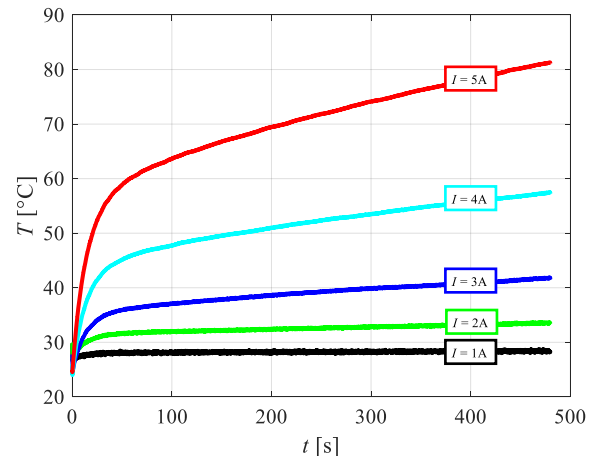**Fig. 6.** Time patterns of coil resistance at various current levels

Fig. 7. Time patterns of coil temperature at various current levels

Apparently, after time t = 480 s (current level 1 A), resistance and temperature of the control coil increase by about 1%, whilst at 2 A, there is a 3% increase. It is reasonable to suppose, therefore, that at current levels I ≤ 2A, the released thermal energy will not cause any temperature change of the coil (MR fluid). At current levels 3, 4 and 5 A, resistance and temperature of the control coil increase by 5%, 12% and 20%, respectively. Plots in Figs 6 and 7 clearly indicate that the process of coil heating involves two distinct stages. In the first stage, when t ≤ 50 s, the temperature goes up rapidly; in the second phase, when t > 50 s, the temperature increase is found to be less significant.

To better highlight this effect, plots of coil temperature and

temperature on the cylinder surface vs time are compared for the current level I = 5 A (Fig. 8a). Time histories of the cylinder temperature were derived from the distribution of temperature readouts from the thermovision camera registered in 5-s time intervals. Figs 9 and 10 plot selected temperature distribution patterns registered at the time instants: 0, 50, 240, 480, 540, 600, 720 and 960 s.

Obviously, within the time t ≤ 50 s, the difference between the temperature of the control coil and that of the cylinder tends to grow rapidly. After that time, the temperature difference becomes 35 ºC and remains at that level until the end of the heating phase (t = 480 s). Fig. 8b shows the change in the coil and cylinder temperature from the moment heating of the shock absorber should cease (i.e. from the time instant t = 480 s until t = 960 s). In order that the resistance of the control coil can be derived so as to determine its temperature through voltage u and current i measurements (Fig. 4), the current driver value must be I = 0.5 A. Such current levels should not cause any increase in the control coil temperature (Fig. 7). Apparently (see Fig. 8b), the difference between the temperature of the control coil and that of the cylinder tends to decrease from t = 480 s to t = 530 s. In the subsequent time instants, the temperatures of the control coil and of the cylinders are nearly identical.

a) Heating

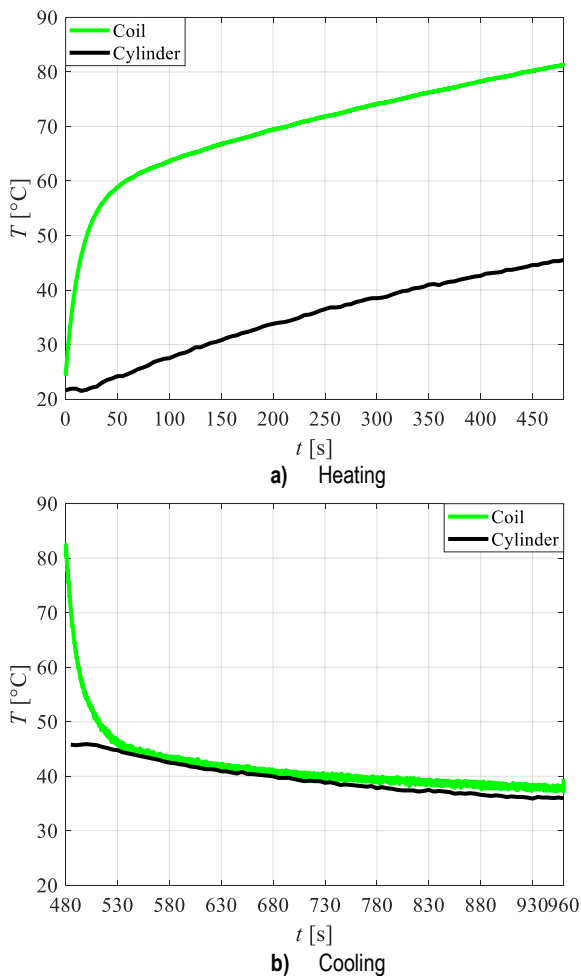
b) Cooling

Fig. 8. Time pattern of the coil and cylinder temperature

a) *t* = 0 s

b) *t* = 50 s

c) *t* = 240 s

d) *t* = 480 s
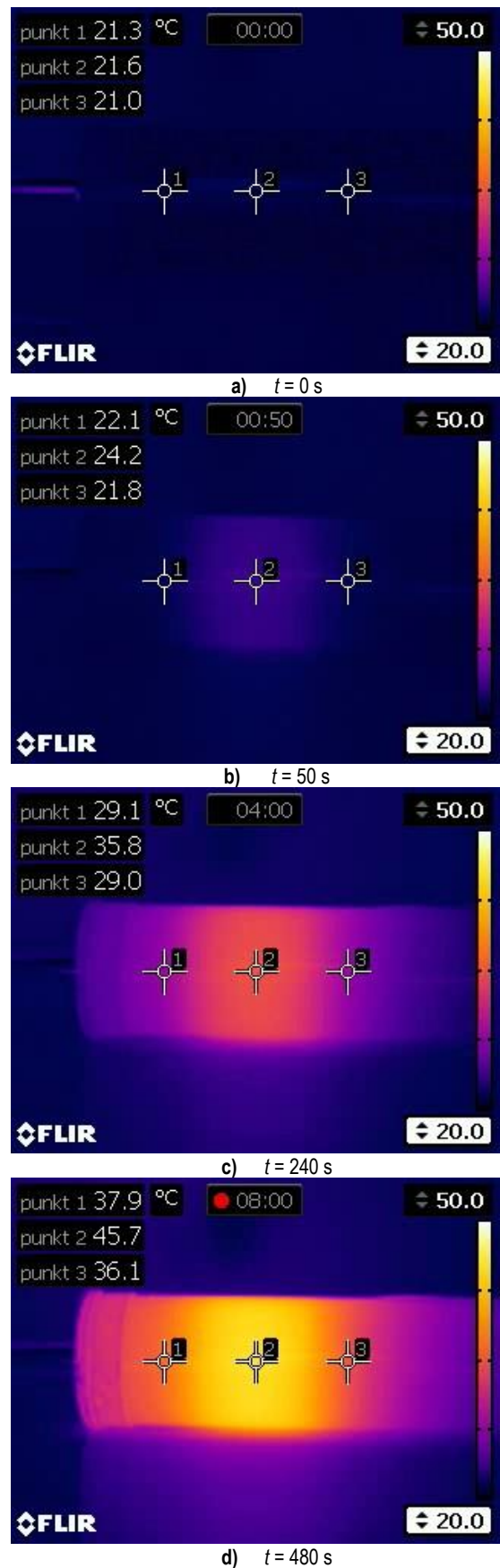
Fig. 9. Temperature distribution on the cylinder surface when heating

Łukasz Jastrzębski, Bogdan Sapiński, Arkadiusz Kozieł
Automotive MR Shock Absorber Behavior Considering Temperature Changes: Experimental Testing and Analysis

DOI 10.2478/ama-2020-0004

a)   *t* = 540 s

b)   *t* = 600 s

c)   *t* = 720 s

d)   *t* = 960 s

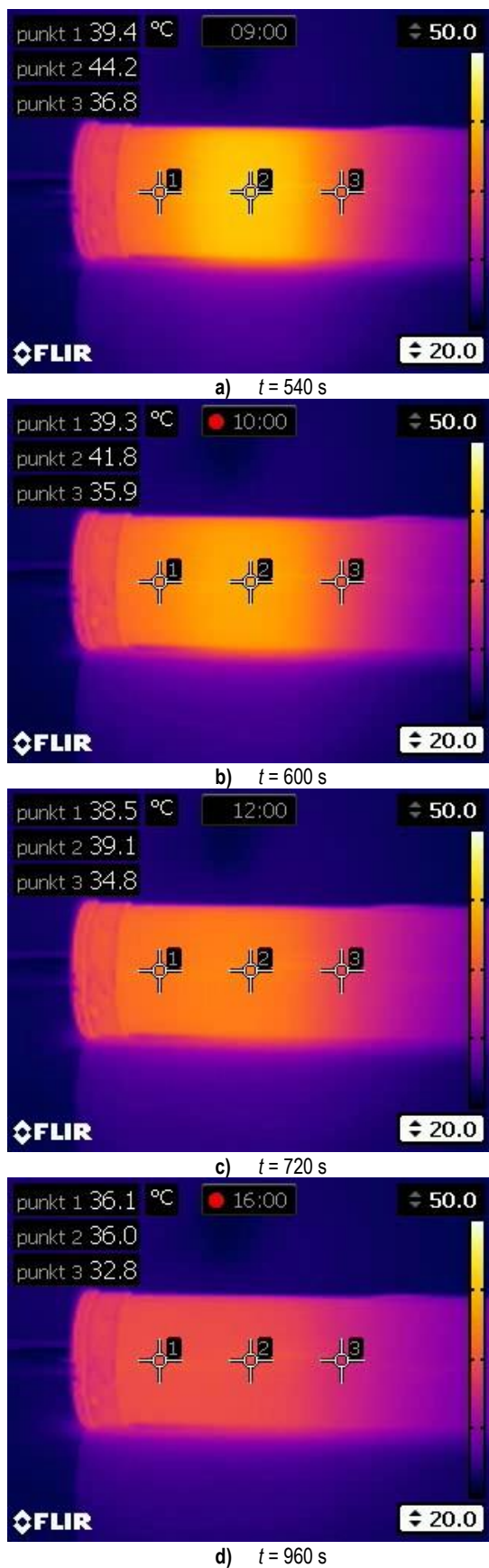**Fig. 10.** Temperature distribution on the cylinder surface when cooling

Fig. 9 shows the temperature distribution on the cylinder surface whilst the control coil is heated by the flowing current I = 5 A. The range of camera-registered temperature was set to fall in the

interval from 20 ºC to 50 ºC, which affords us the means to highlight the temperature readouts collected at points 1, 2 and 3 A on the surface of the cylinder. Point 2 is located in the middle section of the cylinder surface, which coincides with the mid-point of the piston. Points 1 and 3 lie along the line coinciding with the shock absorber axis, beyond the area in which the piston is located. The temperature of the shock absorber when the piston begins to be heated is 21.6 ºC (Fig. 9a, point 2). Temperature distribution on the surface of the cylinder is uniform, and the temperature difference between points 2 and 3 should not exceed 0.6 ºC. After time t = 50 s, a high-temperature region is revealed on the cylinder surface, its temperature approaching 24.2 ºC (Fig. 9b, point 2). The difference in temperature between points 2 and 3 goes up to 2.4 ºC. After the elapse of 240 s, the temperature at point 2 reaches the level 35.8 ºC (Fig. 9c), and after 480 s, it becomes 45.7 ºC (Fig. 9d). After these time instants, the respective temperature difference between points 2 and 3 would be 6.8 ºC and 9.6 ºC.

Cooling of the control coil is illustrated in Fig. 10. Actually, the temperature at point 2 is 44.2 °C after time t = 540 s, 41.8 °C after t = 600 s, 39.1 °C after t = 720 s and 36 °C after t = 960 s.

4.3. Influence of temperature on the absorber performance

Like the previous case, the experiments were conducted in the setup shown in Fig. 4. Throughout the experimental procedure, the rate of piston motion in the shock absorber was 150 mm/s, both during the compression and the rebound phases. The main purpose of the experiments was to find out how the temperature of the control coil impacts on the shock absorber efficiency and performance in terms of the output force range, response force of the accumulator, dissipated power and energy. Another issue addressed was the temperature dependence of electric power required to supply the control coil with preset DC current. Shock absorber efficiency is derived based on the coil temperature because its value is closer to the temperature of MR fluid than to that of the cylinder surface.

Fig. 11 plots the time histories of the control coil temperature in the course of its heating due to the current flow and friction associated with MR current flow in the gap. After the time instant t = 180 s, temperature of the control coil for the current levels 1, 2, 3, 4, 5 A went up by 27%, 66%, 108%, 153% and 200%, respectively. Time histories of the control temperatures registered for the current level 5 A are compared in Fig. 12, having relevance to the case when the piston was in motion (black line) and remained immobile (red line). Apparently, after the elapse of t = 480s, the control coil temperature became higher by nearly 60 °C whilst the piston was in motion than when it remained immobile. In both cases, the rate of temperature change was enhanced when t ≤ 50 s.

The temperature dependence of the force output of the shock absorber was investigated by varying the control temperature from 30 ºC do 143 ºC (this temperature corresponds to the maximal temperature of the cylinder given in the manufacturer's specification as 100 °C). In order to ensure such range of temperature control, the experiments were conducted with the maximal velocity of the piston motion achievable in the MTS testing system and for the maximal rod displacements both in the compression and the rebound phases (150 mm), under the maximal current level in the control coil 5 A. In those conditions, the cylinder reached a temperature of 100 °C after time t = 480 s.
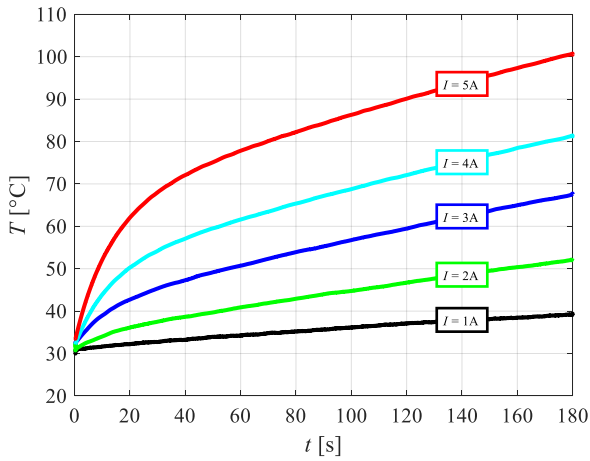
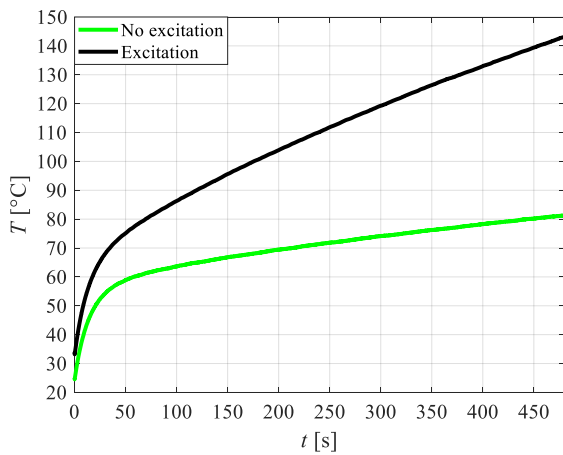**Fig. 11.** Time pattern of coil temperature at various current levels; piston excitation A = 75 mm, f = 0.5 Hz

Fig. 12. Time pattern of coil temperature at current I = 5 A with excitation and with no excitation

Fig. 13 shows the force–position loops of the absorber for the respective coil temperatures: 30 °C, 110 °C, 140 °C. An increase in temperature causes reduction of the range of output force, expressing the difference between the force responses when the piston is in the position x = 0 mm in the compression and rebound cycle. At temperatures 30 °C, 110 °C and 140 °C, the respective output force ranges become 3720, 3195 and 2985 N. Temperature dependence of the averaged absorber force response Fm is shown in Fig. 14. Apparently, the magnitude of force response Fm changes by 50% when the control coil temperature goes up from 30 °C to 140 °C, which is attributable to the increase of gas temperature in the accumulator.

Fig. 15 plots the time history of dissipated energy E within a full cycle of the piston motion (the piston returning to its initial position), derived from Equation (4).

$$E(t) = \oint F(x)dx = \int_{t}^{t+\tau} F(t)\frac{dx}{dt}\,dt \qquad (4)$$

where т = 1/f.

Apparently, the amount of energy dissipated varies in time, which is associated with temperature increase in the system. The dissipated energy tends to decrease at a faster rate within time t ≤ 50 s than at the remaining time of the experiment. The coil temperature dependence of dissipated energy is plotted in Fig. 16. This relationship can be well approximated by a linear function. In this case, the coefficient of determination r^2 is equal to 0.985.

When the temperature of the control coil increases by 110 °C, the amount of dissipated energy will decrease by about 20%.
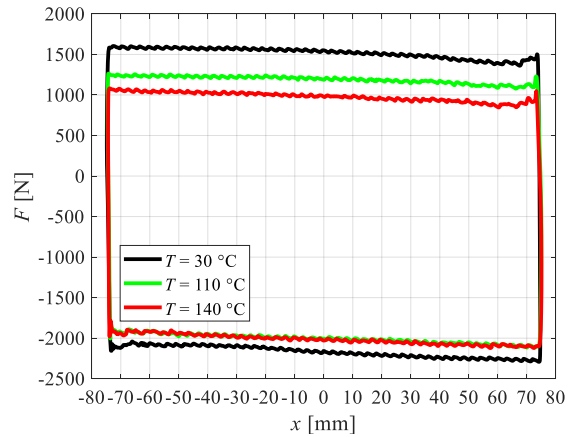

Fig. 13. Force vs piston position at various coil temperatures; piston excitation A = 75 mm, f = 0.5 Hz, current I = 5 A
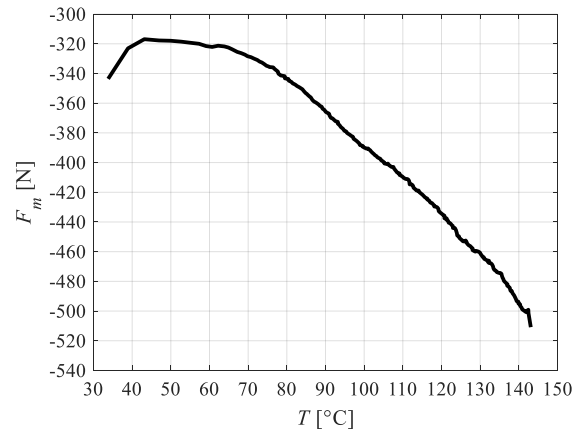
Fig. 14. Force mean value vs coil temperature; piston excitation A = 75 mm, f = 0.5 Hz, current I = 5 A
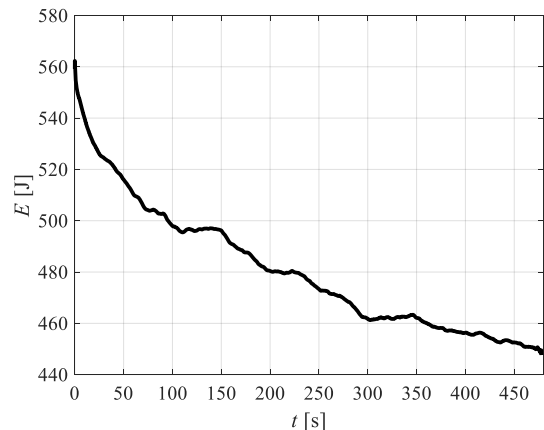
Fig. 15. Time pattern of dissipated energy; piston excitation A = 75 mm, f = 0.5 Hz, current I = 5 A

Fig. 17 gives the plots of average dissipated power and instantaneous electric power supplied to the control coil, in the function of time. Like the dissipated energy (Fig. 15), the average dissipated power P_m tends to decrease, which is attributable to increase in the MR fluid temperature. In order to maintain a constant current level in the control coil whilst its resistance R increases with time, it is required that the power P_{el} supplied from

Łukasz Jastrzębski, Bogdan Sapiński, Arkadiusz Kozieł
Automotive MR Shock Absorber Behavior Considering Temperature Changes: Experimental Testing and Analysis

DOI 10.2478/ama-2020-0004

the current driver should be increased. In the course of the experiment, the temperature of the control coil rose by 110 ºC, which caused a 20% reduction of the averaged dissipated power P_m and a 38% increase of electric power P_{el} supplied to the control coil.
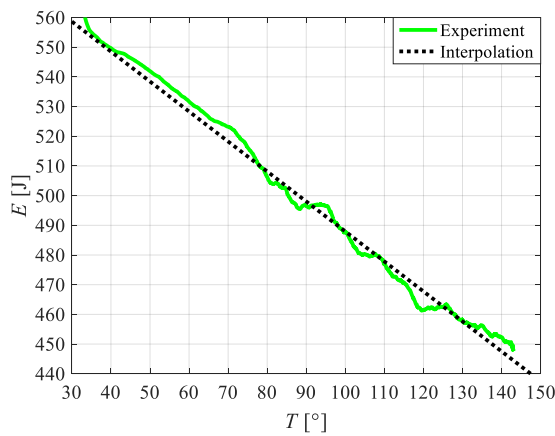
Fig. 16. Dissipated energy vs coil temperature; piston excitation
A = 75 mm, f = 0.5 Hz, current I = 5 A
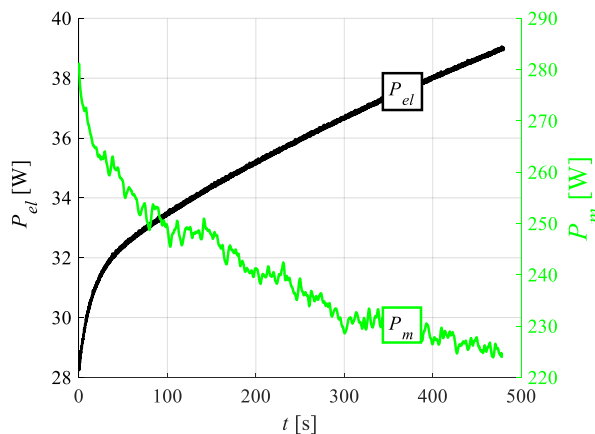
Fig. 17. Time patterns of electrical and mechanical power;
piston excitation A = 75 mm, f = 0.5 Hz, current I = 5 A

5. SUMMARY

The study investigates the temperature dependence of the Magnetic Ride absorber behaviour, focusing on the following aspects: temperature dependence of control coil resistance in the device, the influence of operating current on control coil temperature and temperature dependence of force response and energy dissipated in the system.

The experimental results led us to the following conclusions:

– Resistance of the control coil is found to be linearly related to temperature, hence the coil temperature can be established through direct measurements of voltage and current levels.

– When no excitations are applied, thermal energy released by the flow of current less than 2 A will not significantly affect the coil temperature, whilst for the current level 5 A, after 50 s, the difference between the coil temperature and that of the cylinder would approach 35 ºC.

– At currents in excess of 2 A, the rate of coil temperature increase is significantly reduced after 50 s, no matter whether the piston was in motion or remained immobile.

– At a current level 5 A and piston motion velocity 150 mm/s,

thermal energy released within the time period of 180 s caused the coil temperature to increase threefold.

– When the coil temperature went up from 30 ºC to 140 ºC, the absolute value of the average absorber force response increased by 50%, which was attributable to an increase in the temperature of gas in the accumulator.

– Under the same conditions, a nearly 20% decrease of dissipated energy and power was registered, whilst the electric power demand increased by 38%.

REFERENCES

1. **Bajkowski J., Skalski P.** (2012), Analysis of Viscoelastic Properties of a Magnetorheological Fluid in a Damper, Acta Mechanica et Automatica, 6(3), 5–410.
2. **Batterbee D., Sims N. D.** (2009), Temperature Sensitive Controller Performance of MR Dampers, Journal of Intelligent Material Systems and Structures, 20, 297–309
3. **Choi S. B., Han S. S., Han Y. M.** (2005), Vibration Control of a Smart Material Based Damper System Considering Temperature Variation and Time Delay, Acta Mechanica, 180(1–4), 73–82.
4. **FLIR Systems Inc.** (2019), *User's manual FLIR Exx series,* Technical Documentation ,https://www.flir.eu
5. **FLUKE Corp.** (2019), *8845A/8846A Digital Multimeter. Users Manual.* Technical Documentation, http://www.fluke.com
6. **Gołdasz J., Sapiński B.** (2019), Influence of temperature on the MR squeeze-mode damper, Proceedings of 20th International Carpathian Control Conference ICCC 2019.
7. **Gołdasz J., Sapiński B., Jastrzębski Ł**. (2018), Assessment of the Magnetic Hysteretic Behaviour of MR Dampers through Sensorless Measurements, vol. 2018, Article ID 3740208, 21 pages.
8. **Gordaninejad F., Breese D. G.** (1999), Heating of Magnetorheological Fluid Dampers, Journal of Intelligent Material Systems and Structures, 10(8), 634–645.
9. **INTECO Ltd.** (2019), *RT-DAC4/PCI Multi I/O board. User's Guide*, Technical Documentation, http://www.inteco.com.pl
10. **Jastrzębski Ł., Sapiński B.** (2017), Experimental Investigation of an Automotive Shock Absorber, Acta Mechanica et Automatica, 11(4), 253–259.
11. **Kubik M., Gołdasz J.** (2019), Multiphysics Model of an MR Damper including Magnetic Hysteresis, Shock and Vibration, Article ID 3246915, 20 pages.
12. **McKee M., Gordaninejad F., Wang X.** (2018), Effects of temperature on performance of compressible magnetorheological fluid suspension systems, Journal of Intelligent Material Systems and Structures, 29(1), 41–51.
13. **MTS System Corp.** (2019), *MTS 810 & 858 Material Testing Systems,* Technical Documentation, http://www.mts.com
14. **Sapiński B., Jastrzębski Ł., Rosół M.** (2012), Power amplifier supporting MR fluid-based actuators, Proceedings of 13th International Carpathian Control Conference ICCC 2012, 612–616.
15. **Sims N. D.** (2006), Limit Cycle Behaviour of Smart Fluid Dampers under Closed-loop Control, Journal of Vibration and Acoustics, 128(4), 413–428.
16. **Strecker Z**., **Roupec J**., **Mazurek I**., **Klapka M.**, (2015), Limiting factors of the response time of the magnetorheological damper, International Journal of Applied Electromagnetics and Mechanics, 47(2), 541–550.
17. **WEISS TECHNIK.** (2019), Climate Test Chamber, Technical Documentation, https://www.weiss-technik.com

MODELLING OF THE LOW-PRESSURE GAS INJECTOR OPERATION

Dariusz SZPICA, Michał KUSZNIER

Faculty of Mechanical Engineering, Bialystok University of Technology, ul. Wiejska 45C, 15-351 Białystok, Poland

d.szpica@pb.edu.pl, michal.kusznier@gmail.com

Abstract: In recent years, there has been a growing interest in alternative sources of power supply for internal combustion engines. Liquefied petroleum gas injection systems are among the most popular. It becomes necessary to know mathematical descriptions of the operation of individual components. The article presents a mathematical model that describes the operation of the low-pressure gas injector. Valtek plunger injector was chosen as the test object. The mathematical description includes three parts, i.e. electric, mechanical and pneumatic. The electrical part describes the generation of electromagnetic force by a circuit with a coil, in the mechanical equilibrium equation of forces acting on the plunger, and in the pneumatic part the air pressure on the plunger. The calculations were performed in the Matlab/Simulink environment, creating current waveforms, acting forces and plunger displacement. Correctness of mathematical description and determined in the course of opening and closing time calculations were related to the values declared by the manufacturer, showing differences below 3%. The presented mathematical model can be modified for other injector design solutions.

Key words: Mechanical Engineering, Combustion Engines, Alternative Fuel Supply, Modelling

1. INTRODUCTION

In recent years, natural oil deposits have been exploited at a rapid rate, resulting in rising fuel prices on international markets, and consequently, the number of engines powered by alternative liquefied petroleum gas (LPG) is growing year on year. (Raslavičius et al., 2014). The use of LPG as a fuel dates back to the beginning of the 20th century, and with the development of motorisation, the popularity of this fuel is growing. Manufacturers of gas systems and their components are required to meet the homologation requirements. Regardless of the original fuel system (carburettor, direct and indirect injection) or general trends like downsizing (Leduc et al., 2003), the alternative fuel supply must meet the emission requirements at the point of homologation (Ristovski et al., 2005; Mustafa and Gitano-Briggs, 2009). The problem is the successive tightening of emission standards for internal combustion engines used in transport (Bielaczyc and Woodburn, 2018), non-road and working machines (Waluś et al., 2018; Warguła et al., 2020). The tightening of emission standards is accompanied by changes in the organisation of driving tests (Bielaczyc and Woodburn, 2018). This forces manufacturers to constantly search for new solutions in the structure of the combustion process (Onishi et al., 1979; Jeuland et al., 2004; Mikulski et al., 2018) or the drive sources (Dimitrowa and Marechal, 2015; Grigor`ev et al., 2015; Raslavičius et al., 2017; Simon, 2017).

The required condition for proper operation of the gas injection system is evenness (Szpica, 2018a) and repeatability (Szpica, 2018) of injector dosage. In order to properly dose the fuel, injectors with specific flow parameters, operation delay and durability are required (Czarnigowski, 2012; Borawski, 2015). Therefore, already in the course of construction, the gas injector should meet certain requirements, and mathematical modelling should be used for preliminary tests.

There is a growing interest in computational methods that allow testing virtual prototypes of new solutions. The possibilities of solving mathematical dependencies, similarly as in general technical issues, are searched for using dedicated software for analytical or numerical calculations (Mieczkowski et al., 2007; Mikulski et al., 2015; Marczuk et al., 2019; Brumercik et al., 2020). An alternative to this procedure is to use specialised software based on finite element method (FEM) (Bensetti et al., 2006; Cheng et al., 2014; Mieczkowski et al., 2020) or computational fluid dynamics (CFD) (Wendeker et al., 2007; Czarnigowski et al., 2009). Similarly, with the modelling of the working cycle of an LPG engine, it can be solved in an analytical (Cao et al., 2007) or numerical (Pulawski and Szpica, 2015) way.

The fuel injector in its mathematical description focuses on many aspects. In the execution part, there is a coil with a circuit generating electromagnetic field causing valve movement (Passarini and Nakajima, 2003; Passarini and Pinotti, 2003) or piezoelectric drive (Pogulayev et al., 2015; Mieczkowski, 2019; Mieczkowski, 2019a). In the mechanical part, the motion of the actuator element is analysed (Lim et al., 1994) and related to friction (Borawski, 2018, 2019) along with aerodynamic drag. Hydraulic aspects concern the process of flow through the cycle working valve (Czarnigowski et al., 2007; Marčič et al., 2015). A separate part in modelling of the fuel injector operation process is formed by the issues of electric power supply. The specificity of the signal controlling the opening of the fuel injector is based on a transistor key, which is also designed to limit the power supply to prevent overheating of the injector (Hung and Lim, 2019). For this purpose, a pulse-width modulation (PWM) signal is used some time after the opening is initiated (Taghizadeh et al., 2009; Szpica, 2016). Each time a fuel injector is modelled, input data is required to determine the geometry, electrical, mechanical or hydraulic processes.

Due to the lack of a comprehensive mathematical model describing the operation of the low-pressure gas injector, an attempt

was made to create it. Considering some limitations, especially in the mathematical description of the electromagnetic field generated by the coil with moving core, an empirical model was proposed. The goal was also to show the influence of particular factors shaping plunger displacement. On this basis, the factors of minor importance may be omitted in the course of model simplification. The presented approach allows to develop, based on the proposed mathematical description, models of varying degrees of complexity and possible extensions.

2. THE RESEARCH OBJECT

The object of the research was Valtek Rail Typ 30 low pressure gas injector (Fig. 1). This is a plunger type injector with a transverse flow. The plunger movement is caused by an electromagnetic circuit that includes coil and cramp. The spring is responsible for plunger contact with the corps at standstill. The plunger movement is bounded by a limiter. The gas flows from the inlet nozzle to the outlet nozzle when the coil is electrically powered and the plunger is moved. The plunger has elastic feet mounted at the bottom and top.
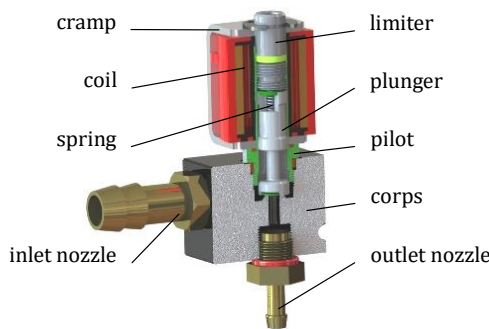

Fig. 1. Valtek Rail Typ 30 gas injector

Basic technical data of the Valtek injector have been presented in Table 1.

Tab. 1. Basic technical data of the Valtek Rail Typ 30 gas injector (https://www.valtek.it/...)

Parameter	Unit	Value
Coil resistance	Ω	3
Plunger displacement	mm	0.4
Nozzle size	mm	Min. 1.5 / Max. 3.5
Opening time	ms	3.4
Closing time	ms	2.2
Max. working pressure	Pa	4.5 $e5$

3. MODELLING METHODOLOGY

The mathematical modelling of the low-pressure gas injector can be based on mathematical descriptions of electrovalves from pneumatic actuators (Rahman et al., 1996a, 1996b; Chu et al., 2007; Kamiński, 2013, 2014) or liquid fuel injectors. In case of fuel injectors, the models can be divided into physical zero, single or multi-dimensional (Matković et al., 2005; Czarnigowski et al., 2007; Ouyang, 2009; Minghai and Feng, 2010; Li and Jiang,

2010) and empirical (Duk and Czarnigowski, 2001; Mehlfeldt et al., 2008; Yang et al., 2012, Borawski, 2015a). The issues mainly concern the movement of the injector's execution element, which in effect determines the mass of fuel that flows out of it (Morselli et al., 2002; Mehlfeldt et al., 2008; Liu and Ouyang, 2009; Li and Jiang, 2010; Haiping and Xianyi, 2010). All mathematical models emphasise the existence of time delays resulting mainly from inertia forces and resistance to motion of the executive element in the ratio of a given impulse to fuel outflow (Szpica, 2017).

The mathematical description of the function of the low-pressure gas injector is based on Fig. 2.
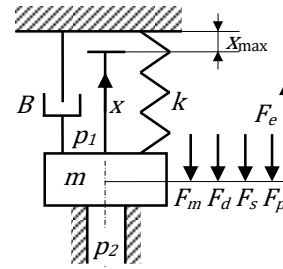

Fig. 2. The scheme of the gas injector (description in the main text)

Due to the high complexity of the mathematical description, the following simplifying approaches were assumed:
- the plunger movement is caused by the result of acting forces (the reflection effect in the return positions is omitted);
- body vibrations and other mechanical disturbances do not affect the plunger movement;
- eddy currents, magnetic saturation and coil temperature do not affect the parameters of the electromagnetic circuit;
- the pressing force coming from the air pressure depends on the plunger position;
- friction is divided into static, kinetic and viscous and its value depends on plunger movement (coefficient values do not depend on temperature and pressure inside the body);
- the aerodynamic drag force of the plunger is included;
- due to the complexity of construction, the inductance of the electromagnetic circuit will be determined experimentally;
- stiffness of the pressure spring will be determined experimentally, vibrations will be omitted.

The equation of equilibrium on this basis (Fig. 2) can be written down in the form:

$$F_m + F_d + F_s + F_p = F_e \tag{1}$$

where F_m is the resistance force of mass inertia, F_d the friction force, F_s the spring force, F_p the pressure force and F_e is the electromagnetic force.

The resistance force of mass inertia in reciprocating motion inertial force is described as:

$$F_m = m \frac{\mathrm{d}^2 x}{\mathrm{d}t^2} \tag{2}$$

where m is the mass of the moving element.

In the case of injector plunger movement, damping (B in Fig. 2) may be the result of friction between plunger and corps as well as gas and aerodynamic drag force. Despite the fact that the electromagnetic system should align the plunger, it is assumed that under horizontal mounting conditions, the plunger will press its weight on the pilot.

The damping force is described as:

$$F_d = \begin{cases} F_{fs} & \text{if } x = 0, x = m_{\max} \\ F_{fk} + F_v + F_{df} & if \ x \neq 0 \end{cases} \quad (3)$$

where $F_{fs} = \mu_s F_N$ is the force of static friction, F_N the normal force, $F_{fk} = \mu_k F_N$ the force of kinetic friction, $F_v = \mu_v \frac{\mathrm{d}x}{\mathrm{d}t} \mathrm{sgn}(x)$ the force of viscous friction, $F_{df} = 0.5 \, A \, c_d \rho \, v^2 \mathrm{sgn}(x)$ the force of aerodynamic drag, μ_s the coefficient of static friction, μ_v the coefficient of viscous friction, μ_k the coefficient of kinetic friction, c_d the drag coefficient, ρ the density of air, $v = \frac{\mathrm{d}x}{\mathrm{d}t}$ the flow velocity and A is the characteristic frontal area of the body.

The spring force is described as:

$$F_s = k(x_0 + x) \quad (4)$$

where k is the spring stiffness, x the displacement element and x_0 is the initial tension of the spring.

The pressure force is given as:

$$F_g = \begin{cases} A_1 p_1 + A_2 p_2 & if \ x = 0 \text{ mm} \\ 0 & if \ x > 5e - 7 \text{ mm} \end{cases} \quad (5)$$

where A_1 is the cross area over the valve, p_1 the gas pressure, A_2 the cross area under the valve and p_2 is the inlet manifold pressure.

The electromagnetic force being the result of the circuit operation can be obtained from the relation:

$$F_e = \frac{1}{2} I^2 \frac{\mathrm{d}L(x)}{\mathrm{d}x} \quad (6)$$

where I is the current and L is inductance.

Using the Faraday`s and Kirchhoff`s laws, one may obtain a differential equation describing the change of the current supplying the electromagnetic circuit:

$$\frac{\mathrm{d}I}{\mathrm{d}t} = \frac{1}{L(x)}\left(U - RI - \frac{\mathrm{d}L(x)}{\mathrm{d}x}\frac{\mathrm{d}x}{\mathrm{d}t}I\right) \quad (7)$$

where R is the resistance and U is the voltage.

Then, substituting all components to Eq. 1, we will obtain an equation of equilibrium that is as follows:

$$a = \frac{\mathrm{d}v}{\mathrm{d}t} = \frac{F_e - F_m - F_d - F_s - F_p}{m} \quad (8)$$

To solve Eq. 8, numerical methods are used and a dedicated software is needed. The calculation process is dependent on the values of input parameters and boundary conditions. There are two options to deal with boundary conditions. In the first simpler variant, hard plunger displacement limits are defined (Borawski, 2015a) in the second variant, it is necessary to describe meticulously mechanical collisions (Tian and Zhao, 2018). The hard constraints are realised by the correct setting of the integrating integrator, while the description of mechanical collisions is a complex system of switch commands. The second variant also allows for more precise modelling of the plunger rebound event in the turning positions.

4. NECESSARY PARAMETER TO INITIATE CALCULATION

In case of controlling the opening of the gas injector, a transistor key is used and the voltage course is specific for the so-called short to ground (Szpica, 2018b). Therefore, this type of extortion should be reversed as an input value in the model, bypassing the part of the voltage drop, where overvoltage occurs in the opposite direction to extortion. Finally, the extortion signal is defined as a rectangle with the height equal to the value of the supply voltage and the length resulting from the opening time.

One of the most important parameters required to initiate calculations is the relation between the inductance of the electromagnetic system and the plunger displacement. There are many analyses in the literature to calculate this parameter dependent on coil parameters and installation geometry. The calculations are based on empirical and numerical models (Pacurar et al., 2015; Bali and Erzan Topcu, 2018). The studies mainly focus on air coils without considering the internal core movement (Lu and Jensen, 2003; Xiang et al., 2008; Plavec et al., 2019; Taghizadeh et al., 2009; Dongiovanni and Coppo, 2010; Cheng et al., 2015). In mathematical descriptions that take into account the movable core, there is no clear experimental verification (Cheung at al., 1993; Cvetkovic et al., 2008; Liu et al., 2011; Lunge and Kurode, 2013; Li et al., 2017; Tian and Zhao, 2018; Demarchi et al., 2018). There are no guidelines for determining the inductance of an electromagnetic circuit, taking into account the construction conditions and characteristics of the materials used.

This is why it was decided to use the results of the experimental research included in Szpica (2016a). The values were measured RLC CMT-417 Meter and a special test will be used at 100 Hz pulse frequency. The measurement results are presented in Fig. 3. The relation $L = f(x)$ was approximated with the polynomial of 3rd degree achieving the compliance, which is confirmed by the value $R^2 = 99.9 \%$. On the result of the approximation dependence, a derivative was determined:

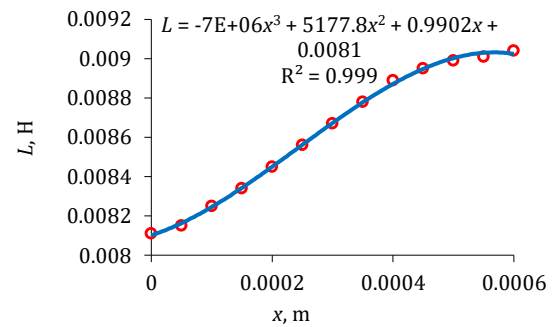$$\frac{\mathrm{d}L(x)}{\mathrm{d}x} = -21\mathrm{e}6x^2 + 10355.6x + 0.990 \quad (9)$$

Fig. 3. Test results on inductance as a function of the lift of the injector working component

Due to the complicated shape of the pressure spring, its rigidity was determined experimentally. For this purpose, the AXIS FB50 50 N with tripod and MITUTOYO altimeter was used, as well as the measuring range including working stroke and preload. The measurement results are presented in Fig. 4. The trend line was linearly approximated to a stiffness of 832.83 N/m ($R^2 = 99.9 \%$).

The parameters needed to initiate the simulation have been presented in Table 2. At the input, the voltage control pulse was set in the form of a rectangular run. At $t = 0 \text{ s}$, the voltage reached $U = 12 \text{ V}$ and the plunger was in the position $x = 0 \text{ m}$. After the time $t = t_{inj}$, the voltage dropped in steps to $U = 0 \text{ V}$. The integrating integrator of displacements had been set to a limit value of $x_{\max}$.
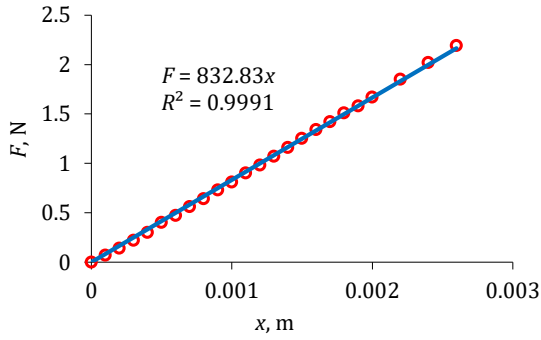
Fig. 4. Test results on the spring stiffness

Tab. 2. Parameters, functions and conditions needed to initiate the simulation

Parameter	Volume
Injection time	$t_{inj} = 5$ ms
Mass of the piston and needle	$m = 5e - 3$ kg
Resistance	$R = 3\ \Omega$
Inductance function	Fig. 3 and Eq. 9
Spring stiffness	Fig. 4
Initial tension the spring	$x_0 = 0.75$ mm
Coefficient of static friction	$\mu_s = 0.61$
Coefficient of kinematic friction	$\mu_k = 0.47$
Coefficient of viscous friction	$\mu_v = 0.009$ Ns/m
Coefficient of aerodynamic drag	$c_d = 1$
Normal force	$F_N = m\ g$
Characteristic frontal area of the body, cross area over the valve	$A = A_1 = 32.56e - 6$ m^2
Cross area under the valve	$A_2 = 12.56e - 6$ m^2
Gas pressure	$p_1 = 1e5$ Pa $+ p_2$
Inlet manifold pressure	$p_2 = 1e5$ Pa
Density of air	$\rho = 1.2$ kg/m^3

5. RESULTS OF THE SIMULATION

By twice integrating the relation Eq. 8, we will obtain a displacement of the piston. It allows conducting calculations of the gas injector operation in the entire cycle, i.e. opening, holding the open position and closing. The differential Eq. 8 was solved numerically with the implicit trapezoidal method combined with reverse differentiation (variable steps, min. step $1e - 7\ s$) in Matlab/Simulink (Yang et al., 2005). This software allows for easy implementation of empirical models in workspace, which has been confirmed in studies (Shamdani et al., 2006; Borawski, 2015a; Demarchi et al., 2018).

As a result of the simulations, it is possible to evaluate the correctness of the mathematical description on the basis of the voltage U, current I and displacement x (Fig. 5).

Analysing the course in Fig. 5, it can be seen that the injector starts opening with a delay of $t_{ro} = 2.17$ ms and the opening process itself takes $t_o = 1.30$ ms. The current course is visible when the injector reaches complete opening. After a power cut, the injector closes. The exact time to fully open $t_{fo} = 3.47$ ms and to fully close $t_{fc} = 2.15$ ms is read from the graph.
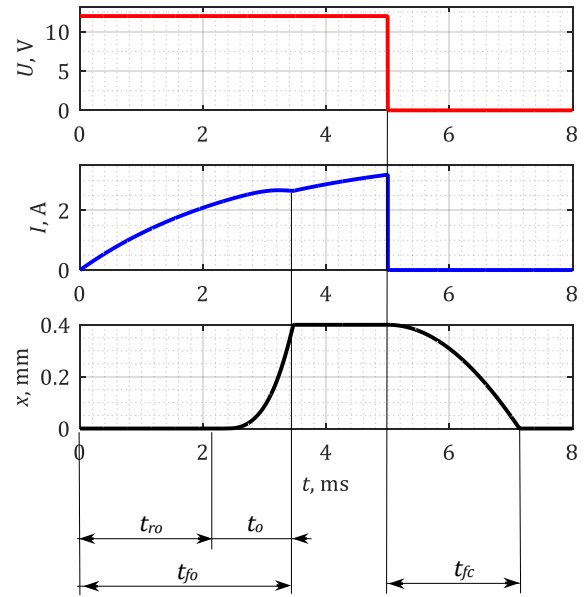

Fig. 5. The results of the simulation: t_{ro} – opening response times, t_o – opening times, t_{fo} – full opening times, t_{fc} – full closing times

Presented in Eq. 1 the balance of forces acting on the plunger determines its movement. As can be seen in Fig. 6, the initial phase of the injector's operation marked as A is the overcoming by the electromagnetic force F_e of air pressure F_p, spring force F_s and static friction force F_{fs}.
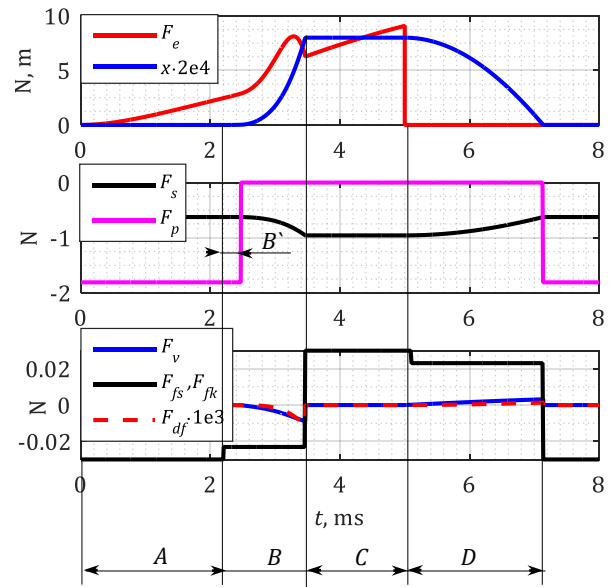
Fig. 6. Course of the forces and displacement
(description in the main text)

At the start of the movement, the static friction force F_{fs} changes into the kinetic friction force F_{fk}, and after time $B`$, the force F_p disappears. During the displacement of the plunger (B in Fig. 6), the viscous friction force F_v and the aerodynamic drag force F_{df} are added as load, which change their turn in the return motion, just like F_{fk}, and the plunger inertia. In section C, only the

electromagnetic force increases because the plunger is stationary. At closure (D in Fig. 6), the spring's stiffness is responsible for the return motion, and it determines this process, since the electromagnetic force F_e fades away in steps. To sum up Fig. 6, it should be stated that the dominant forces are the electromagnetic force F_e, the air pressure force F_p, the spring force F_s and the plunger inertia. The remaining forces have little influence on the opening and closing process of the injector, especially the viscous friction force F_v and the aerodynamic drag force F_{df}.

The injector opening and closing times calculated in the course of analysis were compared with those declared by the manufacturer (Table 3). It was found that full opening time differs by 2.05 % and full closing time by 2.27 % from the manufacturer's declaration, which should be considered an acceptable result. In the case of the opening process, the reason for this difference can be assumed to be the acceptance of a force loss in steps from the pressure F_p to the set value of the lift x. In addition, the inductance was determined at a certain frequency, which may also affect the calculation results. In the case of the closing process, the power cut may have been influenced by the power drops, which, however, fall with some slight delay (Szpica, 2017).

Tab. 3. The technical data and calculated comparison

Parameter	Technical data (ms)	Calculated (ms)	Absolute error (%)
Full opening time	3.40	3.47	2.05
Full closing time	2.20	2.15	2.27

In the course of further activities, it is planned to implement the model presented in the study to other injector design solutions, including plate and membrane. In these cases, the model descriptions of electromagnetic circuits available in the literature should be considered more accurately. Additionally, it is planned to develop a mathematical model of the electromagnetic circuit, which can be used in modelling of the operation of the low pressure gas injector without the need for experimental determination. The final requirement will be to carry out an experimental validation of the simulation results using sensors that do not interfere with the injector's electromagnetic field generating system.

6. CONCLUSIONS

The article describes the course of mathematical modelling of the low-pressure gas injector. The overall mathematical model consists of several parts: electrical, mechanical and hydraulic. In the electrical part, the process of rising and falling of the supply current depending on the supply voltage and magnetic properties of the circuit with the coil is described. In the mechanical part, inertia and frictional resistances and aerodynamics are taken into account, also taking into consideration the spring return pressure. Hydraulic part is the pressure force on the plunger coming from the air pressure, which is assumed in the model as the working medium. The calculations were carried out in the Matlab/Simulink environment, and the Valtek Rail Type 30 injector was selected as the object.

On the basis of the work carried out, the following conclusions can be made :

– The proposed mathematical description of the operation of the low-pressure gas injector allows to simulate its operation.

– The use of experimental results and their implementation into an empirical model seems to be useful in modelling a complex electromagnetic system with a coil and a movable core.

– The movement of the working element of the gas injector (plunger) is determined by the electromagnetic force, inertia, pressure and spring.

– Little influence of frictional and aerodynamic drag on the process of opening and closing the gas injector has been noticed.

– The results showed that full opening time differs by 2.05 % and full closing time by 2.27 %, which gives grounds to consider the proposed model to be correct.

Some imperfections in the mathematical description were noticed which may influence the results. This is a reason for further mathematical analyses and the necessity to carry out partial experimental research, i.e. electromagnetic force acting on the plunger, frictional resistances and others.

REFERENCES

1. **Bali E., Erzan Topcu E.** (2018), Design of on-off type solenoid valve for electropneumatic brake system and investigation of its statistics characteristics, *International Journal of Advances on Automotive and Technology*, 2(3): 175–184.
2. **Bensetti M., Bihan Y.L., Marchand C.** (2006), Development of an hybrid 3D FEM for the modeling of micro-coil sensors and actuators, *Sensors and Actuators A: Physical*, 129(1): 207–211.
3. **Bielaczyc P., Woodburn J.** (2018), Trends in automotive emissions legislation: impact on LD engine development, fuels, lubricants, and test methods - a global view, with a focus on WLTP and RDE regulations - Summary of the 6th International Exhaust Emissions Symposium (IEES), *Combustion Engines*, 174(3): 56–65
4. **Borawski A.** (2015), Modification of a fourth generation LPG installation improving the power supply to a spark ignition engine, *Eksploatacja i Niezawodnosc – Maintenance and Reliability*, 17(1): 1–6.
5. **Borawski A.** (2015a), Simulation studies of LPG injector used in 4th generation installations, *Combustion Engines*, 160(1): 49–55.
6. **Borawski A.** (2018). Simulation Study of the Process of Friction in the Working Elements of a Car Braking System at Different Degrees of Wear. Acta Mechanica et Automatica, 12(3): 221–226.
7. **Borawski A.** (2019), Common methods in analysing the tribological properties of brake pads and discs - a review, *Acta Mechanica et Automatica*, 13(3): 189–199.
8. **Brumercik F.; Lukac M.; Caban J. Krzysiak Z.; Glowacz A.** (2020), Comparison of selected parameters of a planetary gearbox with involute and convex–concave teeth flank profiles, *Applied Science*, 10: 1417.
9. **Cao Y., Teng W., Zhang H.** (2007), Dynamic modeling and hardware-in-the-loop simulation testing for LPG engine, *Proceedings of the 2007 IEEE International Conference on Mechatronics and Automation*, 2093–2098.
10. **Cheng Q., Zhang Z.-D., Guo H., Xie N.-L.** (2015), Electro-magnetic-thermal coupling of GDI injector, *Journal of Jilin University (Engineering and Technology Edition)*, 45(3): 806–813
11. **Cheng Q., Zhang Z-D., Guo H., Xie N-L.** (2014), Simulation and analysis on electro-magnetic-thermal coupling of solenoid GDI injector, *International Journal of Applied Electromagnetics and Mechanics*, 46(4): 775–792.
12. **Cheung N.C., Lim K.W., Rahman M. F.** (1993), Modelling a linear and limited travel solenoid, *Proceedings of IECON '93 - 19th Annual Conference of IEEE Industrial Electronics*, 3: 1567–1572.
13. **Chu L., Hou Y., Liu M., Li J., Gao Y., Ehsani M.** (2007), Study on the dynamic characteristics of pneumatic ABS solenoid valve for commercial Vehicle, *2007 IEEE Vehicle Power and Propulsion Conference*, 641–644.

14. **Cvetkovic D, Cosic I., Subic A.** (2008), Improved performance of the electromagnetic fuel injector solenoid actuator using a modelling approach, *International Journal of Applied Electromagnetics and Mechanics*, 27: 251–273.

15. **Czarnigowski J.** (2012), *Teoretyczno-empiryczne studium modelowania impulsowego wtryskiwacza gazu*, Wydawnictwo Politechniki Lubelskiej, Lublin.

16. **Czarnigowski J., Jaklinski P., Wendeker M., Pietrykowski K., Gabowski Ł.** (2009), The analyses of the phenomena inside a CNG flap-valve injector during gas flow. *Combustion Engines*, 1(136): 10–18.

17. **Czarnigowski J., Wendeker M., Jakliński P., Rola M., Grabowski Ł., Pietrykowski K.** (2007), CFD model of fuel rail for LPG systems, *JSAE/SAE International Fuels & Lubricants Meeting*, 2007-01-2053.

18. **Demarchi A., Farçoni L., Pinto A., Lang R., Romero R., Silva I.** (2018), Modelling a solenoid's valve movement, In: Akiyama H., Obst O., Sammut C., Tonidandel F. (eds) *RoboCup 2017: Robot World Cup XXI. RoboCup 2017. Lecture Notes in Computer Science*, Cham: Springer, 11175.

19. **Dimitrova Z., Maréchal F.** (2015), Gasoline hybrid pneumatic engine for efficient vehicle powertrain hybridization, *Applied Energy*, 151: 168–177.

20. **Dongiovanni C., Coppo M.** (2010), *Accurate Modelling of an Injector for Common Rail Systems*. In book: Siano D. *Fuel Injection*, London: IntechOpen Limited, 6: 95–119.

21. **Duk M., Czarnigowski J.** (2001), The method for indirect identification gas injector opening delay time, *Przeglad Elektrotechniczny*, 88(10b): 59–63.

22. **Grigor'ev M.A., Naumovich N.I., Belousov E.V.** (2015), A traction electric drive for electric cars, *Russian Electrical Engineering*, 86(12): 731–734.

23. **Haiping Y., Xianyi Q.** (2010), The calculation of main parameters of the gasoline engine fuel injection system, *Proceeding of the International Conference on Computer Application and System Modeling (ICCASM)*, V13–635.

24. **Hung N.B., Lim O.T.** (2019), Improvement of electromagnetic force and dynamic response of a solenoid injector based on the effects of key parameters, *International Journal of Automotive Technology*, 20: 949-960.

25. **Jeuland N., Montagne X., Duret P.** (2004), New HCCI/CAI combustion process development: Methodology for determination of relevant fuel parameters, *Oil & Gas Science and Technology*, 59(6): 571–579.

26. **Kamiński Z.** (2013), Experimental and numerical studies of mechanical subsystem for simulation of agricultural trailer air braking systems, *International Journal of Heavy Vehicle System*, 20(4): 289–311.

27. **Kamiński Z.** (2014), Mathematical modelling of the trailer brake control valve for simulation of the air brake system of farm tractors equipped with hydraulically actuated brakes, *Eksploatacja i Niezawodnosc – Maintenance and Reliability*, 16(4): 637–643.

28. **Leduc L., Dubar B., Ranini A., Monnier G.** (2003), Downsizing of gasoline engine: an efficient way to reduce CO2 emissions. *Oil & Gas Science Technology*, 58(1): 115–127.

29. **Li P.X., Su M., Zhang D.B.** (2017), Response characteristic of high-speed on/off valve with double voltage driving circuit, *IOP Conference Series: Materials Science and Engineering*, 220: 012028.

30. **Lim K.W., Cheung N.C., Kahman M.F.** (1994), Proportional control of a solenoid actuator, *Proceedings of IECON'94 - 20th Annual Conference of IEEE Industrial Electronics*, 2045–2050.

31. **Liu Y.-F., Dai, Z.-K., Xu X.-Y., Tian L.** (2011), Multi-domain modeling and simulation of proportional solenoid valve, *Journal of Central South University Technology*, 18: 1589–1594.

32. **Liu Z., Ouyang G.** (2009), Numerical analysis of common rail electro-injector for diesel engine, *Proceedings of the International 2009 Conference on Mechatronics and Automation (IEEE)*, 1683–1688.

33. **Lu F., Jensen D.** (2003), Potential viability of a fast-acting micro-solenoid valve for pulsed detonation fuel injection, *41st Aerospace Sciences Meeting and Exhibit, Aerospace Sciences Meetings*, 2003-0888.

34. **Lunge, S.P., Kurode S.R.** (2013), Proportional actuator from on off solenoid valve using sliding modes, *Proceedings of the 1st International and 16th National Conference on Machines and Mechanisms (iNaCoMM2013)*, 1020–1027.

35. **Marčič S., Marčič M., Praunseis Z.** (2015), Mathematical Model for the Injector of a Common Rail Fuel-Injection System. *Engineering*, 7: 307–321.

36. **Marczuk A., Caban J., Aleshkin A.V., Savinykh P.A., Isupov A.Y., Ivanov I.I.** (2019), Modeling and simulation of particle motion in the operation area of a centrifugal rotary chopper machine, *Sustainability*, 11(18): 1–15.

37. **Matković K., Jelović M., Jurić J., Konyha Z., Gračanin D.** (2005), Interactive visual analysis and exploration of injection system simulations, *Proceedings of the International Conference on Vizualization (VIS 05. IEEE)*, 391–398.

38. **Mehlfeldt D., Weckenmann H., Stöhr G.** (2008), Modeling of piezoelectrically actuated fuel injectors, *Mechatronics*, 18: 264–272.

39. **Mieczkowski G.** (2019), Criterion for crack initiation from notch located at the interface of bi-material structure, *Eksploatacja i Niezawodnosc – Maintenance and Reliability*, 21 (2): 301–310.

40. **Mieczkowski G.** (2019a), Static electromechanical characteristics of piezoelectric converters with various thickness and length of piezoelectric layers, *Acta Mechanica et Automatica*, 13(1): 30–36.

41. **Mieczkowski G., Borawski A., Szpica D.** (2020), Static electromechanical characteristic of a three-layer circular piezoelectric transducer, *Sensors*, 20, 222.

42. **Mieczkowski G., Molski K., Seweryn A.** (2007), Finite-element modeling of stresses and displacements near the tips of pointed inclusions, *Materials Science*, 43(2): 183–194.

43. **Mikulski M., Balakrishnan P.R., Doosje E., Bekdemir C.** (2018), Variable valve actuation strategies for better efficiency load range and thermal management in an RCCI engine, *SAE Technical Papers*, 2018-01-0254.

44. **Mikulski M., Wierzbicki S., Piętak A.** (2015), Numerical studies on controlling gaseous fuel combustion by managing the combustion process of diesel pilot dose in a dual-fuel engine, *Chemical and Process Engineering*, 36(2): 225–238.

45. **Li M.H., Jiang F.** (2010), Simulation research on fuel injection system of 16V265H Dielsel engine introduced from U.S., *Proceedings of the International Conference on E-Product E-Service and E-Entertainment (ICEEE)*, 4796–4799.

46. **Morselli R., Corti E., Rizzoni G.** (2002), Energy based model of a common rail injector, *Proceeding of the International Conference on Control Applications (IEEE)*, 2: 1195–1200.

47. **Mustafa K.F., Gitano-Briggs H.W.** (2009), Liquefied petroleum gas (LPG) as an alternative fuel in spark ignition engine: Performance and emission characteristics. *Proceedings of the International Conference Energy and Environment (ICEE)*, 189–194.

48. **Onishi S., Jo S.H., Shoda K., Jo P.D., Kato S.** (1979), Active thermo-atmosphere combustion (A.T.A.C.) - A new combustion process for internal combustion engines, *SAE Paper*, 790501.

49. **Pacurar C., Topa V., Munteanu C., Racasan A., Hebedean C., Oglejan R., Vlad G.** (2015), Solenoid actuator parametric analysis and numerical modeling, *Acta Electrotehnica*, 56(3): 246–251.

50. **Passarini L.C., Nakajima P.R.** (2003), Development of a high-speed solenoid valve: an investigation of the importance of the armature mass on the dynamic response, *Journal of the Brazilian Society of Mechanical Sciences and Engineering*, XXV(4): 329–335.

51. **Passarini L.C., Pinotti JR, M.** (2003), A new model for fast-acting electromagnetic fuel injector analysis and design, *Journal of the Brazilian Society of Mechanical Sciences and Engineering*, 25(1): 95–106.

52. **Plavec E., Ladisic I., Vidovic M.** (2019), The impact of coil winding angle on the force of DC solenoid electromagnetic actuator, *Advances in Electrical & Electronic Engineering*, 17(3): 244–250.

53. **Pogulyaev Y.D., Baitimerov R., Rozhdestvensky Y.** (2015), Detailed dynamic modeling of common rail piezo injector, *Procedia Engineering*, 129: 93–98.

54. **Pulawski G., Szpica D.** (2015), The modelling of operation of the compression ignition engine powered with diesel fuel with LPG admixture, *Mechanika*, 21(6): 501–506.

55. **Rahman M. F., Cheung N. C., Lim K. W.** (1996a), Converting a switching solenoid to a proportional actuator, *IEEJ Transactions on Electrical and Electronic Engineering*, I-16(5): 531–537.

56. **Rahman M. F., Cheung N. C., Lim K. W.** (1996b), Modeling of a nonlinear solenoid toward the development of a proportional actuator, *Procceedings of the 5th International Conferences Modeling and Simulation of Electrical Machines Convertors and Systems ELECTRIMACS'96*, 2: 695–670.

57. **Raslavičius L., Keršys A., Makaras R.** (2017), Management of hybrid powertrain dynamics and energy consumption for 2WD, 4WD, and HMMWV vehicles, *Renewable and Sustainable Energy Reviews*, 68(1): 380–396.

58. **Raslavičius L., Keršys A., Mockus S., Keršiene N., Starevičius M.** (2014), Liquefied petroleum gas (LPG) as a medium-term option in the transition to sustainable fuels and transport, *Renewable & Sustainable Energy Reviews*, 32: 513–525.

59. **Ristovski Z.D., Jayaratne E.R., Morawska L., Ayoko G.A., Lim M.** (2005), Particle and carbon dioxide emissions from passenger vehicles operating on unleaded petrol and LPG fuel, *Science of the Total Environment*, 345: 93–98.

60. **Shamdani, A.H., Shamekhi, A.H., Basharhagh, M.Z.** (2006). Modeling and Simulation of a Diesel Engine Common Rail Injector in Matlab/Simulink, *14th Annual (International) Mechanical Engineering Conference*, 7.

61. **Simon M.** (2017), Pneumatic vehicle, research and design, *Procedia Engineering*, 181: 200–205.

62. **Szpica D.** (2016), Modeling of current limitation through the PWM signal in LPG injectors, *Proceedings of 20th International Scientific Conference Transport Means 2016*, 536–539.

63. **Szpica D.** (2016a), Testing the parameters of LPG injector solenoids as a function of the lift of the working component and the frequency of impulses, *Proceedings of 20th International Scientific Conference Transport Means 2016*, 551–555.

64. **Szpica D.** (2017), Comparative analysis of low pressure gas-phase injector's characteristics, *Flow Measurement and Instrumentation*, 58: 74–86.

65. **Szpica D.** (2018), Investigating fuel dosage non-repeatability of low pressure gas-phase injectors, *Flow Measurement and Instrumentation*, 59: 147–156.

66. **Szpica D.** (2018a), Research on the influence of LPG/CNG injector outlet nozzle diameter on uneven fuel dosage, *Transport*, 33(1): 186–196.

67. **Szpica D.** (2018b), Validation of indirect methods used in the operational assessment of LPG vapor phase pulse injectors, *Measurement*, 118: 253–261.

68. **Taghizadeh M, Ghaffari A, Najafi F.** (2009), Modeling and identification of a solenoid valve for PWM control applications, *Comptes Rendus Mecanique*, 337(3): 131–140.

69. **Tian H, Zhao Y.** (2018), Coil inductance model based solenoid on/off valve spool displacement sensing via laser calibration. *Sensors*, 18(12): 4492.

70. Valtek Type 30 – technical data. [online] [02.08.2018]. Available at: https://www.valtek.it.

71. **Waluś K.J., Warguła Ł., Krawiec P., Adamiec J.M..** (2018), Legal regulations of restrictions of air pollution made by non-road mobile machinery - the case study for Europe: a review, *Environmental Science and Pollution Research*, 25(4): 3243–3259.

72. **Warguła Ł., Krawiec P., Waluś K.J., Kukla M.** (2020), Fuel consumption test results for a self-adaptive, maintenance-free wood chipper drive control system, *Applied Sciences*, 10(8): 2727.

73. **Wendeker M., Jakliński P., Gabowski Ł., Pietrykowski K., Czarnigowski J., Hunicz J.** (2007), Model of CNG flap valve injector for internal combustion engines, *Combustion Engines*, 4(131): 42–52.

74. **Xiang Z., Liu H., Tao G-L, Man J., Zhong W.** (2008), Development of an ε-type actuator for enhancing high-speed electro-pneumatic ejector valve performance, *Journal of Zhejiang University - Science A*, 9(11): 1552–1559.

75. **Yang L.-J., Fu Q.-F., Qu Y.-Y., Zhang W., Du M.-L., Xu B.-R.** (2012), Spray characteristics of gelled propellants in swirl injectors, *Fuel*, 97: 253–261.

76. **Yang W.Y., Cao W., Chung T.S., Morris J.** (2005), *Applied Numerical Methods Using MATLAB*; John Wiley & Sons Inc., New Jersey.

ACCURACY ANALYSIS OF AIRCRAFT POSITION AT DEPARTURE PHASE USING DGPS METHOD

Kamil KRASUSKI*, Janusz ĆWIKLAK*

*Institute of Navigation, Military University of Aviation, Dywizjonu 303 35, 08-521 Dęblin, Poland

k.krasuski@law.mil.pl, j.cwiklak@law.mil.pl

Abstract: The aim of this paper is to present the problem of implementation of the Differential Global Positioning System (DGPS) technique in positioning of the aircraft in air navigation. The aircraft coordinates were obtained based on Global Positioning System (GPS) code observations for DGPS method. The DGPS differential corrections were transmitted from reference station REF1 to airborne receiver using Ultra High Frequency (UHF) radio modem. The airborne Thales Mobile Mapper receiver was mounted in the cabin in Cessna 172 aircraft. The research test was conducted around the military aerodrome EPDE in Dęblin in Poland. In paper, the accuracy of aircraft positioning using DGPS technique is better than 1.5 m in geocentric XYZ frame and ellipsoidal BLh frame, respectively. In addition, the obtained accuracy of aircraft positioning is in agreement with International Civil Aviation Organization (ICAO) Required Navigation Performance (RNP) technical standards for departure phase of aircraft. The presented research method can be utilised in Ground-Based Augmentation System (GBAS) in air transport. In paper, also the accuracy results of DGPS method from flight test in Chełm are presented. The mean values of accuracy amount to ±1÷2 m for horizontal plane and ±4÷5 m for vertical plane.

Key words: DGPS Method, Accuracy, GBAS, Reference Station, RTK

1. INTRODUCTION

The International Civil Aviation Organization (ICAO) facilitated the use of GNSS (Global Satellite Navigation System) satellite technique as a modern measurement technique for positioning the aircraft in aviation. At the same time, the GNSS satellite technique is treated as a non-conventional measurement method in relation to the classic system solutions used so far in aviation, e.g. the INS (Inertial Navigation System), DME (Distance Measuring Equipment), VOR (Very High Frequency Omnidirectional Radio Range) systems and others. Within the GNSS satellite technology, the ICAO permits the Global Positioning System **(**GPS) and GLONASS (Globalnaya Navigacionaya Sputnikovaya Sistema) navigational systems as well as ABAS (Aircraft-Based Augmentation System), SBAS (Satellite-Based Augmentation System) and Ground-Based Augmentation System (GBAS) augmentation systems to be used in aviation (ICAO, 2006). Among the above-mentioned GNSS satellite systems, the GBAS system requires a creation of appropriate technical infrastructure at an aerodrome and appears to be most time consuming and labour intensive. The GBAS system allows precise positioning of an aircraft by means of ground GNSS receivers installed in the vicinity of a given aerodrome. In particular, ground-based satellite receivers (GNSS reference stations) are installed along the approach path for a landing aircraft, so that the mobile receiver mounted on board an aircraft could receive differential correction data in real time. In the navigational aspect, the GBAS system has two fundamental variations exploited in aviation, i.e. the DGNSS (Differential Global Satellite Navigation System): DGPS (Differential Global Positioning System) or DGLONASS (Differential Globalnaya Navigacionaya Sputnikovaya Sistema) positioning technique and the RTK-OTF (Real Time Kinematic – On The Fly)

differential technique (Krasuski, 2017). In the DGNSS differential technique, there are the DGPS and DGLONASS positioning methods, on the basis of the ICAO certification for the application of navigation systems – GPS and GLONASS – in aviation. In the DGPS method of positioning, there are differential corrections of the GPS code measurements. On the other hand, the DGLONASS technique uses differential corrections of GLONASS code measurements. The DGPS and DGLONASS measurement techniques can be applied on the basis of ICAO standards, both in real time in order to determine an aircraft position as well as in the post-processing mode to reconstruct the trajectory of the aircraft flight. In addition, in the mathematical DGNSS method, the GNSS observations undergo the process of differentiation in order to eliminate the systematic errors. In case of the RTK-OTF differential technique, in precision aircraft positioning, precise single- or dual-frequency phase observations are used. Therefore, ground-based GNSS satellite receivers and a GNSS on-board receiver must record GPS/GLONASS observations at L1/L2 frequencies. For the DGNSS differential technique, it is possible to determine the aircraft positioning accuracy within several metres, typically less than 3 m (Kim et al., 2017). Due to the differential RTK-OTF technique, it is possible to recover the actual position of an aircraft with an accuracy of approximately 10 cm (Ciećko et al., 2016). In the GNSS satellite measurements in aviation, the RTK-OTF differential technique is used as a precision positioning method, being a reference for the DGNSS code measurements.

In the scientific literature, there are a lot of examples of using the DGNSS differential technique in scientific research concerning aircraft positioning in air navigation. The research concerning the determination of the positioning accuracy of an aircraft by means of the DGNSS differential technique in aviation was conducted in Poland and abroad. The research tests primarily focused on determining the aircraft accuracy of positioning on the basis of the

DGNSS solution. In the study of Krasuski et al. (2018a), the authors determined the accuracy of the DGLONASS positioning for the DGPS solution using dual-frequency GNSS code observations. In the numerical calculations, the recursive forward Kalman filtering was used. A typical accuracy of the DGLONASS positioning in relation to the DGPS solution equalled 10 m. In the study of Ciećko et al. (2014), the authors used the DGPS method in order to determine the accuracy of the aircraft positioning in real time. In the numerical calculations, differential corrections of data from the KODGIS (real time service of DGNSS corrections), being a part of the positioning system ASG-EUPOS (Aktywna Sieć Geodezyjna - European Position Determination System) in Poland, were used. A typical accuracy of the DGLONASS positioning in relation to the RTK-OTF base solution equalled 8 m. In the study of Grzegorzewski (2005), the authors used the DGPS method in order to determine the accuracy of the aircraft positioning in real time and in the post-processing mode. In the numerical calculations, the authors used GPS code observations at L1 frequency. A typical positioning DGPS accuracy in relation to the base RTK-OTF solution amounted up to 2 m in the post-processing mode and up to 18 m in real time. In the work of Grzegorzewski et al. (1999), an integration of the DGPS and DGLONASS methods was used in order to determine the aircraft positioning accuracy in real time. A typical accuracy of the DGPS/DGLONASS positioning in relation to the RTK-OTF base solution equalled 100 m. In the study of Tajima and Asakura (2005), the authors used the DGPS differential method in order to determine the accuracy of the aircraft positioning in real time. In the study, the research tests were conducted for the purposes of installing the GBAS system in air transport. A typical accuracy of the DGPS positioning in relation to the RTK-OTF base solution amounted to 10 m during all flight tests. In the study of Baroni and Kuga (2005), the DGPS differential technique was exploited in order to determine the aircraft positioning accuracy in the local coordinate frame ENU (Earth-North-Up). The mathematical model of designating the position of the aircraft was based on the use of Kalman filtering for the DGPS method. A typical DGPS positioning accuracy in relation to the solution of double-phase DD differences neared 10 m. In the study of Gianniou and Groten (1996), the DGPS differential technique was used to determine the aircraft positioning accuracy in the geocentric XYZ coordinate frame. In the calculations, determining the position of the aircraft at a different elevation angle of the GPS observation was tested. A typical DGPS positioning accuracy in relation to the DD double-phase differences equalled 8 m. In the study Eggleston (2002), the author used the DGPS differential technique in order to determine the accuracy of the aircraft altitude profile during the takeoff phase at the aerodrome. The readings of the aircraft position in the DGPS technique were compared with a laser measurement. The accuracy of calculating the elevation profile of the differential DGPS technique in relation to a laser measurement reached approximately 0.2 m. In the study of Sabatini and Palmerini (2008), the technique of the DGPS differential accuracy in determining the vertical profile of an aircraft was used. The readings of the aircraft position in the DGPS technique were compared with a radar measurement. The accuracy of the designation of the altitude profile of the DGPS differential technique with regard to a radar measurement reached 13 m.

In this article, the author focuses on the use of the DGNSS differential technique for the GPS code measurements (DGPS solution) in a flight test. In particular, the paper specifies the accuracy of aircraft positioning for the DGPS differential technique in the initial phase of the flight. The test flight was conducted by the Cessna 172 aircraft at the EPDE military aerodrome in Dęblin, the region of Lubelskie in Poland. The positioning accuracy of the aircraft Cessna 172 was determined for real-time applications within the DGPS differential technique. Thus, the paper presents a new solution of using the DGPS code measurements in aircraft positioning in the context of the scientific research with regard to implementation of the GBAS system in Polish aviation. The article has been divided into six parts: Introduction, Research Method, Research Test, Findings, Discussion and Conclusions. The article ends with a concise list of research literature.

2. THE RESEARCH METHOD

The mathematical model of the observation equation for the DGPS differential technique for code measurements at frequency L1 in the GPS navigation system, in real time, can be expressed as follows (Ali and Montenegro, 2014; Kim et al., 2017):

$$l = \rho + c \cdot d_{clk} + d_{atm} + PRC + RRC \cdot (t - t_0) \qquad (1)$$

where l is the code measurement (pseudorange) registered by the airborne receiver in the GPS system; ρ the geometric distance satellite and the airborne receiver in the GPS system, $\rho = \sqrt{(x - X_{GPS})^2 + (y - Y_{GPS})^2 + (z - Z_{GPS})^2}$; $(X_{GPS}, Y_{GPS}, Z_{GPS})$ are the satellites coordinates in the GPS system; (x, y, z) are the aircraft coordinates in the geocentric XYZ frame, unknown parameters in equation (1); c is the speed of light; d_{clk} the systematic error of the receiver clock delay in the GPS system; d_{atm} the systematic error of atmosphere delay in the GPS system; PRC the pseudorange correction in the DGPS differential technique; RRC the range rate correction in the DGPS differential technique; t the current measurement epoch and t_0 is the reference time.

The differential corrections PRC and RRC are determined on the basis of the mathematical models as shown below (Kaźmierczak et al., 2011):

$$\begin{cases} PRC = \rho_{ref} - d_{ref} \\ RRC = \frac{\Delta PRC}{\Delta t} \end{cases} \qquad (2)$$

where d_{ref} is pseudorange L1-C/A registered by the GPS reference station, ρ_{ref} the geometric distance between the satellite and the GPS reference station and Δt is the time interval.

In accordance with the technical recommendations of the ICAO for air operations, the airplane position should be determined using the method of least squares in the stochastic process. In case of the DGPS positioning technique, the aircraft coordinates are determined by means of differential corrections data for GPS code observations at L1 frequency. In the first place, the DGPS differential corrections are specified using GPS code observations at the GNSS reference station. The DGPS corrections are calculated on the assumption that precise GPS satellite coordinates and GNSS reference station coordinates are known while taking a measurement. In this way, the DGPS differential corrections are determined in accordance with equation (2). Thus, it is possible to formulate a mathematical equation (1), on the basis of which the aircraft coordinates in the geocentric frame XYZ are determined. The position of the aircraft is calculated in equation (1) in the GPS kinematic measurements in real time. Additionally, some of the systematic errors associated with the satellite clock error, such as satellite clock offset, hardware delay (TGD – Timing Group Delay) and relativistic correction, are eliminated from the observation equation (1) due to the use of the

difference operator. The remaining systematic errors in the observation equation (1) are divided into parameters which are connected with the receiver clock error d_{clk} and the atmospheric delay d_{atm}. The parameter d_{clk} in the DGPS differential technique is determined along with aircraft coordinates. In turn, the parameter of atmospheric delay d_{atm} is derived from deterministic models.

3. THE RESEARCH TEST AND RESULTS

Within the research test, the author determined the position of the aircraft during the execution of the flight experiment, namely the Cessna 172 had its coordinates designated during a flight test above the military aerodrome EPDE in Dęblin in the region of Lubelskie in Poland (see Fig. 1). Due to the computed coordinates of the Cessna 172, it was possible to evaluate the use of DGPS precision measurement technique in aviation. In particular, the research focused on the determination of the coordinates of the aircraft Cessna 172 in the initial phase of the flight. The aspect of the initial phase of the flight, i.e. take-off and departure, is extremely important to pilots. Besides, the aircraft take-off is one of the most demanding components of pilotage, constituting one of the most important elements of the pilot's work in the cockpit.

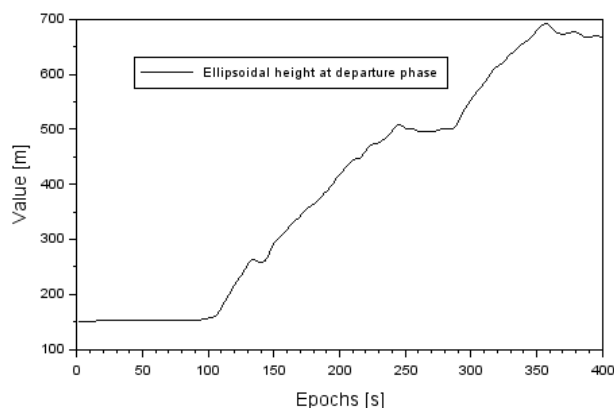**Fig. 1.** The horizontal trajecory of the aircraft (https://www.google.pl/maps/)

Fig. 2. The vertical trajectory of the aircraft

A portable navigation receiver Thales Mobile Mapper with the function of receiving differential corrections and the work of the DGPS computational module, was installed into airplane Cessna 172. In addition, there was a dual-frequency geodetic receiver Topcon HiperPro, serving as a reference GNSS station (REF1) for the military aerodrome EPDE in Dęblin (see Fig. 1). The DGPS differential corrections were sent from the reference REF1 station to the receiver Thales Mobile Mapper using the Ultra High Frequency (UHF) transmission link (Tsai, 1999). The DGPS differential corrections were sent to the receiver Thales Mobile Mapper in the standard RTCM (Radio Technical Commission for Maritime) format.

The investigations were conducted for the initial phase of the Cessna 172 flight, i.e. take-off and departure from the military aerodrome in Dęblin. The maximum distance of the Cessna 172 from the reference station REF1 was below 10 km. At this time, the aircraft Cessna 172 climbed from approximately 150 m to almost 700 m and levelled off (see Fig. 2). The time of making this operation was close to 400 s, or more than 6.6 minutes. At that time, the aircraft turned right and flew in the direction of the town of Kozienice in Mazowieckie voivodeship in Poland. The target distance to fly over the city of Kozienice against the aerodrome EPDE location in Dęblin was approximately 25–30 km.

Prior to the flight, the test receiver Thales Mobile Mapper was configured and set as below (Hejmanowska et al., 2005):

− internal software of the receiver: Mobile Mapper Field and Mobile Mapper Office;
− export format data: SHP, MIF and DXF;
− the possibility to use base maps: yes; reference frame: global, WGS-84 as a standard;
− mode of computations: DGPS differential;
− final format of coordinates: geocentric XYZ coordinates ellipsoidal BLh frame;
− the maximum number of tracked GPS satellites: 12 GPS satellites;
− manner of tracking GPS satellites: sequential;
− initialisation of calculations: "cold start" <2 minutes, "warm start" <1 minute, "hot start" <15 seconds;
− interval of calculations and recording time of the observation: 1 second as a rule;

− protocol of satellite data transmission: standard RTCM -104;
− receiving antenna: built in the receiver;
− battery life: typically up to 8 hours;
− number of batteries in a set: usually two batteries built into the receiver;
− mode of positioning: real time;
− GPS ephemeris data: on-board broadcast ephemeris;
− weighting of measurement results: applied;
− elevation mask: 5°;
− reference time: GPS time.

Fig. 3 shows the number of GPS satellites being tracked by the Thales Mobile Mapper airborne receiver and reference stations REF1. During the air experiment, the number of GPS satellites ranged from eight to nine; however, eight GPS satellites being tracked were only in 6 measurement epochs, whereas in the remainder of 394 epochs, the number of GPS satellites equalled nine. It needs to be emphasised that during the research test, the number of satellites exceeded four; thus, it was possible to determine the navigational position of the aircraft from equation (1). It can be added, therefore, that during the take-off and climb of the Cessna 172, for approximately 98% of the flight time, the number of GPS satellites equalled 9. Moreover, it can be observed that the number of available GPS satellites translated directly into determining the coordinate values of the aircraft Cessna 172 during the flight.
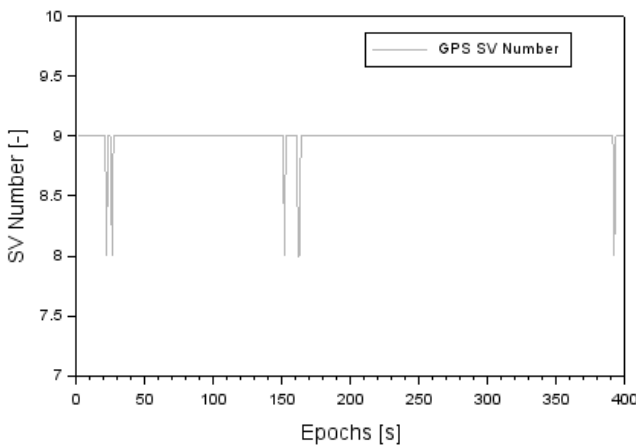

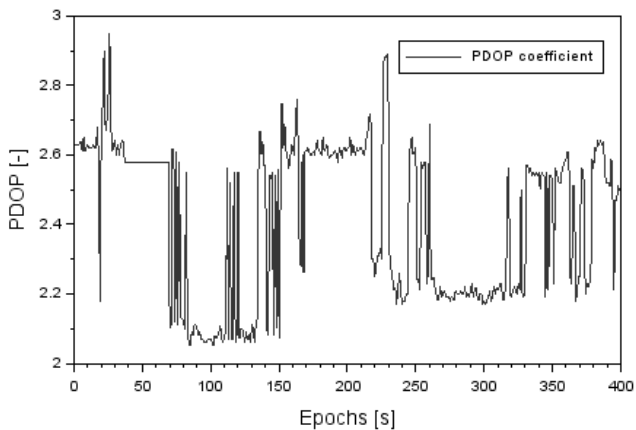**Fig. 3.** The number of GPS satellites at the flight test

Fig. 4. The value of PDOP (Position Dilution of Precision) coefficients at the flight test

Fig. 4 shows the value of the dilution of precision coefficient PDOP position during the initial phase of the flight. The minimum value of the PDOP coefficient equals 2.1, whereas the maximum value is equal to 2.9. In addition, the median for the PDOP value parameter is equal to 2.5. The average value of the PDOP coefficient equals approximately 2.4 with a mean error of 0.2. It should be noted that at the time of the take-off from the EPDE aerodrome in Dęblin, the value of the PDOP coefficient was below 3. It can, therefore, be concluded that the conditions for making observations to conduct GPS satellite measurements at the time of the air experiment were very good. It was possible to obtain low values of the PDOP coefficient for a high number of tracked GPS satellites during the flight test (see Fig. 3).

In the framework of the conducted air experiment, the key element of the studies was to assess the positioning accuracy of the aircraft Cessna 172 using the DGPS measurement technique. For this reason, the author compared the values of the designated Cessna 172 coordinates from the DGPS solution in relation to the precise position of the aircraft designated by means of the RTK-OTF differential technique. The precise trajectory of the Cessna 172 was recovered by means of the RTK-OTF differential technique for the GPS dual-frequency phase observations. In the RTK-OTF differential technique, the authors used GPS phase observations from the reference station REF1 and additionally from the geodetic receiver Topcon HiperPro, mounted on board the Cessna 172. The Topcon HiperPro receiver was located at a distance of less than 0.1 m against the navigation receiver Thales Mobile Mapper. The computations of the Cessna 172 aircraft base position for the RTK-OTF differential technique were performed in the AOSS v.2.0 programme (Krasuski et al., 2018b). Therefore, it was possible to compare the designated coordinates of the Cessna 172 from the DGPS solution with the reference position from the RTK-OTF solution. Comparison of the Cessna 172 position was done in the frame of geocentric XYZ coordinates and ellipsoidal BLh coordinates in the framework of implementation of the reference frame ETRF'89.

Therefore, in the first place, a comparison was made between the designated coordinates of the Cessna 172 from the navigational receiver Thales Mobile Mapper and the base RTK-OTF solution. On this basis, it was possible to determine the difference in the coordinate values of the aircraft Cessna in the geodetic XYZ frame for the code DGPS method as below (Gianniou and Groten 1996):

$$\begin{cases} DX = x_{DGPS} - x_{RTK} \\ DY = y_{DGPS} - y_{RTK} \\ DZ = z_{DGPS} - z_{RTK} \end{cases} \qquad (3)$$

where x_{DGPS} is the designated aircraft coordinate along the X axis, on the basis of the DGPS solution, in accordance with equation (1); y_{DGPS} the designated aircraft coordinate along the Y axis, on the basis of the DGPS solution, in accordance with equation (1); z_{DGPS} the designated aircraft coordinate along the Z axis, on the basis of the DGPS solution, in accordance with equation (1); x_{RTK} the reference coordinate of the aircraft along the X axis on the basis of the RTK-OTF differential technique; y_{RTK} the reference coordinate of the aircraft along the Y axis on the basis of the RTK-OTF differential technique and z_{RTK} is the reference coordinate of the aircraft along the Z axis on the basis of the RTK-OTF differential technique.

Fig. 5 shows the results of a comparison of XYZ coordinates of the aircraft Cessna 172 on the basis of the DGPS code solution and the RTK-OTF phase solution. The positioning accuracy of the

aircraft Cessna 172 along the X axis ranges from −0.25 to +0.18 m. In addition, the average value of DX parameter equals −0.02 m, with the RMS (Root Mean Square) error being approximately 0.08 m. The mean value of positioning of the Cessna 172 along the Y axis is equal to +0.09 m and the RMS error is 0.07 m. Moreover, the amplitude of the obtained findings for the difference in the coordinate along the Y axis ranges from −0.08 to +0.21 m. The mean value of positioning accuracy of the aircraft Cessna 172 along the axis Z is equal to −0.34 m, whereas the RMS error is equal to 0.35 m. Besides, the amplitude of the obtained results for the difference in the coordinate along the Z axis is between −1.16 and +0.28 m. It is worth adding that the maximum value of the parameters (DX, DY) reaches the range of ±0.25 m. At the same time, the RMS error for the parameter values (DX, DY) reaches the maximum results to the level of 0.1 m. The dispersion of results for the parameter DZ, compared to the results of the accuracy along the X axis and Z axis, is quite significant, exceeding the level of ±1 m. Nevertheless, the RMS error along the Z axis is under 0.4 m.
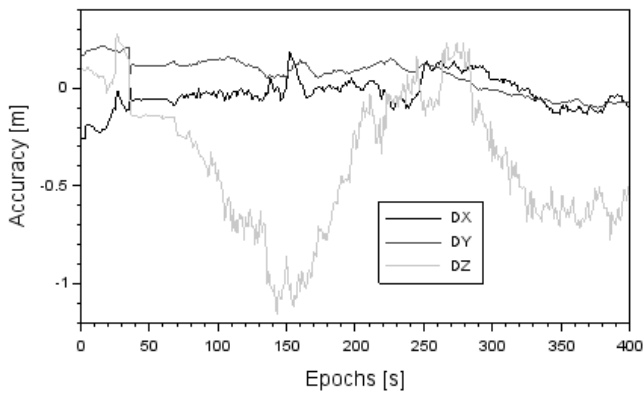

Fig. 5. The accuracy of aircraft positioning in the geocentric XYZ coordinates
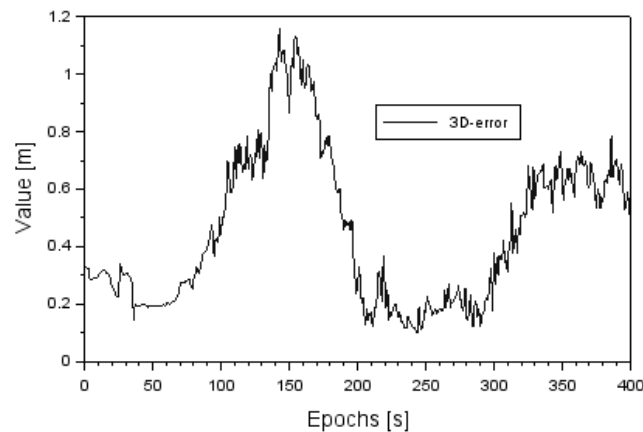

Fig. 6. The results of 3D-error in the geocentric XYZ coordinates

In the next stage, Fig. 6 shows the resultant shift error (3D-error) of geocentric XYZ coordinates of the Cessna 172 from the DGPS solution with regard to the reference coordinates of the RTK-OTF differential technique. The 3D-error parameter was determined from the dependence as below (Rodríguez-Bilbao et al., 2015):

$$3D-\text{error} = \sqrt{DX^2 + DY^2 + DZ^2} \qquad (4)$$

The mean value of the 3D-error parameter equalled 0.45 m for the range between 0.10 and 1.17 m. It is worth stressing that the value of the 3D-error exceeds 1 m for 23 measurement epochs. To conclude, in approximately 95% of the measurement epochs, the value of the 3D-error does not exceed the level of 1 m.
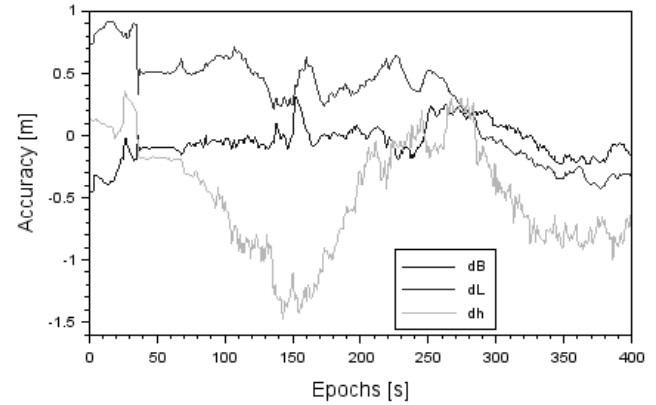

Fig. 7. The accuracy of aircraft positioning in the ellipsoidal BLh coordinates

In the next stage, the positioning accuracy of the aircraft Cessna 172 from the DGPS solution in the ellipsoidal BLh frame was determined. In order to determine the position of the aircraft Cessna 172 in the ellipsoidal frame, the Helmert transformation from the geocentric XYZ coordinates to the ellipsoidal BLh coordinates was used. The positioning accuracy values of the aircraft Cessna 172 in the ellipsoidal BLh frame were defined as below (Grzegorzewski et al., 2008):

$$\begin{cases} dB = B_{DGPS} - B_{RTK} \\ dL = L_{DGPS} - L_{RTK} \\ dh = h_{DGPS} - h_{RTK} \end{cases} \qquad (5)$$

where B_{DGPS} is the designated coordinate of the aircraft for B geodetic latitude on the basis of the DGPS solution, L_{DGPS} the designated coordinate of the aircraft for L geodetic longitude on the basis of the DGPS solution, h_{DGPS} the designated coordinate of the aircraft for h ellipsoidal height on the basis of the DGPS solution, B_{RTK} the reference coordinate of the aircraft for B geodetic latitude on the basis of the RTK-OTF differential technique, L_{RTK} the reference coordinate of the aircraft for L geodetic latitude on the basis of the RTK-OTF differential technique and h_{RTK} is the reference coordinate of the aircraft for h ellipsoidal height on the basis of the RTK-OTF differential technique.

The results of the positioning accuracy of the aircraft Cessna 172 from the DGPS solution in the ellipsoidal BLh frame is shown in Fig. 7. The positioning accuracy of the aircraft Cessna 172 along the axis B ranges from −0.45 to +0.32 m. In addition, the mean value of dB parameter equals −0.05 m, with the RMS error being approximately 0.14 m. The mean value of the positioning accuracy of the Cessna 172 along the axis L is equal to +0.29 m and the RMS error is 0.37 m. Furthermore, the amplitude of the results obtained for the difference in the coordinate along the axis L ranges from −0.43 to +0.92 m. The mean value of the positioning accuracy of the aircraft Cessna 172 along the axis h is equal to −0.48 m, whereas the RMS error is equal to 0.44 m. Besides, the amplitude of the obtained results for the difference along the axis h ranges from −1.48 to +0.36 m. The smallest positioning accuracy of the aircraft Cessna 172 is noticeable along the axis h

and the highest accuracy is found for the coordinate B. In addition, the RMS error is the biggest for the coordinate h and the smallest for the coordinate B.

4. DISCUSSION

The findings obtained in the study, with regard to the positioning accuracy of Cessna 172 in the initial phase of the flight, proved the usefulness of using the DGPS differential technique in aviation. In particular, the high accuracy of positioning using the DGPS differential technique in relation to the real position of the aircraft Cessna 172 is extremely important in the context of the development of infrastructure of the GBAS system in aviation. The values of the positioning accuracy of the Cessna 172, found using the DGPS differential technique, did not exceed the level of ±1.5 m. The results of the positioning accuracy of the Cessna 172 are very interesting in terms of comparison of the scientific research findings with other studies (Baroni and Kuga, 2005; Ciećko et al., 2014; Gianniou and Groten, 1996; Grzegorzewski et al., 1999; Grzegorzewski, 2005; Krasusky et al., 2018; Tajima and Asakura, 2002). It should be observed that the obtained positioning accuracy of the Cessna 172 aircraft is much higher than the results published in other studies (Baroni and Kuga, 2005; Ciećko et al., 2014; Gianniou and Groten, 1996; Grzegorzewski et al., 1999; Grzegorzewski, 2005; Krasuski et al., 2018a; Tajima and Asakura, 2002). Therefore, the use of DGPS differential measurements in aviation is justifiable and efficient. However, the problem of the DGPS differential technique is the construction and maintenance of expensive technical infrastructure at an aerodrome in the form of GNSS reference stations, enabling transmission of differential corrections. Such a GNSS reference station must be equipped with a dual-frequency receiver, resistant to the effect of multipath and allowing tracking of GPS, GLONASS, BeiDou and Galileo satellite constellations. The need to build technical infrastructure for a GNSS reference station leads to additional expenses for the Airport Area Manager. On the other hand, however, the construction of a GNSS reference station at an aerodrome will ensure creation of the GBAS augmentation system, which will significantly increase the precision and accuracy of performed air operations. The basic navigation features for the operation of the GBAS system at the airport should allow distribution of the DGPS differential corrections, provision of data associated with the GBAS, provision of data with regard to the final approach in case of precision approaches and provision of data on the precise distance of an aircraft to a runway. It should also provide monitoring of credibility and integrity for the determination of the distance parameter of the aircraft to the airport and improve the aircraft position and reference time.

Lastly, the problem of accuracy of an aircraft operation, in the context of ICAO provisions and recommendations, is worth discussing. In accordance with the provisions of ICAO Required Navigation Performance (RNP), the accuracy of positioning for the conduct of navigation in the horizontal plane LNAV in a departure phase from the airport must not exceed 220 m. On the other hand, for the conduct of navigation in the vertical plane VNAV, the ICAO has not introduced any technical recommendations or indications for the use of the GNSS sensor in aircraft positioning (ICAO, 2006). Thus, the accuracy results with regard to the Cessna 172 positioning, using the DGPS method, can be compared only for horizontal coordinates. The technical recommendations of the ICAO Annex 10 to the Chicago Convention refer to aircraft posi-

tioning accuracy with the use of the GNSS sensor, expressed in ellipsoidal BLh coordinates. The resulting positioning accuracy of the horizontal coordinates (B and L) for the Cessna 172 does not exceed 1 m. Thus, the technical standards and recommendations made by the ICAO for aircraft positioning accuracy in the phase of a departure from an aerodrome were satisfied. However, it is essential to conduct further testing using the DGPS technique in order to evaluate the aircraft positioning accuracy, also in the phase of a flight and a landing approach.

Further, the accuracy parameters of DGPS method were verified and calculated for GPS data in a flight experiment in Chełm in southeastern Poland. Fig. 8 presents the accuracy of aircraft position in BLh ellipsoidal coordinates. The typical accuracy of latitude ranges between −2.92 and −0.46 m. In addition, the arithmetic mean of latitude accuracy is about −1.95 m. The typical accuracy of longitude ranges between −0.85 and −0.28 m. In addition, the arithmetic mean of longitude accuracy is about −0.61 m. The typical accuracy of ellipsoidal height ranges between +1.57 and +8.42 m. In addition, the arithmetic mean of ellipsoidal height accuracy is about +4.65 m.
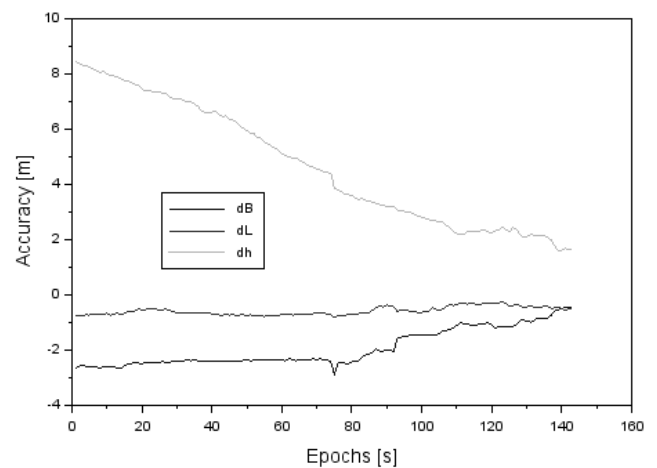

Fig. 8. The accuracy of aircraft positioning in the ellipsoidal BLh coordinates in Chełm experiment
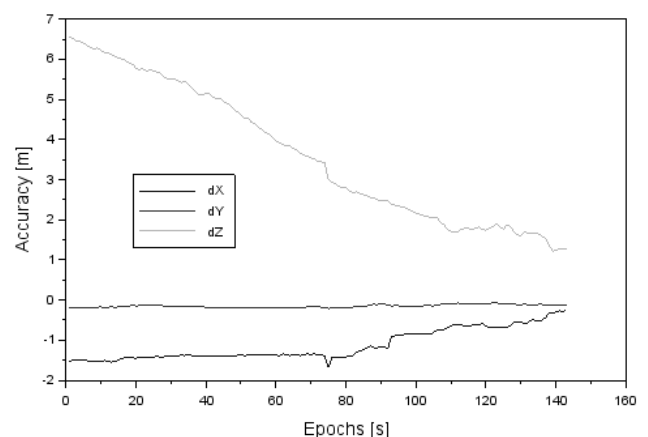

Fig. 9. The accuracy of aircraft positioning in the geocentric XYZ coordinates in Chełm experiment

Fig. 9 presents the accuracy of aircraft position in XYZ coordinates. The typical accuracy along X axis ranges between −1.68 and −0.26 m. In addition, the arithmetic mean of X coordinate

accuracy is about −1.13 m. The typical accuracy along the Y axis ranges between −0.21 and −0.08 m. In addition, the arithmetic mean of Y coordinate accuracy is about −0.15 m. The typical accuracy along the Z axis ranges between +1.22 and +6.55 m. In addition, the arithmetic mean of Z coordinate accuracy is about +3.62 m.
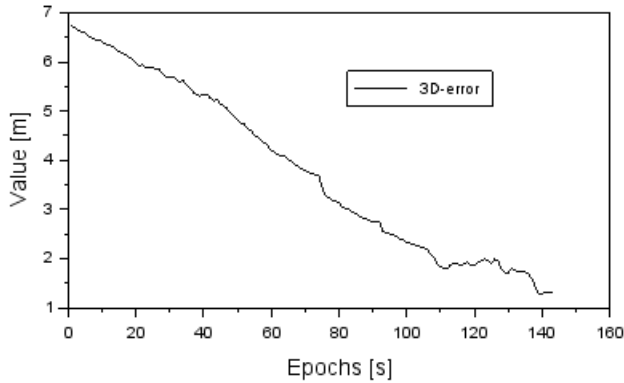
Fig. 10. The results of 3D-error in the geocentric XYZ coordinates in Chełm experiment
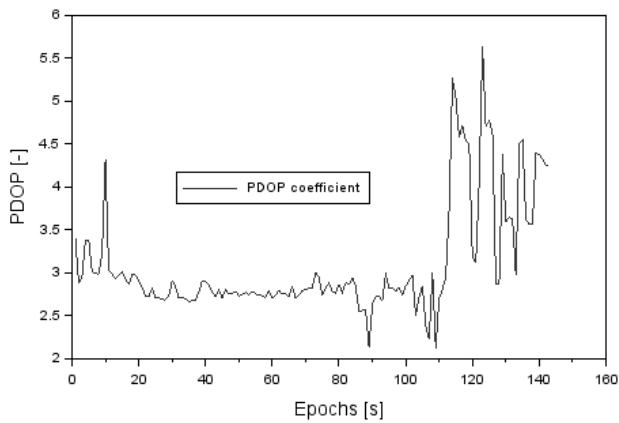
Fig. 11. The value of PDOP coefficients at the flight test in Chełm experiment
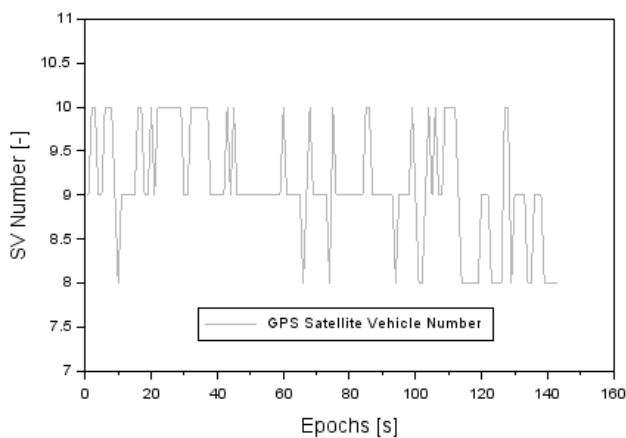
Fig. 12. The number of GPS satellites at the flight test

Fig. 10 shows the results of 3D-error for the accuracy of XYZ coordinates. The mean value of the 3D-error parameter equalled 3.80 m for the range between 1.26 m and 6.73 m obtained in the results. The highest results of 3D-error are obtained at the first phase of flight and it decreases with the observation time.

Fig. 11 shows the value of the dilution of precision coefficient PDOP position during the initial phase of the flight in Chełm experiment. The minimum value of the PDOP coefficient equals 2.1, whereas the maximum value is equal to 5.6. In addition, the median for the PDOP value parameter is equal to 2.8. The average value of the PDOP coefficient equals approximately 3.1. It should be noted that at the time of the take-off from the EPCD aerodrome in Chełm, the value of the PDOP coefficient was below 6.

Fig. 12 shows the number of GPS satellites being tracked by the airborne receiver and GNSS reference station in Chełm experiment. During the air experiment, the number of GPS satellites ranged from 8 to 10; however, the average value of the number of GPS satellites being tracked equalled 9 in the flight test in Chełm.

5. CONCLUSIONS

The paper publishes the results of scientific research concerning the use of the DGPS differential technique in positioning the aircraft in air navigation. In particular, the paper presents the results of the positioning accuracy of the aircraft using the DGPS techniques during the phase of a departure from the airport. In the air experiment, the author used the Cessna 172 aircraft, which performed a test flight over the military aerodrome EPDE in Dęblin. On board the aircraft, the navigation receiver Thales Mobile Mapper was mounted, which determined the aircraft position in a differential mode DGPS. Besides, at the airport in Dęblin, a geodetic receiver Topcon HiperPro was mounted. Its aim was to transmit differential corrections through the UHF Link to the on-board receiver Thales Mobile Mapper. The test flight was conducted for the first 400 seconds of the flight of the Cessna 172 from the military aerodrome EPDE in Dęblin. During the test flight, the Cessna 172 changed its altitude from approximately 150 m to nearly 700 m. In addition, during the flight test, the number of GPS satellites used in the solution of the aircraft position in the DGPS technique ranged from eight to nine. Additionally, the PDOP coefficient during the tests was less than 3. In order to determine the positioning accuracy of the Cessna 172, the authors verified the designated coordinates from the DGPS solution in relation to a precise flight trajectory obtained from the RTK-OTF differential technique. The positioning accuracy of the aircraft Cessna 172 in the geocentric XYZ coordinates was higher than 1.2 m, whereas in the ellipsoidal BLh coordinates, it exceeded 1.5 m. The findings on Cessna 172 positioning accuracy emphasise the fact that the DGPS technique can be used in the GBAS system in aviation. Furthermore, the obtained results of aircraft positioning accuracy of the Cessna 172 by means of the DGPS technique comply with the ICAO recommendations and instructions within executed departures from an aerodrome. The accuracy results of DGPS method from a flight test in Chełm are also presented in the paper. The mean values of accuracy amounts to ±1÷2 m for horizontal plane and ±4÷5 m for vertical plane. In addition, the PDOP coefficient amounts between 2.1 and 5.6. Moreover, the number of GPS satellites used in the solution of the aircraft position in the DGPS technique ranged from 8 to 10. Accuracy results from the flight test in Dęblin and Chełm are suitable for DGPS solution in air navigation.

In the future, the authors plan to perform tests for other phases of flight, e.g. landing.

REFERENCES

1. **Ali, Q., Montenegro, S.** (2014), A Matlab Implementation of Differential GPS for Low-cost GPS Receivers, *TransNav*, 8(3), 343-350.

2. **Baroni, L., Kuga H. K.** (2005), Analysis of navigational algorithms for a real time differential GPS system, *18th International Congress of Mechanical Engineering*, November 6-11, 2005, Ouro Preto, Brazil.

3. **Ciećko, A., Grunwald, G., Kaźmierczak, R., Grzegorzewski, M., Ćwiklak, J., Oszczak, S., Bakuła M.** (2014), Analysis of the accuracy and availability of ASG-EUPOS services in air navigation and transport, *Logistyka*, 3, 1091-1100. (in Polish)

4. **Ciećko, A., Grzegorzewski, M., Oszczak, S., Ćwiklak, J., Grunwald, G., Balint, J., Szabo, S.** (2016), Examination of EGNOS Safety-Of-Life service in Eastern Slovakia, *Annual of Navigation*, 22/2015, 65-67.

5. **Eggleston, B., McKinney, W. D., Choi, N. S., Min D.** (2002), A low cost flight test instrumentation package for flight airplanes, *23rd Congress of International Council of the Aeronautical Sciences*, 8-13 September, 2002, Toronto, Canada, Paper ICAS 2002-5.2.2.

6. **Gianniou, M., Groten E.** (1996), An advanced real-time algorithm for code and phase DGPS, *Paper presented at DSNS'96 Conference*, St. Petersburg, Russia, May 20-24.

7. **Grzegorzewski, M.** (2005), Navigating an aircraft by means of a position potential in three dimensional space, *Annual of Navigation*, 9, 26-27.

8. **Grzegorzewski, M., Ciećko, A., Oszczak, S., Popielarczyk, D.** (2008), Autonomous and EGNOS Positioning Accuracy Determination of Cessna Aircraft on the Edge of EGNOS Coverage, *Proceedings of the 2008 National Technical Meeting of The Institute of Navigation*, San Diego, CA, January 2008, 407-410.

9. **Grzegorzewski, M., Jaruszewski, W., Fellner, A., Oszczak, S., Wasilewski, A., Rzepecka, Z., Kapcia, J., Popławski T.** (1999), Preliminary results of DGPS/DGLONASS aircraft positioning in flight approaches and landings, *Annual of Navigation*, 1, 41-53.

10. **Hejmanowska, B., Rodolphe, P., Oszczak, S., Ciećko A.** (2005), *Validation of methods for measurement of land parcel areas*, Draft final report, AGH University of Science and Technology.

11. **ICAO** (2006), "ICAO standards and recommended practices (SARPS), annex 10 volume I (radio navigation aids)", available at: www.ulc.gov.pl/pl/prawo/prawo-mi%C4%99dzynarodowe/206-konwencje, current version on date: 15 October 2018, (in Polish).

12. **Kaźmierczak, R., Grunwald, G., Bakuła, M**. (2011), The use of RTCM 2.X Dekoder Software for Analyses of KODGIS and NAWGIS Services of the ASG-EUPOS System, *Technical Sciences*, 14(2), 229-243.

13. **Kim, J., Song, J., No, H., Han, D., Kim, D., Park, B., Kee, C.** (2017), Accuracy Improvement of DGPS for Low-Cost Single-Frequency Receiver Using Modified Flächen Korrektur parameter Correction, *ISPRS Int. J. Geo-Inf.*, 6, 222.

14. **Krasuski, K.** (2017), Application the GPS code observations in BSSD method for recovery the position of the aircraft, *Journal of Automation, Mobile Robotics & Inteligent Systems*, 11(3), 45-52.

15. **Krasuski, K., Ćwiklak, J., Grzesik, N.** (2018), Accuracy assessment of aircraft positioning by using the DGLONASS method in GBAS system, *Journal of KONBIN*, 45, 97-124.

16. **Krasuski, K., Wierzbicki, D., Jafernik H.** (2018), Utilization PPP method in aircraft positioning in post-processing mode, *Aircraft Engineering and Aerospace Technology*, 90(1), 202-209.

17. **Rodríguez-Bilbao, I., Radicella, S. M., Rodríguez-Caderot, G., Herraiz M.** (2015), Precise point positioning performance in the presence of the 28 October 2003 sudden increase in total electron content, *Space Weather*, 13, 698–708.

18. **Sabatini, R., Palmerini, G. B.** (2008), *Differential Global Positioning System (DGPS) for Flight Testing*, ISBN 978-92-837-0041-8, RTO AGARDograph 160 Flight Test Instrumentation Series – Volume 21, Chapter 6 – DGPS PERFORMANCE ANALYSIS.

19. **Tajima, H., Asakura, M.** (2002), Flight Experiments of DGPS Approaches and Landings on a Megafloat Airport Model, *Transactions Of The Japan Society For Aeronautical And Space Sciences*, 45 (147), 66-68.

20. **Tsai, Y-J.** (1999), *Wide Area Differential operation of the Global Positioning System: ephemeris and clock algorithms*, PhD thesis, Stanford University, 110-112.

21. **URL1.** (2019), https://www.google.pl/maps/, current on 2019.

PURE BENDING OF STRIP (BEAM) WITH CRACK IN STRIP OF TENSILE STRESS WITH ALLOWANCE FOR PLASTIC STRIPS NEAR CRACK TIPS

Heorgij SULYM[*], Viktor OPANASOVYCH[**], Mykola SLOBODIAN[**], Oksana BILASH[***]

[*]Department of Mechanics and Applied Computer Science Application, Faculty of Mechanical Engineering,
Bialystok University of Technology, ul. Wiejska 45 C, 15-351 Bialystok, Poland
[**]Faculty of Mechanics and Mathematics, Department of Mechanics,
Ivan Franko National University of Lviv, Universytetska Street, 1, Lviv, 79000, Ukraine
[***]Faculty Training Specialists Battle (Operational) Software, Department of Engineering Mechanics,
Hetman Petro Sahaidachnyi National Army Academy, Heroes of Maidan Street, 32, Lviv, Ukraine

sulym@pb.edu.pl, Viktor.Opanasovych@lnu.edu.ua, slobkolia@gmail.com, oksana.opanasovych@gmail.com

Abstract: In the article, the pure bending problem for strip (beam) with straight, perpendicular to its axis crack located in the zone of tensile stresses is investigated on the assumption of narrow plastic strips near crack tips. Using methods of the theory of functions of a complex variable and complex potentials, the problem is reduced to the several linear conjunction problems. The solutions of latter problems are obtained in the class of functions confined in the edges of plastic strips. Formulas for the calculation of their lengths are derived. Expressions for the determination of crack tip opening values are written. Numerical analysis of the problem is performed.

Key words: Pure Bending, Strip (Beam), Crack, Plastic Strips, Linear Conjugation Problems

1. INTRODUCTION

Beams are one of the main structural elements that are common in engineering, especially in construction practice. Cracks, which are strong stress concentrators, may appear in them during various operations and, as a result, may lead to destruction of such structural elements. Therefore, it is very important to carefully evaluate the reliability of the beam operation in the presence of such defects.

In an article, Monfared et al. (2018) investigated the configuration of arbitrary crack configurations in the orthotropic strip. Fourier transformation was used to construct a system of singular integral equations that was numerically solved using the Chebyshev quadrature formula for the density of dislocation on a crack face. Effects of crack geometry and parameter of nonhomogeneity of material on the stress intensity, energy release and energy density were considered. In the work of Pavazza (2000), approximate analytical formulas for stresses and displacements in thin rectangular orthotropic or isotropic strips subjected to tension are presented.

Shi (2015) devoted his investigation to analytical and numerical analyses of the doubly periodic arrays of cracks and proposes a precise solution procedure for describing the interaction effect in the doubly periodic rectangular-shaped arrays of cracks. Fan et al. (2014) investigated the elastic-plastic fracture behaviour of an interaction between Zener–Stroh crack and coated inclusion in composite materials with regard to crack tip plastic zones. The sizes of plastic zone at the both crack tips were determined by the generalised Irwin model. In the article by Prawoto (2012), an approach of classical fracture mechanics is used for calculating the near crack tip plastic zones in heterogeneous or composite materials. In the research by Unger (2007), the Dugdale model of plasticity is used for a static crack instead of Tresca plasticity theory.

An analysis of stress–strain state under combined bending and tension of an isotropic plate with crack is represented by Sulym et al. (2018) in the assumption of line and constant width area contact between crack faces but with no plastic zones near the crack tips. In the articles by Nykolyshyn et al. (2010, 2015), the tension of homogeneous isotropic plate weakened by two through cracks with plastic zones is considered. By using the method of complex potentials, the solution of the problem is reduced to linear conjugation problems and the explicit expressions for complex potentials of plane problem. The length of the plastic zone and crack opening displacement are obtained analytically and the numerical analysis of them is performed at various parameters. In the particular case, the known results are obtained.

Kuz et al. (2015, 2019) investigated the influence of stress concentrators (square hole, cut or rigid inclusion) on the strength of a plate under uniaxial tension using the numerical solution of boundary-value problems of the theory of small elasto-plastic deformations for a linear hardening material. The growth of microstructurally short and physically small cracks in the fatigue process zone and the initiation of macrocrack in notched tension specimens were investigated in the work of Ostash (2017).

In this article, the problem of pure bending of strip (beam) with crack perpendicular to its axis and located in tensile stresses area is investigated. We assumed that at the crack tips, the narrow plastic strips are formed, as in the works of Panasyuk (1968) and

Savruk et al. (1989). Solving of the problem is based on the methods of the theory of functions of complex variable and complex potentials and is reduced to the problems of linear conjunction. Their solutions are obtained in class of functions confined at the tips of plastic strips. The method used in the article is given in the work of Muskhelishvili (1966). System of transcendental equations for calculating lengths of plastic zones is written. Expressions for calculating of crack tip opening values are also obtained. The numerical analysis of the problem is carried out. Graphic dependencies of the length of plastic strips and crack tip opening values are constructed at various values of problem parameters.

2. FORMULATION OF THE PROBLEM

Consider an elastic isotropic strip (beam) perpendicular to its axis straight through crack of length 2l, centre of which is at the distance x_0 from the axis. Let 2h be the height of the beam transverse section and $2\tilde{a}$ be the width of the beam. Assume that the beam is under pure bending with the bending moment M. Let us introduce a Cartesian coordinate system Oy-axis, which is directed along the beam centre line, and Ox-axis, which is directed along the crack. The crack is located in the tensile stress zone and its faces are free of external loads. Assume that near crack tips with coordinates $(a, 0)$ and $(b, 0)$ narrow plastic zones (plastic srips) have been formed on the extending of the crack. In these zones, normal stresses are equal to the yield strength of beam material (Panasyuk, 1968; Savyn, 1968). Let the coordinates of edges of the plastic strips are (d_2, a) and (b, d_1), L denotes the projection of the crack onto the Ox-axis and L_1 and L_2 denote plastic strips of length $\Delta_2 = a - d_2$ and $\Delta_1 = d_1 - b$, respectively (Fig. 1). In addition, we introduce the notations $\tilde{L} = L + L_1 + L_2$ and $\tilde{L}_1 = L_1 + L_2$.
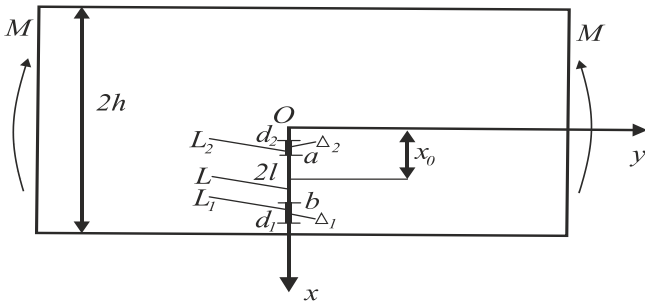

Fig. 1. Beam loading scheme and location of crack with plastic strips

The following boundary conditions correspond to the formulated problem:

$$\sigma_{xy}^{\pm} = 0, x \in \tilde{L};$$
$$\sigma_{yy}^{\pm} = 0, x \in L; \sigma_{yy}^{\pm} = \sigma_Y, x \in \tilde{L}_1, \tag{1}$$

where σ_{yy} and σ_{xy} are the components of stress tensor and marks '+' and '−' mean limits as $y \to \pm 0$.

3. CONSTRUCTION OF THE SOLUTION OF THE PROBLEM

Let us introduce the complex potentials $\Phi(z)$ and $\Omega(z)$ (Muskhelishvili, 1966) and use the expressions

$$\sigma_{yy} - i\sigma_{xy} = \Phi(z) + \Omega(\bar{z}) + (z - \bar{z})\overline{\Phi'(z)}, \tag{2}$$

$$2\mu(u + iv)' = \kappa\Phi(z) - \Omega(\bar{z}) - (z - \bar{z})\overline{\Phi'(z)}, \tag{3}$$

where μ is the shearing modulus; κ is the Muskhelishvili's constant; $u' = \partial u/\partial \mathrm{x}$, $v' = \partial v/\partial \mathrm{x}$; u and v are the components of displacement vector of a beam point on axes Ox and Oy; $z = x + iy, i^2 = -1$.

According to Panasyuk and Lozovyy (1961) and Savyn (1968), functions $\Phi(z)$ and $\Omega(z)$ at large $|z|$ can be presented as

$$\Phi(\mathrm{z}) = \mathrm{C}z/4 + O(1/z^2)$$
$$\Omega(z) = 3\mathrm{C}z/4 + O(1/z^2) \tag{4}$$
$$\mathrm{C} = \mathrm{M/I}$$

where $\mathrm{I} = 4\tilde{a}h^3/3$ is an inertia moment of the beam about neutral line of its transverse section.

From the boundary condition,

$$\left(\sigma_{yy} - i\sigma_{xy}\right)^+ - \left(\sigma_{yy} - i\sigma_{xy}\right)^- = 0, \mathrm{x} \in \tilde{L}$$

taking into account (2), we obtain

$$[\Phi(x) - \Omega(x)]^+ - [\Phi(x) - \Omega(x)]^- = 0, x \in \tilde{L}. \tag{5}$$

The solution of the linear conjunction problem (5), (4) is

$$\Phi(z) - \Omega(z) = -\frac{\mathrm{c}}{2}z. \tag{6}$$

On the basis of (1), we can write the following boundary condition:

$$\left(\sigma_{yy} - i\sigma_{xy}\right)^+ + \left(\sigma_{yy} - i\sigma_{xy}\right)^- = \begin{cases} 2\sigma_Y, x \in \tilde{L}_1; \\ 0, x \in L. \end{cases} \tag{7}$$

Taking into account (2), from (7), we obtain

$$[\Phi(x) + \Omega(x)]^+ + [\Phi(x) + \Omega(x)]^- = \begin{cases} 2\sigma_Y, x \in \tilde{L}_1, \\ 0, x \in L. \end{cases} \tag{8}$$

The solution of this linear conjunction problem is

$$\Phi(z) + \Omega(z) = \frac{\sigma_Y X(z)}{\pi i}\int_{\tilde{L}_1}\frac{dt}{X^+(t)(t-z)} + c_1 X(z)L, \tag{9}$$

where

$$X(z) = \sqrt{(z - d_1)(z - d_2)}, X^+(t) = i\sqrt{(d_1 - t)(t - d_2)},$$

c_1 is an unknown constant.

On the basis of (4) at large $|z|$, we can write

$$\Phi(z) + \Omega(z) = Cz + O(1/z^2). \tag{10}$$

As at large $|z|$

$$X(z) = z - \frac{1}{2}(d_1 + d_2) - \frac{1}{8}(d_1 - d_2)^2\frac{1}{z} + \dots,$$

$$\frac{X(z)}{t - z} = -1 + \frac{1}{z}\left(\frac{1}{2}(d_1 + d_2) - t\right) + \dots,$$

expanding right and left parts of formulas (9) into series at large $|z|$ and making equal the coefficients at equal powers of z, we receive

$$c_1 = C$$

$$-\frac{\sigma_Y}{\pi i}\int_{\tilde{L}_1}\frac{dt}{X^+(t)} - C\frac{1}{2}(d_1 + d_2) = 0$$

$$\frac{\sigma_Y}{\pi i}\int_{\tilde{L}_1}\frac{1}{X^+(t)}\left(\frac{1}{2}(d_1+d_2) - t\right)dt \qquad (11)$$

$$-\frac{C}{8}(d_1-d_2)^2 = 0$$

Using calculated integrals from Bronshteyn and Semendyaev (1967) formula (11) leads us to the system of transcendental equations for finding lengths $\Delta_i (i=1,2)$ of plastic strips at the crack tips:

$$\frac{2}{\pi}[\arccos((2+w_1-w_2)/\gamma_1)$$
$$\arccos((2+w_2-w_1)/\gamma_1)] = \tilde{\sigma}(2\tilde{x}+w_1-w_2) \qquad (12)$$

$$\tilde{\sigma}\gamma_1^2 = \frac{16}{\pi}\frac{w_1-w_2}{\sqrt{w_2(2+w_1)}+\sqrt{w_1(2+w_2)}}$$

where

$$w_i = \Delta_i/l, \tilde{x} = x_0/l, \tilde{\sigma} = Ml/(I\sigma_Y), \gamma_1 = 2 + w_1 + w_1.$$

Now, on the basis of (6) and (9), we have

$$\Phi(z) = \frac{C}{2}\left(X(z) - \frac{1}{2}z\right) + \frac{\sigma_Y X(z)}{2\pi i}\int_{\tilde{L}_1}\frac{dt}{X^+(t)(t-z)}, \qquad (13)$$

$$\Omega(z) = \Phi(z) + \frac{C}{2}z. \qquad (14)$$

Taking into account (3), we can write the expression for the derivative of the opening of the crack faces

$$2\mu[(u+iv)'^+ - (u+iv)'^-] =$$
$$\kappa[\Phi^+(x) - \Phi^-(x)] + \Omega^+(x) - \Omega^-(x), x \in \tilde{L}_1. \qquad (15)$$

From here, using (14),

$$2\mu\delta'_x(x) = 2\mu[v'^+ - v'^-] =$$
$$(\kappa+1)\text{Im}[\Phi^+(x) - \Phi^-(x)], x \in \tilde{L}_1. \qquad (16)$$

Taking into account (13) and calculating integrals (Bronshteyn, Semendyaev, 1967, Savruk et al. 1989), we obtain

$$\tilde{\delta}_1 = \frac{\gamma_1}{2}\left[\frac{\gamma_1\tilde{\sigma}}{4}\left(a_1\sqrt{1-a_1^2} - \arccos a_1\right) -\right.$$
$$\left. -\frac{1}{\pi}(\gamma_3 + \gamma_2\arccos a_1)\right] \qquad , \qquad (17)$$

$$\tilde{\delta}_2 = \frac{\gamma_1}{2}\left[\frac{\gamma_1\tilde{\sigma}}{4}\left(a_2\sqrt{1-a_2^2} + \arccos\tilde{a}_2\right) + \frac{1}{\pi}(\gamma_3 +\right.$$
$$\left. \gamma_2\arccos\tilde{a}_2)\right],$$

where

$$a_1 = (2+w_2-w_1)/\gamma_1, a_2 = (2+w_1-w_2)/\gamma_1, \tilde{a}_2 = -a_2, \gamma_2 = \sqrt{1-a_1^2} - \sqrt{1-a_2^2},$$

$$\gamma_3 = \frac{1}{2}(a_1-a_2)\ln\frac{1-a_1a_1-\sqrt{(1-a_1^2)(1-a_2^2)}}{1-a_1a_1+\sqrt{(1-a_1^2)(1-a_2^2)}},$$

$$\tilde{\delta}_i = \frac{2\mu\delta_i}{\sigma_Y(1+\kappa)l}, \delta_2 = \delta_a, \delta_1 = \delta_b. \qquad (18)$$

Account for (2), (7) and (8), we calculate stress tensor components on the faces of crack and on its extending using the formulas

$$\sigma_{yy}^* = \sigma_{yy}/\sigma_Y =$$
$$-\tilde{\sigma}X(x_1) + \frac{1}{\pi}(\arccos\tilde{\gamma}_1 + \arccos\tilde{\gamma}_2); \sigma_{xx}^* = \sigma_{xx}/\sigma_Y =$$
$$-\tilde{\sigma}x_1 + \sigma_{yy}^*, x_1 < \tilde{x} - 1 - w_2,$$

$$\sigma_{yy}^* = 1, \sigma_{xx}^* = \sigma_{xx}^{*\pm} = -\tilde{\sigma}x_1 + 1,$$

$$\tilde{x} - 1 - w_2 < x_1 < \tilde{x} - 1, 1 + \tilde{x} < x_1 < 1 + \tilde{x} + w_1; \quad (19)$$

$$\sigma_{yy}^* = 0, \sigma_{xx}^* = \sigma_{xx}^{*\pm} = -\tilde{\sigma}x_1, \tilde{x} - 1 < x_1 < \tilde{x} + 1;$$

$$\sigma_{yy}^* = \sigma_{yy}/\sigma_Y = \tilde{\sigma}X(x_1) + \frac{1}{\pi}(\arccos\tilde{\gamma}_1 + \arccos\tilde{\gamma}_2),$$
$$\sigma_{xx}^* = \sigma_{xx}/\sigma_Y = -\tilde{\sigma}x_1 + \sigma_{yy}^*, x_1 > 1 + \tilde{x} + w_1,$$

where

$$\tilde{\gamma}_1 = 1 - \frac{2w_1(x_1 - \tilde{d}_2)}{(x_1 - \tilde{d}_1 + w_1)(\tilde{d}_1 - \tilde{d}_2)},$$

$$\tilde{\gamma}_2 = 1 - \frac{2w_2(\tilde{d}_1 - x_1)}{(\tilde{d}_2 + w_2 - x_1)(\tilde{d}_1 - \tilde{d}_2)},$$

$$X(x_1) = \sqrt{(x_1 - \tilde{d}_1)(x_1 - \tilde{d}_2)}, \qquad (20)$$

$$\tilde{d}_1 = d_1/l = 1 + \tilde{x} + w_1, \tilde{d}_2 = d_2/l = \tilde{x} - 1 - w_2,$$
$$x_1 = x/l.$$

Note that based on (12), we can find out the condition under which $w_2 = 0$, that is, the length of the plastic strip at the nearest to the beam axe crack tip is zero. For example, given the external load $\tilde{\sigma}$, we obtain the following expression from the second equation (12):

$$\tilde{\sigma}(2+w_1)^2 = \frac{8\sqrt{2}}{\pi}\sqrt{w_1}, \qquad (21)$$

for calculating the length of the plastic strip at another crack tip. And from the first equation (12) at given $\tilde{\sigma}$ and obtained w_1, we determine the coordinate of crack centre $\tilde{x}_1 = x_0/l$

$$\tilde{x}_1 = \frac{1}{2}\left[\frac{2}{\pi\tilde{\sigma}}\arccos\frac{2-w_1}{2+w_1} - w_1\right]. \qquad (22)$$

Note also that equation (21) in w_1 has a solution up to some certain value $\tilde{\sigma}_0$ only. At $\tilde{\sigma} > \tilde{\sigma}_0$, it does not have the solution and satisfying the condition $w_2 = 0$ is impossible.

4. NUMERICAL ANALYSIS OF THE PROBLEM

The results of the calculations are given in Figures 2–7.

Graphical dependencies of dimensionless length of plastic strip and dimensionless opening the displacement of crack faces at crack tips on external load are given in Figures 2 and 3, correspondingly. In these figures, curves with label '1' correspond to the farther to the beam axis crack tip and curves with label '2' correspond to the nearer one. Figures 2(a) and 3(a) are constructed at $\tilde{x} = x_0/l = 1.5$, and Figures 2(b) and 3(b) are constructed at $\tilde{x} = 3$. It is seen from Figures 2 and 3 that, under fixed external load, the length of plastic strip and crack tip opening

values increases when crack centre moves from beam axis. On the basis of δ_κ model, the beam destruction starts from the farther (with respect to beam axis) crack tip.
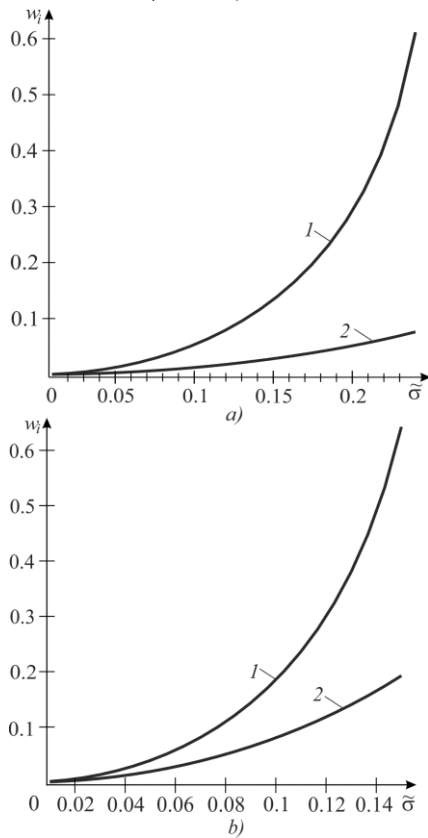
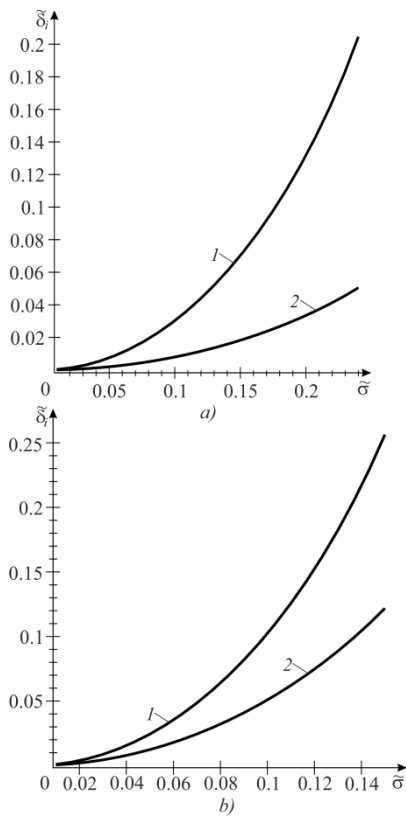**Fig. 2.** Graphical dependencies of relative length of plastic strip at crack tips on external load

Fig. 3. Graphical dependencies of dimensionless crack tip opening displacement on external load
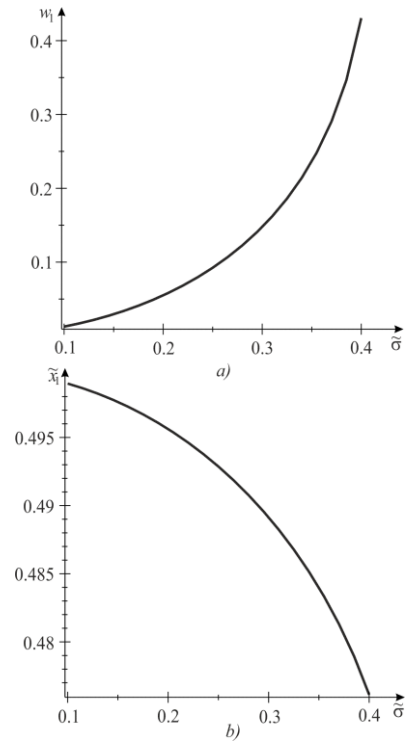
Fig. 4. Graphical dependencies of length of plastic strip at the crack tip (Fig. 4 a) and coordinate of crack centre, at which the length of plastic strip at nearer crack tip is zero, on external load
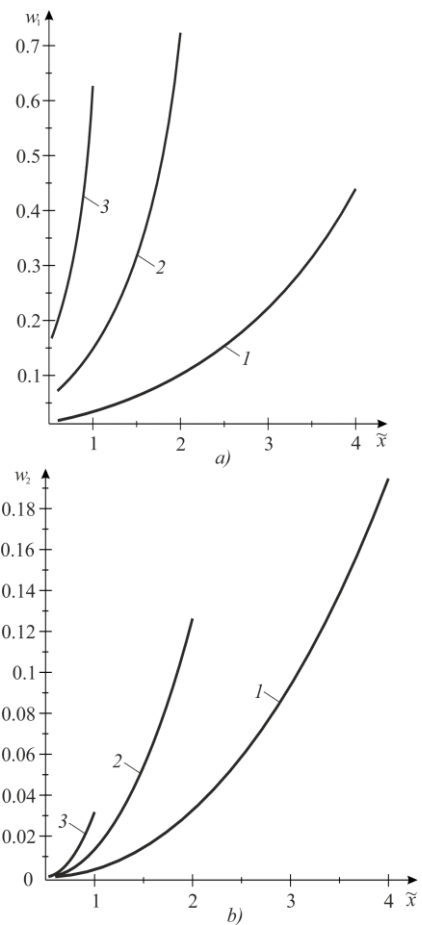
Fig. 5. Graphical dependencies of length of plastic strip at the crack tips on relative coordinate of crack centre $\tilde{x} = x_0/l$ at various values of external load

Figure 4 deals with case when the length of plastic strip at nearer to the beam axis crack tip is zero. The graphical dependencies of length of plastic strip at farther crack tip are given in Fig. 4(f). Figure 4(b) shows the graphical dependencies of coordinate of crack center for this case on external load attached to the beam. It is can be seen that increasing the value of external load leads to increasing the length of plastic strip at farther crack tip. At the same time, crack centre gets closer to the beam axis and the crack tip with zero plastic strip is strip of compressive stresses for the beam without crack.

Figure 5 demonstrates graphical dependencies of length of plastic strip in farther (Fig. 5a) and nearer (Fig. 5b) to the beam axis crack tips on relative coordinate of crack centre $\tilde{x}$ at several values of external load. Curves labelled as '1', '2' and '3', respectively, correspond to $\tilde{\sigma} = 0.1075$, $\tilde{\sigma} = 0.205$ and $\tilde{\sigma} = 0.3025$. Note that curves are constructed at $\tilde{x} > \tilde{x}_1$ and labels '1', '2' and '3' stand for $\tilde{x}_1 = 0.499$, $\tilde{x}_1 = 0.495$, and $\tilde{x}_1 = 0.489$, correspondingly. It is seen that decreasing the distance between crack centre and beam axis increases the length of the plastic strips at crack tip.
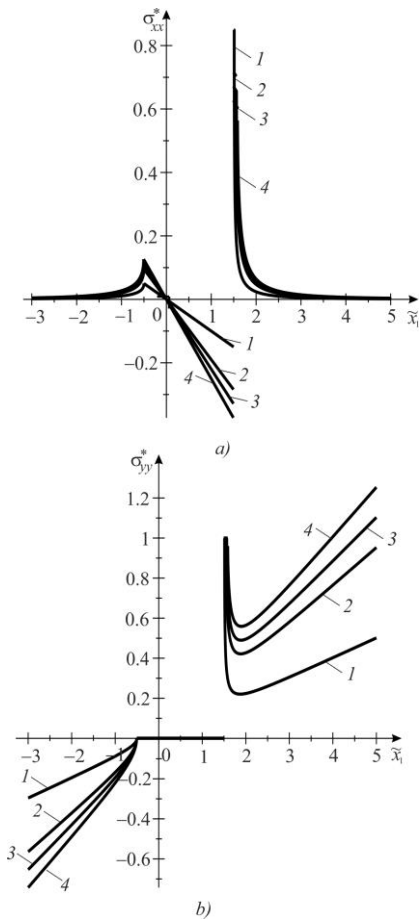
tive beyond the crack, but on the crack, they can be both positive and negative, everything depends on the position of crack center. σ_{xx}^* decreases away from the crack tips. From Figures 6(b) and 7(b), we see that stresses σ_{yy}^* beyond the crack tip b are constant in plastic strip at first, then decrease to some value and after that increase and become greater than 1 at a certain distance, that is $\sigma_{yy} > \sigma_Y$ (beam material goes into a plastic state). But beyond the crack tip a, they behave differently. As we can see from Figure 6(b), stresses σ_{yy} are negative when the length of plastic strip at this tip is zero. But for nonzero length, at first, they are equal to σ_Y in plastic strip and then decrease from positive values to negative ones.

a)

a)

b)

Fig. 6. Stress distribution on crack line at $\tilde{x} = \tilde{x}_1$ and various values of external load $\tilde{\sigma}$

b)
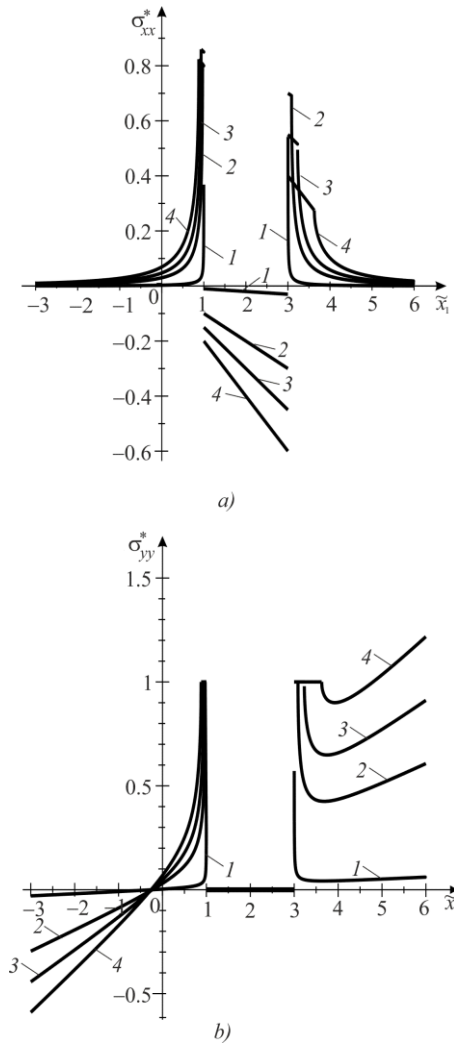
Fig. 7. Stress distribution on crack line at $\tilde{x} = 2$ and various values of external load $\tilde{\sigma}$

5. CONCLUSIONS

Numerical analysis of the problem confirms that the destruction of the strip (beam) with a crack perpendicular to its axis on the grounds of δ_K − fracture model for bodies with crack will start from the crack tip that is farther to the beam axis. A quantitative estimation of length of plastic zone and value of the opening of crack faces are also obtained. Note that the plastic strip is not always formed at the nearer (to the beam axis) crack tip, which is

In Figures 6 and 7, curves with label '1' are constructed at external load $\tilde{\sigma} = 0.01$, with label '2' at $\tilde{\sigma} = 0.1$, '3' at $\tilde{\sigma} = 0.15$ and '4' at $\tilde{\sigma} = 0.2$. Figures 6(a) and 7(a) show graphical dependencies of stresses $\sigma_{xx}^* = \sigma_{xx}/\sigma_Y$, and Figure 6(b) and 7(b) show graphical dependencies of stresses $\sigma_{yy}^* = \sigma_{yy}/\sigma_Y$. From Figures 6(a) and 7(a), we see that stresses σ_{xx}^* are always posi-

in the strip of compressive stresses for the beam without crack. But, in this case, there is no contact between crack faces, and the length of the plastic strip at this tip decreases when the tip removes from the beam axis. At some distance, this length becomes zero. As the distance increases, quantitative changes turn into qualitative ones, and perhaps, crack faces begin to contact. This requires a further investigation.

REFERENCES

1. **Bronshteyn I.N., Semendyaev K.A.** (1967), *Handbook of mathematics*, Science, Moscow.
2. **Fan M., Yi D.K., Xiao Z.M.** (2014), A Zener–Stroh crack interacting with a coated inclusion with generalized Irwin plastic zone correction, *International Journal of Solids and Structures*, 51 (19–20), 3399-3409.
3. **Kuz I., Kuz O., Sulym H.** (2015) Stress-strain state of elastic plate with an arbitrary smooth notch, *Acta Mechanica et Automatica*, 9 (4), 241-244.
4. **Kuz I.S., Moroz O.I., Kuz O.N.** (2019), Strength of elastoplastic plates containing square holes (inclusions) and cuts (thin inclusions) under uniaxial tension, *Materials Science*, 54 (4), 603–609.
5. **Monfared M.M., Bagheri R., Yaghoubi R.** (2018), The mixed mode analysis of arbitrary configuration of cracks in an orthotropic FGM strip using the distributed edge dislocations, *International Journal of Solids and Structures*, 130–131, 21-35.
6. **Muskhelishvili N.I.** (1966), *Some basic problems of the mathematical elasticity theory*, Science, Moscow.
7. **Nykolyshyn M.M., Opanasovych V.K., Kurotchyn L.R., Slobodyan M.S.** (2015), Biaxial tension of a piecewise homogeneous plate with two cracks on the interface of materials with regard for the plastic zones near their tips, *Materials Science*, 50 (6), 844-850.
8. **Nykolyshyn M.M., Opanasovych V.K., Kurotchyn L.R., Slobodyan M.S.** (2010), Biaxial tension of a homogeneous isotropic plate with two equal coaxial cracks with regard for plastic zones near their tips, *Journal of Mathematical Sciences*, 168 (5), 643-652.
9. **Ostash O.P., Chepil R.V., Vira V.V.** (2017), The assessment of fatigue life of notched components at uniaxial pulsating loading using the fracture mechanics approach, *International Journal of Fatigue*, 105, 305–311.
10. **Panasyuk V.V.** (1968), *Limit equilibrium of brittle bodies with cracks*, Naukova Dumka, Kyiv.
11. **Panasyuk V.V., Lozovyy B.L.** (1961), Bending of strips from a straight slit, *Applied Mechanics*, 7 (6), 627-634.
12. **Pavazza R.** (2000), An approximate solution for thin rectangular orthotropic/isotropic strips under tension by line loads, *International Journal of Solids and Structures*, 37 (32), 4353-4375.
13. **Prawoto Y.** (2012), How to compute plastic zones of heterogeneous materials: A simple approach using classical continuum and fracture mechanics, *International Journal of Solids and Structures*, 49 (15–16), 2195-2201.
14. **Savruk M. P., Osyv P. N., Prokopchuk I. V.** (1989), *Numerical analysis in the plane problems of crack theory*, Naukova dumka, Kyiv.
15. **Savyn G.V.** (1968), *Stress distribution near holes*, Naukova dumka, Kyiv.
16. **Shi P.P.** (2015), On the plastic zone size of solids containing doubly periodic rectangular-shaped arrays of cracks under longitudinal shear, *Mechanics Research Communications*, 67, 39-46.
17. **Sulym H., Opanasovych V., Slobodian M., Bilash O.** (2018), Combined bending with tension of isotropic plate with crack considering crack banks contact and plastic zones at its tops, *Acta Mechanica et Automatica*, 12 (2), 91-95.
18. **Unger D.J.** (2007), Numerical plane stress elastic–perfectly plastic crack analysis under Tresca yield condition with comparison to Dugdale plastic strip model, *Mechanics Research Communications*, 34 (4), 325-330.

PRACTICAL ASPECTS OF DESIGN AND TESTING UNMANNED AERIAL VEHICLES

Patryk SZYWALSKI[*], Andrzej WAINDOK[*]

[*]Faculty of Electrical Engineering, Automatic Control and Informatics Department of Electrical Engineering and Mechatronics,
Opole University of Technology, ul. Prószkowska 76, 45-758 Opole, Poland

p.szywalski@doktorant.po.edu.pl, a.waindok@po.edu.pl

Abstract: A design of an unmanned aerial vehicle (UAV) construction, intended for autonomous flights in a group, was presented in this article. The design assumptions, practical implementation and results of the experiments were given. Some of the frame parts were made using 3D printing technology. It not only reduces the costs but also allows for better fitting of the covers to the electronics, which additionally protects them against shocks and dirt. The most difficult task was to develop the proper navigation system. Owing to high costs of precision positioning systems, common global positioning system (GPS) receivers were used. Their disadvantage is the floating position error. The original software was also described. It controls the device, allows performing autonomous flight along a pre-determined route, analyses all parameters of the drone and sends them in a real time to the operator. The tests of the system were carried out and presented in the article, as well.

Keywords: Unmanned Aerial Vehicles (UAV), Unmanned Aerial Systems (UAS), Navigation System, Trajectory Generation

1. INTRODUCTION

The four-engine flying devices, colloquially called quadcopters or drones, are very popular. In the literature, they can be found under the name remotely piloted aircraft systems (RPAS; Gómez et al, 2019), unmanned aerial systems (UAS) and unmanned aerial vehicles (UAV; Roseneia Rodrigues Santos de Melo et al, 2017). Typically, the term unmanned aerial vehicles (UAV) is used for one quadcopter and the term unmanned aerial system (UAS) is used for drones in number greater than one.

There is a growing interest in UAV observed. This is especially visible in the statistics of popularity of the keyword 'drone' in the Science Network (Thompson Reuters). This brought about 3,000 results for the past 15 years and the number has increased particularly rapidly in the past 4 years (María de Miguel Molina, 2018). At present, only the Swiss university ETH Zurich, the American company Intel and the Chinese company EHang Egret have drone network projects. These institutions have been successful in connecting the devices into one independent system.

At present, there are many publications focusing on flight simulations of different manoeuvres of one or many UAVs. These papers describe devices that can be freely scaled, combined with each other, and study the thesis based on the simulation (Nallapaneni et al, 2018; Pulvera et al, 2018). These devices have found their application in both industry (e.g. in geodesy, parcel transport and building protection or photography; Bonali et al, 2019; Choudhary et al, 2019; Fujimori et al, 2018) and amongst ordinary people who use them for recreational purposes. There are also solutions in which devices, connected with each other, are able to provide access to the Internet in certain crisis areas (Aghaeeyan et al, 2015). The aim is also to integrate drones with autonomous cars (Khamseh et al, 2015; Kopiche et al, 2013).

The basic algorithm of stabilising an UAV in the overhang tends to stabilise three angles: pitch, roll and yaw (Fig. 1). Most control algorithms also have stabilisation of altitude, position and speed. To stabilise the pitch, roll and yaw angles, knowledge about their value is required. For this purpose, UAVs have a three-axis accelerometer and a three-axis gyroscope. Optionally, the device has a magnetometer to determine the direction along Earth's magnetic field (Ebeid et al, 2018).
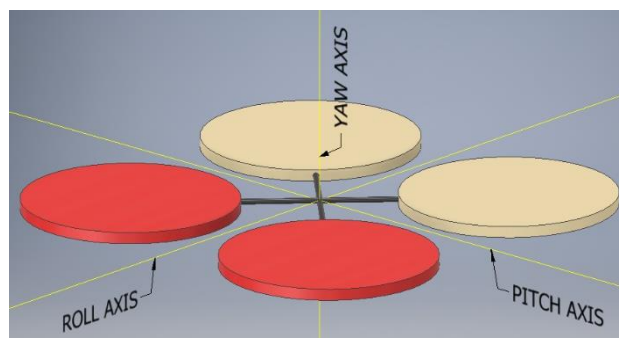
Fig. 1. Illustrative scheme of the UAV axis

The altitude parameter can be obtained from a barometric altitude sensor, laser sensor or other alternative navigation systems. The position of the device is taken from the navigation system, not necessarily global positioning system (GPS). Different alternative positioning systems, such as inertial navigation, video navigation or an indoor navigation system based on stationary ultrasonic beacons, are available. They are connected by radio interface in a license-free band (433 or 915/868 MHz; Sun, 2018).

Flight controllers with various processors can be found (Cetinsoy et al., 2012). The most popular is the STM 32 bit pro-

cessor in the F4 or F7 version. Ready modules (processor and basic sensors) are available from 20 Euro. The device can be used with a commercial software (often delivered with high-end equipment) or open-source software. The most popular of them are BetaFlight, CleanFlight, RaceFlight and iNav. The software allows programming the drone and configuring it for the flight.

In the article, practical aspects of design UAV are presented. The device is devoted for a drones' network and will be used in a testing of swarm algorithms based on nature such as swarm of bees, moths, ants, fishes and birds (Socha et al, 2008; Olivas et al, 2017; Luo et al, 2019). Construction of own device is necessary, because it is very difficult to purchase and modify a commercial UAV. The original construction allows fitting better the device for a specific application.

UAVs can be divided into several categories, for example, based on the number of engines, size or type of start (vertical or horizontal). However, the most common division is the number of engines: one, two, three, four or multi-engine drones can be distinguished (Szywalski et al., 2018, Puchała et al., 2015). In the

article, the construction of a four-engine device will be discussed.

2. STRUCTURE OF THE SYSTEM

In Figure 2 (and more detailed in Fig. 9) the structure of the system was shown. It is divided into three main parts:
- UAV (yellow) – this part presents one UAV, but it can be extended for an UAS
- Radio communication system (orange)
- Control and supervision software (green)

The UAV (or their collection) contains two STM32 processors, four drive units, sensors and a communication module. The whole system is mounted on a self-designed frame. Each processor has a pre-assigned task and priorities. In the first column (Fig. 2), priorities of the flight controller were shown. The most important task is to maintain the stability of the device, and the lowest priority is to maintain the right speed.

Unmanned Aerial Vehicles					Radio communication system	Control and Supervision Software				
STM F4	Data transfer UART	STM F2	Data transfer UART	Radio 433 MHz		Radio 433 MHz	Data transfer UART	M0	Data transfer UART	Computer
Stabilisation: pitch, roll and yaw	Data ↔	The autonomous flight algorithm	Data ↔	Data transmission	Data ↔	Data transmission	Data ↔	Intermediary module	Data ↔	Control panel
High stabilisation										
Position stabilisation										
Speed stabilisation										

Fig. 2. Structure of the system

The important element of the system is the radio communication module. It consists of radio modules mounted on each receiver in the network. For creating the network, 433-MHz RFM69 modules were used. The library RadioHead RFMxx was used to connect multiple clients by creating a network for data exchange. The system enables to exchange 60 bytes with a frequency of 20 Hz at a distance of up to 5 km (with appropriate antennas). The data transmission is encrypted with a 16-byte key. The created program is modular and allows adding drones (maximally 30) or flying out of operator's range (without a control panel).

The last module of the system is the control and supervision system controlled from the operator panel. To connect the computer to the network, a module that receives data from the radio network and sends it to the serial port on the computer was made. The software of the operator panel was created in MATLAB. This program processes data, draws relevant graphs and displays information.

3. DESIGN OF THE UAV

The goal of the project was to create a device with relatively high robustness to external forces, a flight time of minimum 15 min, weight up to 400 g, dimensions not exceeding 15 × cm × 15 cm × 15 cm and software enabling the device to be used in the network. In addition, it should be able to maintain integrity and availability during operations (if it is within operator's range). The

designed UAV should also be prepared for a navigation system that can determine the position of the device with an accuracy of 10 cm.

3.1. Description of electromechanical and electronic components used in the UAV

The challenge in the designing is the mechanical part, which should be characterised by high mechanical strength and low weight (in the presented case not exceeding 400 g). The central plate was milled from a carbon fibre-reinforced polymer (CFRP). The other elements were printed using a 3D printer. The print was made using the fused filament fabrication (FFF/FDM) method. It involves melting the material and laying it in thin paths, one next to another. The layers of plastic bond together, cooling down (Kownacki, 2016). For printing, the legs and two elements of the electronics housing the rubber material (TPU) and polycarbonate were used. The brass threads were embedded in the frame (Ferrarese et al, 2017), which was screwed using aluminium screws. The most important frame dimensions were given in Figure 3. The distance between the centre of mass (CoM) and axis of the propellers is also marked. The CoM is placed below the rotor line. The frame assembly is shown in Figure 4. Each element was sized and weighed. The mechanical part was designed in Inventor 2018.
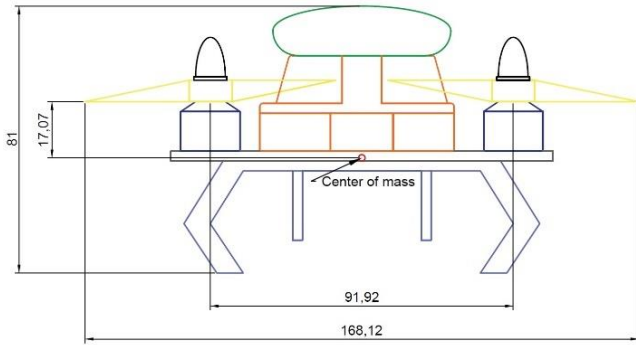
Fig. 3. Main dimensions of the drone and distance between the centre of mass and axis of the propellers (in mm)
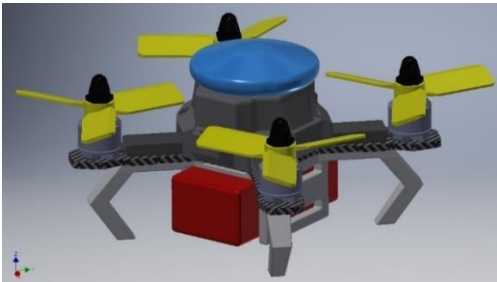
Fig. 4. Assembling of the frame elements

Table 1. Technical specification of the UAV controller

Controller
Processor: STM32F405 (168 MHz) and STM32F205RG (120 MHz)
Wi-Fi module: BCM43362 802.11b /G/N
Accelerometer/gyroscope: MPU6000 (SPI)
Radio module: RFM69HCW 433 MHz
Barometer: BMP280 (I2C)
Magnetometer: HMC5883 (UART)
GPS receiver: Ublox M8N (UART)
Blackbox: MicroSD card slot (SD/SDHC)
Beeper
Current/voltage sensor: 6-30 V/ 184 A (3-6S LiPo)
Step-down converter: 3.3 V, 4.5 V, 5 V – max. 3 A

The power unit of the device consists of four Readytosky 1306, 3100 KV engines and two pairs of propellers (2 x CW 3x3x3 and 2 x CCW 3x3x3). As the electronic speed controller (ESC) of the brushless direct-current motor (BLDC), the Little Bee 20A driver was selected (operates on the BlHeli software). The driver communicates with the controller using an OneShot125 protocol, which is characterised by eight times shorter pulses than the standard PWM protocol (from 125 to 250 µs). It allows for eight times faster update of the PID control loop (loop update time of 250 µs/4 kHz). The signal delay is also shorter: only 250 µs instead of 2000 µs. The OneShot125 protocol is needed for drones below 25 cm (diagonal distance of engines). MatekSys F405-CTR was chosen as the flight controller. It uses a powerful STM32F405 processor working at 168 MHz. In addition, the module has an inertial navigation system (IMU) sensor MPU6000, pressure sensor BMP280, blackbox – MicroSD (SD/SDHC), inverter for SBUS, PPM support, 6 x PWM, 5 x universal asynchronous receiver-transmitter (UART), SoftSerial, camera operation, operation programmable LEDs, beeper, current and voltage sensors and bat-

tery eliminator circuit (BEC) inverter. All parameters were included in Table 1.

The device was designed for using in a swarm of unmanned flying vehicles. Thus, the second module – Adafruit Feather WICED with the STM32F205RG processor – was added. The module will be used for communication with other UAVs and the operator. Its second task is to calculate the flight trajectory in a real time. The radio module – Adafruit FeatherWing LoRa RFM69 433MHz – was connected to it. Both modules can be mounted into a 'sandwich', creating one controller (Figs. 7 and 8).

The MatekSys 405-CTR module communicates with Adafruit Feather WICED via the serial port using the MSP protocol (Multi-wii Serial Protocol). The protocol works based on the client server. In this case, the master controller is Feather WICED Adafruit with the STM32F405 processor on board. It sends queries for specific parameters, calculates the predicted trajectory based on this and sends coordinates and other parameters (e.g. flight speed) to the flight controller. A detailed diagram of the system and the division of specific tasks between the single modules is shown in Figures 2 and 9. In Figures 5 and 6, the pictures of completed UAV are shown.

Fig. 5. Final construction – view from the side

Fig. 6. Final construction – view from the skew
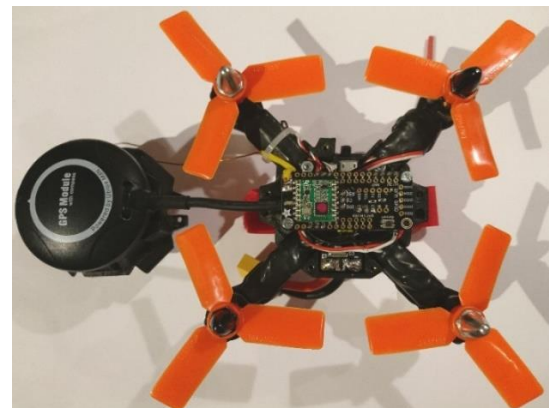
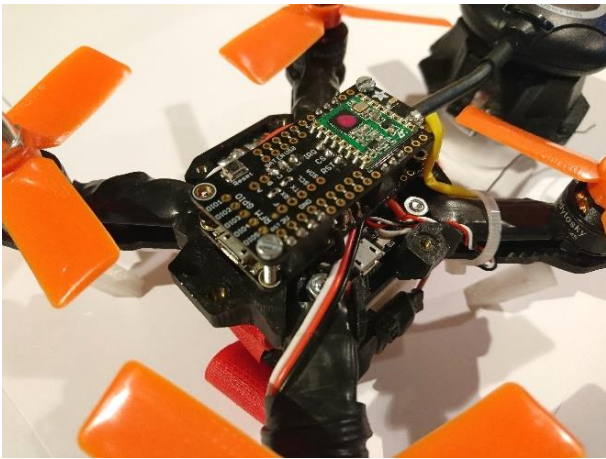**Fig. 7.** Electronics assembly – view from the top

Fig. 8. Electronics assembly – view from the skew

Table 2. Technical specification of the UAV

Quadcopter
Size without propellers: 12 cm × 12 cm
Size with propellers: 15.5 cm × 15.5 cm
Battery: Lithium polymer 11.1 V 1550 mAh
Type of propellers: 2xCW 3x3x3, 2xCCW 3x3x3
Weight: 365 gram
Motor BLDC: Readytosky 1306, 3100KV, 58.5W
ECS: Little Bee 20A BlHeli
Frame: class 130 • central plate: CFRP, • electronics housing: polycarbonate, • legs: thermoplastic polyurethane (TPU).

Specifications of the device were included in Table 2. The beeper was used in order to find the device after an unplanned or unsuccessful landing. For localisation, the Ublox M8N GPS receiver was used. The GPS receiver and magnetometer were placed on the top of the device. It is possible to find UAVs with a magnetometer built inside the machine, but in this case, motors or power supply often disturbs the measurement. Although the sensor is pulled out of the device, it is necessary to cancel the electromagnetic field generated by the motors and other components.

3.2. Schematic of electrical part

In Figure 9, the outline of electrical part of the entire system was shown. A yellow line surrounded the quadcopter block. In the centre, a flight controller is visible. Owing to the dynamics of the drone, the engines rotate in pairs in the opposite direction. Two types of propellers (clockwise [CW] and counterclockwise [CCW]) were used. They were assembled in such a way that the thrust is directed downwards. In the project, four three-phase BLDC motors were used. The device is powered by a 3-cell, 11.1 voltage polymer-lithium battery. Their big advantage is a very high discharge current. The battery allows power consumption up to 1 kW. In order to eliminate a voltage drops for the current peaks, a 470 µF, 25 V capacitor was added to the power connector. The F405-CTR module is equipped with step-down converter from 11.1 V to 3.3, 4.5 and 5 V. It serves as a source for powering the other modules (e.g. GPS, radio module and beeper). The GPS receiver and radio module communicates with the flight controller using the I2C bus. The magnetometer (mounted in the same housing as GPS) uses the SPI protocol.

A green line surrounds the operator supervision block. It consists of two modules (responsible for communication), a computer, original software (shown in Fig. 2), a safety button and a battery (980 mAh, 3.3 V). The battery is constantly recharged when the system is powered from the computer's USB port. Its main task is to maintain the battery voltage during a sudden power failure on the computer (e.g. discharge or power failure). This solution allows sending a landing order, even without the operator panel. For a protection, the system includes a safety button that is connected directly to the radio module. After pressing the button, regardless of whether the computer is on and/or other commands, the radio module sends an immediate order to land. The third block – radio communication – is surrounded with orange line.
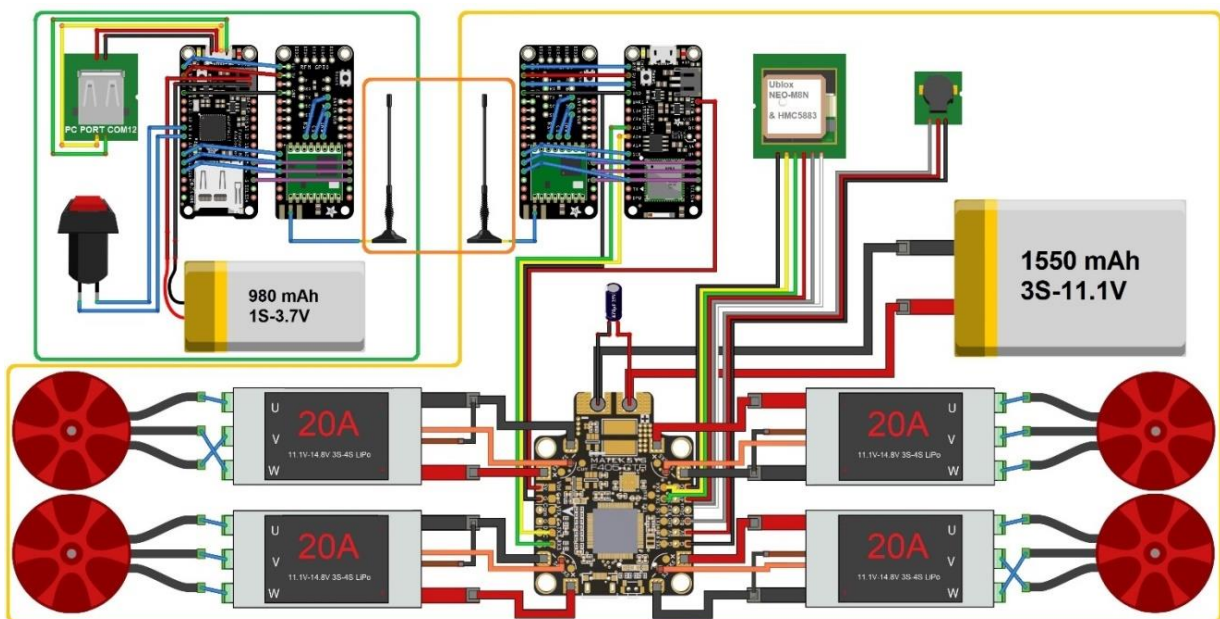

Fig. 9. Outline of the electric part

3.3. Navigation system

For autonomous flight, an unmanned flying unit must know its position in three-dimensional space. For this reason, it is necessary to use navigation systems. The most popular and easiest to use is GPS. Its biggest advantage is the possibility of using it all over the globe. To determine the position in three-dimensional space, it is necessary to connect the receiver with a minimum of three satellites. The accuracy of the position increases with the number of connected satellites. The system has been configured forcing a connection with a minimum of six satellites. A smaller number of satellites do not allow starting in the GPS-assisted mode. At present, the most popular receiver of the GPS signal is Ublox NEO-M8N. Its disadvantage is accuracy not exceeding 2.5 m in relation to latitude/longitude and about 5 m in relation to altitude.

In Figures 10 and 11, the static characteristics of the tested receiver were shown. The experiment was performed using the iNav software. The measurement was performed in the following way: the receiver was turned on in an unbuilt area and the maximum displacement during 10 min and during 10 s was measured. The experiment was started only after establishing communication with a minimum of 12 satellites. By converting the longitude and latitude values to meters, it is assumed that the Earth is a sphere, not an ellipsoid, and that the errors in the shipments tested (not exceeding 10 km) are not large enough to affect the results (Szywalski et al, 2018).
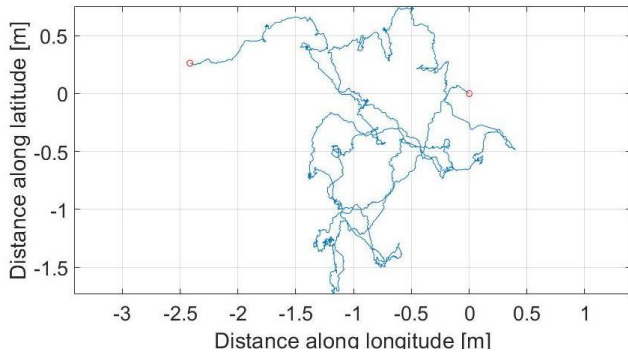

Fig. 10. Static 2D characteristics of GPS receiver
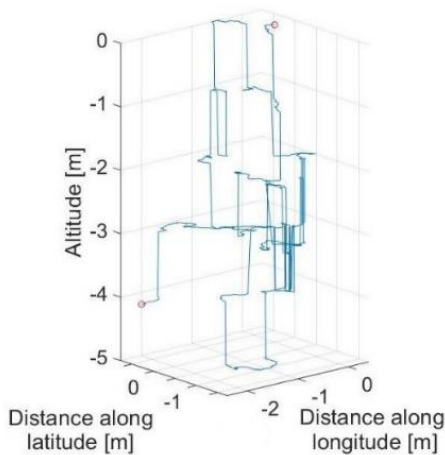(10 min of measuring)

Fig. 11. Static 3D characteristics of GPS receiver
(10 min of measuring)

In order to evaluate the navigation system, an error for a sample of 10 min and 10 s was calculated. The value of 10 min is important for long flights. It indicates how far the destination can be moved. The deviation was also calculated for 10 s period because, in this time, the device passes between the neighbouring points. Detailed analysis of the results showed that the maximum difference between the measurement (longitude and latitude) in the sample *n* and *n + 1* was not greater than 14 cm, and the average was 4 mm. This is important because, although the accuracy of the system is several metres, the measurement value does not change significantly between the two measurement points. The results related to the displacement from the starting point P0 = (0,0,0) are given in Table 3.

The altitude value is characterised by a relatively larger error compared to longitude and latitude values. This error can be minimised with using an additional barometric height sensor. The sensor uses the dependence of the pressure verso the height according to the formula (Zhu et al., 2013):

$$h = \frac{T_o \left(\left(\frac{p}{P_0} \right)^{-\frac{R \cdot L_0}{g_0 \cdot M}} - 1 \right)}{L_0} \tag{1}$$

where h is the altitude above sea level (in m); T_o is the standard temperature above sea level 288.15 K; L_0 is the constant of temperature change, 0.0065 K/m; p is the measured pressure in hPa; P_0 is the static pressure 1013.25 hPa; g_0 is the acceleration of gravity, 9.80665 m/s^2; M is the molar mass of air, 0.0289644 kg/mol; and R is the gas constant, 8.31432 J/(mol*K)

The barometric height sensor is able to measure several dozen centimetres with the assumption that the sensor is not affected by any external factors: air turbulence generated by the drive units, wind or temperature fluctuations. The sensor must be mounted at a suiTab. placed away from the elements that can heat up during the work. In the presented construction, it was additionally wrapped with a sponge.

Tab.3. Static measurement results for the Ublox NEO-M8N GPS

Error type		Distance along latitude (m)	Distance along longitude (m)	Altitude (m)
Measurement for 10 min	Average distance from P0	0.616	0.903	2.955
	Span of the measurement	2.482	2.816	5
	Max distance from P0 in R3	5.553		
Measurement for 10 s	Average distance from P0	0.576	0.465	0.87
	Span of the measurement	0.99	1.057	1
	Max distance from P0 in R3	1.435		

The overworked control algorithm takes into account the values taken from the GPS and from the barometric altitude sensor. In addition, in order to increase the accuracy, a radar could be used (radar altimeter and electronic altimeter). By means of appropriate fusion algorithms, for example, Kalman, the height can

be determined with an accuracy of a few centimetres (Cho et al, 2011, Cai et al, 2008). An another solution is Inertial Navigation System (INS), Vision Navigation System (VNS) or INS/VNS fused by a Kalman filter (Huang et al, 2018; Stančić et al, 2010; Cechowicz et al, 2017).

3.4. Open-Source flight controller software

The control algorithm was made based on an open-source flight software. Before starting, it was necessary to properly connect, configure and calibrate the sensors, as well as to select the flight mode. At present, it is possible to find many open-source programs to control a quadcopter with a STM32 processor. The software can be divided according to the function:

- CleanFlight – is characterised by a stable and easy-to-use code. It is updated, on an average, once a quarter. At present, it supports STM32 processors – F1, F3, F4 and F7.
- BetaFlight – experimental software. On an average, new features appear once a week. It supports STM32 processors – F1, F3, F4 and F7.
- RaceFlight – created especially for racing drones. To increase the operating frequency of the control loop, some unnecessary stabilisation functions and GPS module were removed. It supports STM32 – F4 and F7 processors.
- iNav – is a software created for GPS flights and Return to Home (RTH) functions. It is used mainly for recording movies from the air and GPS-assisted flights. It is supports STM32 – F3, F4 and F7 processors.

Cleanflight, BetaFlight and iNav can be used on multirotor aircrafts and fixed-wing aircraft. They support a variety of shapes and motor counts not limited to quadcopters, hexacopters, octocopters, tricopters and planes. The iNav software was selected according to the intended use of the device. An advantage is a big pressure of the creators on a sTab. and precise flight using the navigation systems.

A useful function of the iNav software is the RTH and Waypoint (WP) algorithm. In the presented solution, the RTH functions is used as a safeguard – for example, loss of communication or other errors (e.g. from navigation systems). The accuracy of the function has been tested and the device actually lands at a maximum distance of 2.5 m from the starting point. WP functions were used to control the device. The STM32F2 driver calculates the direction of the flight and sends it to the flight controller in the form of point coordinates and speed of reaching it. It is important that the target point should be not too near to the actual position of the device – in such a case, the system recognise the point as completed. This is due to the accuracy of GPS. In the presented construction, the version of iNav 2.1.3 and the Firmware for MATEK405 2.0.1 were used.

3.5. Planning and generating trajectories

Original software was created to operate the drone, allowing generating a trajectory, sending it to the device and supervising the quadcopter during the flight. The whole system consists of a quadcopter, a communication system and a PC-class computer. The final trajectory consists of several shapes (line, circle and helix; Szywalski, 2017). It was assumed that the user should define the characteristic points of each partial shape and define the type between the points. It is possible to create a shape and

then duplicate it. Owing to the inaccuracy of navigation systems, each result has an error, so it is impossible for the device to reach a certain point directly. Therefore, around each point a region was defined – it has a sphere shape characterised by a diameter of 1.5 m. The diameter parameter can be modified depending on the flight accuracy. When the distance between the main points is bigger than the declared accuracy, the program will automatically calculate intermediate points in such a way that the defined shapes are maintained. The idea of the algorithm is to generate a virtual tunnel in which the device should move. When the UAV reaches the defined zone, it is assumed that the point was reached and the device can fly to the next one.

The arrows in Figure 12 indicate the order of the points (flight direction). The flight path is marked in green. The cross section of the track is a circle. For this example, 1 m was accepted as the distance between the intermediate points. Increasing this parameter reduces the accuracy of the flight. By defining the distance (between the intermediate points) and the regions around them, the accuracy of the GPS should be taken into account. The software allows re-calling predefined shapes, scaling them and saving.
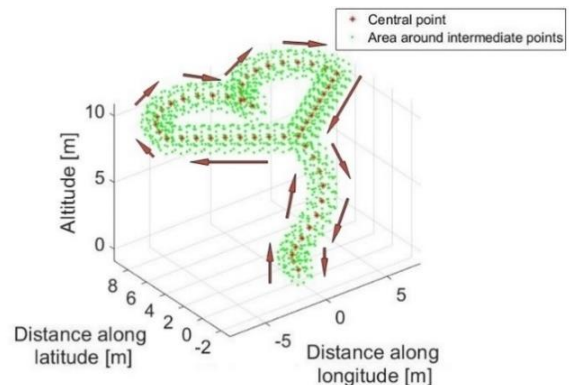

Fig. 12. Trajectory in the shape of a heart

3.6. Operator panel

In order to test the UAV work for different trajectories, the original software made in MATLAB was used. The operator panel is shown in Figure 13. The software allows generating or importing a flight trajectory from an external, previously created file. The whole software works in a real time and displays following parameters: start position, current position, distance from the starting point, number of visible satellites of the GPS system, statistics of data transmission, battery voltage, instant current consumption and energy consumption, and draws a displacement in three and two axes. The 2D drawing has additionally a graph, which shows how the device is turned to the north. The data can be saved to an external file and replayed.

The software was also created by taking into account the flight safety and to predict the discharge of the battery. To detect early errors in the data transmission between the operator and the drone, all of the parameters are analysed. In the normal operating mode between the operator and the drone, 15 device parameters are sent in 56 bytes. The system evaluates the correctness of the parameter based on predefined rules (Table 3). When the parameter is incorrect, dm is 1. Then the sum of the incorrect parameters is counted and multiplied by their predicted length in bytes. Missing data packet (all n parameters) in 100 ms time increases

the t_err counter. As a result, the system calculates the error of false or missing bytes in relation to the predicted bytes in data transmission according to the following formula:

$$err = \frac{\sum_{i=1}^{nd}\left(\sum_{j=1}^{n}(dm_j \cdot dp_j)\right) + (t\_err \cdot dp\_size)}{nd \cdot dp\_size \cdot 0.01} \quad (2)$$

nd is the number of demanded packets, *n* is the number of sent parameters (in our case 15), *dm* is the data message (1 represents error and 0 is correct parameter), dp_j is the number of bytes of *j*-th parameter, *dp_size* is the data packet size (normally 56 byte) and *t_err* is the counter for missing data packages.

The resulting ratio is expressed as a percentage of how much data has been lost. For a value above 20%, the device returns autonomously to the starting point. In the tests, the parameter was below 3%, which is within the limits of acceptance.

In Table 4, a list of all parameters that are sent from the device to the operator is presented. For each parameter, its number of bytes and boundary conditions were defined. If either condition is not met, the system sends a message consisting of zeros and (on the last byte) 'e', for example, '00000e' for a parameter of 6 bytes. Thus, the system knows that the parameter was read incorrectly or changed when sending to the operator. To minimise the data package, parameters GPS_LON and GPS_LAT are reduced from 9 to 6 bytes. The system has the first 3 bytes permanently assigned (they have a constant value). The result is the reduction of the zone (to 7.1 km × 11.1 km) in which the device can move. In the M1-M4 parameters, additional messages were programmed:

- 0–50: the messages inform about the motor arming,
- 50–950: motor speed,
- 950– 999: motor error messages.
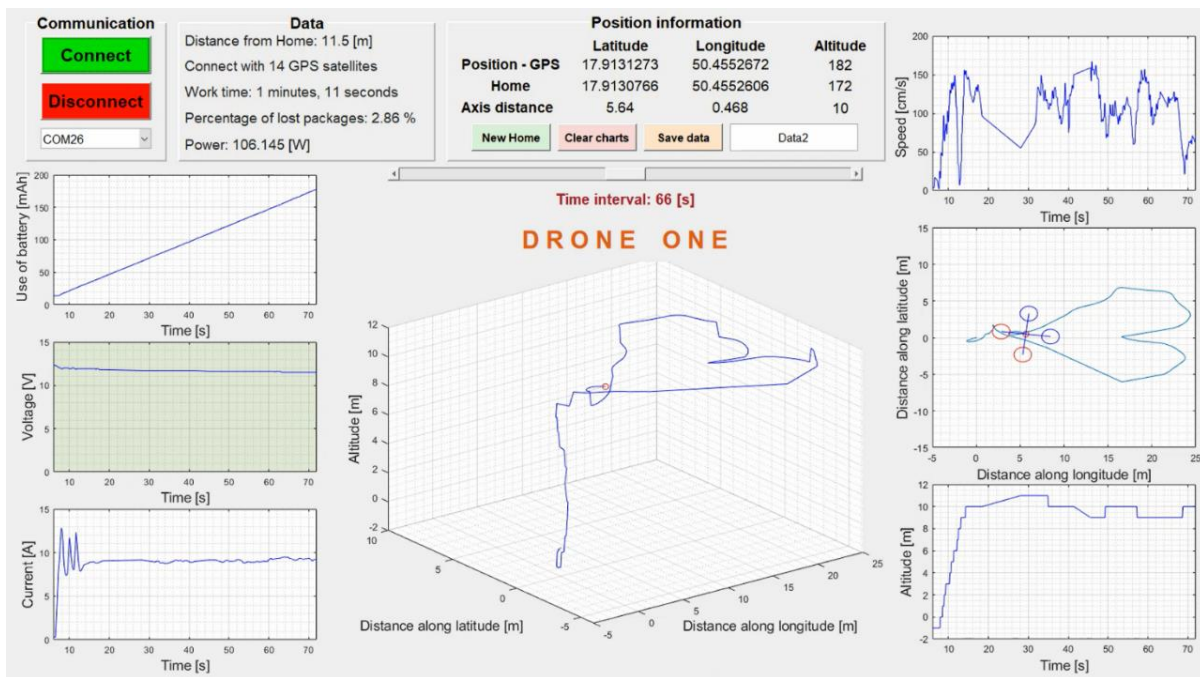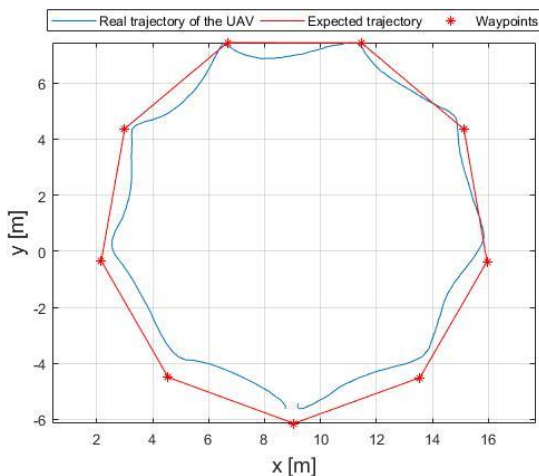

Fig. 13. Operator panel

Fig. 14. Flight along a circle with a diameter of 14 m(flight speed: 75 cm/s; wind speed: 4 m/s): the average path error is 0.4 m and the maximum path error is 0.96 m
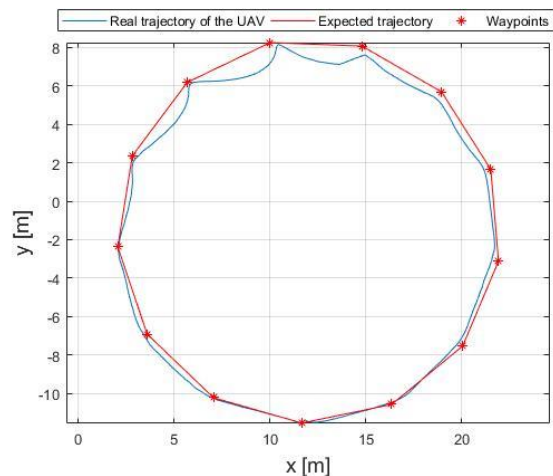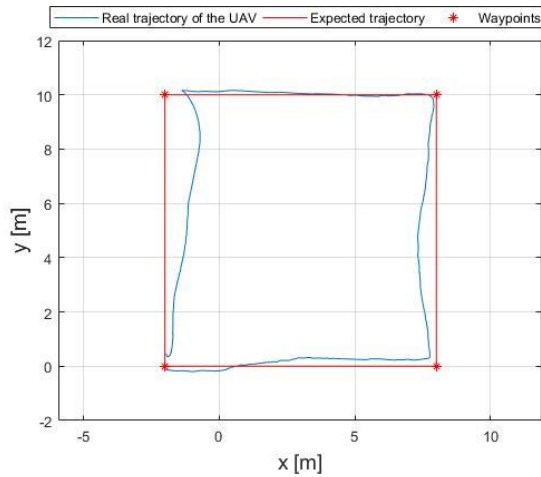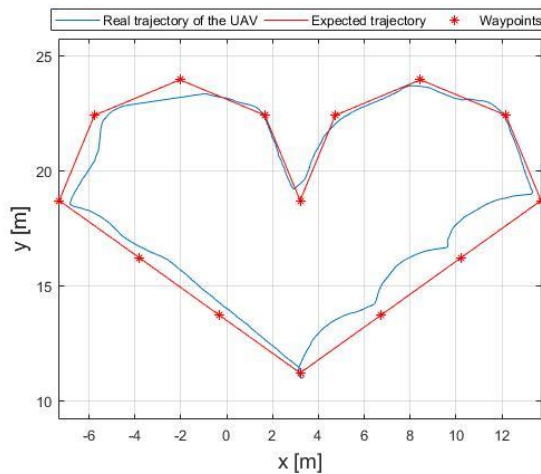

Fig. 15. Flight along a circle with a diameter of 20 m (flight speed: 150 cm/s; wind speed: 4 m/s): the average path error is 0.28 m and the maximum path error is 1.13 m

Fig. 16. Flight along a rectangle with a side length of 10 m (flight speed: 75 cm/s; wind speed: 4 m/s): the average path error is 0.3 m and the maximum path error is 1.29 m

Fig. 17. Flight along a heart trajectory (flight speed: 150 cm/s; wind speed: 4 m/s): the average path error is 0.38 m and the maximum path error is 1.36 m

The energy consumption is calculated, as well. On the basis of these tests, it is possible to predict the discharge of the battery. There are many publications devoted to this issue. One of the most effective solutions includes neural network (Souza et al, 2016). The graphs on the left of Figure 13 show (from above): energy consumption in mAh, battery voltage and instant current consumption. The energy consumed is expressed in mAh, which allows direct comparison of the value to the nominal capacity of the battery. The second graph shows the voltage on the battery. If the voltage drops below 10.8 V (3.6 V on one cell), the background will change to yellow, and if it drops below 9.6 V (3.2 V on one cell), background will change to red indicating battery discharge and immediate landing. The green background of the graph indicates the correct battery voltage. The bottom chart shows the instantaneous current consumption. On its basis, the power consumption of the device can be calculated (in the presented case, it is 106.145 W – the device was in the overhang). During the programming process, the device consumes about 0.7 W, and when the battery and ECS drivers are connected, it consumes 3.4 W.

In the centre of Figure 13, a graph with the UAV displacement in three axes is shown. It should be noted that the charts have been drawn relative to the local coordinate system where the point

(0, 0, 0) is the place where the engines are armed – the device is starting. On the right side, three graphs are present – the data from the GPS receiver. The top plot shows the current speed of the device – in our case, it is 100 cm/s. The value is characterised by an error, which is due to the low priority of the control algorithm. An accurate speed measurement can be performed based on the visual and inertial information without GPS. In this method, no map and no artificial landmark of the environment are required – only the off-the-shelf onboard sensors in a multicopter including a low-cost inertial measurement unit (IMU), a downward-looking monocular camera and an ultrasonic range finder facing downwards are needed to constitute the vision motion constraint (Deng et al, 2018). The middle graph shows the device displacement in 2D. The current position of the device is shown by the graphics of a four-engine drone. The front of the device is marked in red. This graphic rotates according to the actual rotation of the device. The last graph shows the altitude parameter.

Table 4. List of device parameters and their length in bytes

	Parameter	Number of bytes	Rules causing an error
1	GPS_LON	6	Size > 6 || GPS_LON > 180000000 || GPS_LON < 178000000
2	GPS_LAT	6	Size > 6 || GPS_LAT > 505000000 || GPS_LAT < 503000000
3	GPS_ALT	3	Size > 3 || GPS_ALT > 999 || GPS_ALT < 120
4	GPS_numSat	2	Size > 2 || GPS_numSat > 20 || GPS_numSat < 0
5	angx	4	Size > 4 || angx > 180 || angx < -180
6	angy	4	Size > 4 || angy > 180 || angy < -180
7	heading	4	Size > 4 || heading <= 0 || heading >= 360
8	vbat	3	Size > 3 || vbat > 200 || heading < 0
9	mAhDrawn	4	Size > 4 || mAhDrawn > 2000 || mAhDrawn < 0
10	amperage	4	Size > 4 || amperage > 9999 || amperage < 0
11	GPS_speed	4	Size > 4 || GPS_speed > 9999 || GPS_speed < 0
12	M1	3	Size > 3 || M1 > 999 || M1 < 0
13	M2	3	Size > 3 || M2 > 999 || M2 < 0
14	M3	3	Size > 3 || M3 > 999 || M3 < 0
15	M4	3	Size > 3 || M4 > 999 || M4 < 0

4. SUMMARY

The autonomous flight tests were made for different trajectory shapes. Owing to clarity, the demanded and measured trajectories were shown in 2D plane (Figs. 14–17). The differences between them do not exceed the GPS error, which confirms the correctness of the UAV construction and control algorithms. The movies, showing the completed operator panel during the work for tested trajectories are available on YouTube under links given in References 32 (circle with 14-m diameter), 33 (circle with 20-m diameter), 34 (rectangle) and 35 (heart trajectory).

The developed device can flight up to 16 min in the autonomous mode. The structure of the system is scalable. The test shows that the UAV works sTab. and flights in autonomous mode with or without the operator panel. In addition, the RTH and WP algorithms work correctly.

The average path error (deviation between demanded and real flight path) during the flight did not exceed 0.4 m, whereas the maximum path error was below 1.4 m. It was found that increasing the number of intermediate points reduces the error value. Considering the flight using GPS, the obtained error values are satisfactory. The use of more accurate navigation systems (e.g. local), which will be tested in further work, should reduce these errors.

The mechanical elements made using 3D print technology met the expectations. The housing withstood the tests and protected the electronic part of the device. All assumptions were achieved.

The system was made for further studies related to the optimisation of the flight. The presented UAV will be used in testing of swarms algorithms.

REFERENCES

1. **Aghaeeyan A,, Abdollahi F., Talebi H.A.,** (2015), UAV–UGVs cooperation: With a moving center based trajectory, *Robotics and Autonomous Systems,* 63, Part 1,1-9.
2. **Bonali F.L., Tibaldi A., Marchese F., Fallati L., Russo E., Corselli C., Savini A.,** (2019), UAV-based surveying in volcano-tectonics: An example from the Iceland rift, *Journal of Structural Geology*, 121, 46-64.
3. **Cai G., Feng L., Chen B., Lee T.H.,** (2008), Systematic design methodology and construction of UAV helicopters, *Mechatronics 18*, 545–558.
4. **Cechowicz R.,** (2017), Bias drift estimation for mems gyroscope used in inertial navigation, *Acta Mechanica et Automatica*, 11(2), 104-110.
5. **Cetinsoy E., Dikyar S., Hancer C., Oner K.T., Sirimoglu E., Unel M., Aksit M.F.,** (2012), Design and construction of a novel quad tilt-wing UAV, *Mechatronics 22,* 723–745.
6. **Cho A., Kang Y.S., Park B., Yoo Ch.S., Koo S.O.,** (2011), Altitude Integration of Radar Altimeter and GPS/INS for Automatic Takeoff and Landing of a UAV, *2011 11th International Conference on Control*, Automation and Systems, Gyeonggi-do, Korea, 1429-1432.
7. **Choudhary G., Sharma V., You I.**, (2019), Sustainable and secure trajectories for the military Internet of Drones (IoD) through an efficient Medium Access Control (MAC) protocol, *Computers & Electrical Engineering,* 74, 59-73.
8. **Deng H., Arif U., Fu Q., Xi Z., Quan Q., Cai K.,** (2018), Visual–inertial estimation of velocity for multicopters based on vision motion constraint*, Robotics and Autonomous Systems*, 107, 262-279.
9. **Ebeid E., Skriver M., Husum K., Jensen K., Pagh U**., (2018), A Survey of Open-Source UAV Flight Controllers and Flight Simulators, *Microprocessors and Microsystems*, 61, 11-20.
10. **Ferrarese G., (2017), Bandwidth Assessment for MultiRotor UAVs,** *Acta Mechanica et Automatica*, 11(2), 150-153.
11. **Fujimori A., Ukigai Y., Santoki A., Oh-hara S.,** (2018), Autonomous flight control system of quadrotor and its application to formation control with mobile robot. *IFAC-PapersOnLine*, 51(22), 343-347.
12. **Gómez A., Rodríguez A., Sanchez C., Luis G., Hernández C., Cuerno R.,** (2019), Remotely Piloted Aircraft Systems conceptual design methodology based on factor analysis, *Aerospace Science and Technology*, 90, 368-387.
13. https://www.youtube.com/watch?v=4rh5Z1fHzq4&feature=youtu.be (access on 23.12.2019).
14. https://www.youtube.com/watch?v=4WOrWoNT-bM&feature=youtu.be (access on 23.12.2019).
15. https://www.youtube.com/watch?v=eJ9QhFdsagQ&feature=youtu.be (access on 23.12.2019).
16. https://www.youtube.com/watch?v=tq4ihl6fRDg&feature=youtu.be (access on 23.12.2019).
17. **Huang L., Song J., Zhang Ch., Cai G.,** (2018), Design and performance analysis of landmark-based INS/Vision Navigation System for UAV, *Optik*, 172, 484-493.
18. **Khamseh H.B., Janabi-Sharifi F., Abdessameud A.,** (2018), Aerial manipulation—A literature survey, *Robotics and Autonomous Systems*, 107, 221-235.
19. **Kopichev M., Ignatiev K., Putov A.,** (2013), Autonomous Control and Stabilization System for Unmanned Aerial Vehicles, *IFAC Proceedings Volumes*, 46(30), 240-243.
20. **Kownacki C.,** (2016), Multi-UAV Flight on the Basis of Virtual Structure Combined with Behavioral Approach, *Acta Mechanica et Automatica*, 10(2), 92-99.
21. **Luo Q., Yang X., Zhou Y.,** (2019). Nature-inspired approach: An enhanced moth swarm algorithm for global optimization, *Mathematics and Computers in Simulation,* 159, 57-92.
22. **María de Miguel Molina, Virginia Santamarina Campos, M. Ángeles Carabal Montagud, Blanca de Miguel Molina,** (2018), Ethics for civil indoor drones: A qualitative analysis, *International Journal of Micro Air Vehicles*, 10(4), 340–351.
23. **Nallapaneni Manoj Kumara, Sudhakar K., Samykano M., Jayaseelan V.,** (2018), On the technologies empowering drones for intelligent monitoring of solar photovoltaic power plants, *International Conference on Robotics and Smart Manufacturing (RoSMa2018),* Procedia Computer Science, 133, 585–593.
24. **Olivas F., Valdez F., Castillo O., González C.I., Martinez G.E., Melin P.,** (2017), Ant colony optimization with dynamic parameter adaptation based on interval type-2 fuzzy logic systems, *Appl. Soft Comput*, 74-87.
25. **Puchała K., Szymczyk E., Jachimowicz J.,** (2015), FEM design of composite – metal joint for bearing failure analysis, *Przegląd Mechaniczny*, 33 – 41.
26. **Pulvera A., Weib R.**, (2018), Optimizing the spatial location of medical drones, *Applied Geography,* 90, 9–16.
27. **Roseneia Rodrigues Santos de Melo, Dayana B.C., Juliana Sampaio Álvares, Irizarry J.,** (2017), Applicability of unmanned aerial system (UAS) for safety inspection on construction sites, *Safety Science*, 98, 174-185.
28. **Socha K., Dorigo M.,** (2008), Ant colony optimization for continuous domains, *European Journal of Operational Research,* 1155-1173.
29. **Souza D., Pinto V., Nascimento L., Torres J., Gomes J., Sa-Junior J., Sa-Junior J., Almeida R.,** (2016), Battery Discharge forecast applied in Unmanned Aerial Vehicle, *Przegląd Elektrotechniczny* 02/2016, 185-192.
30. **Stančić R. Graovac S.,** (2010), The integration of strap-down INS and GPS based on adaptive error damping, *Robotics and Autonomous Systems*, 58(10), 1117-1129.
31. **Sun J., Li B., Wen Ch.Y., Chen Ch.K.,** (2018), Design and implementation of a real-time hardware-in-the-loop testing platform for a dual-rotor tail-sitter unmanned aerial vehicle, *Mechatronics* 56, 1–15.
32. **Szywalski P.,** (2017), Design of the autonomous flight algorithm for Unmanned Aerial System, Opole, 4-61
33. **Szywalski P., Waindok A.,** (2018), Analysis of the quadrocopter class 130 frame deformation made with using 3D printing technology*, Przegląd Mechaniczny*, 39-44.
34. **Szywalski P., Wajnert D., (2018),** Possibility Analysis of the Location Measurement by Using the GPS Receiver and Barometric Altimeter, *Pomiary Automatyka Robotyka*, 33-39.
35. **Zhu W., Dong Y., Wang G., Qiao Z., Gao Z.,** (2013), High-precision Barometric Altitude Measurement Method and Technology, *2013 IEEE International Conference on Information and Automation (ICIA)*, 430-435.

AN EXPLORATORY STUDY ON THE ACCURACY OF PARTS
PRINTED IN FDM PROCESSES FROM NOVEL MATERIALS

Halina NIECIĄG,[*] Rafał KUDELSKI,[*] Piotr DUDEK,[*] Jacek CIEŚLIK[*]

[*]Faculty of Mechanical Engineering and Robotics, Department of Machine Design and Technology,
AGH University of Science and Technology, Al. Adama Mickiewicza 30, 30-059 Kraków, Poland

hnieciag@agh.edu.pl, kudelski@agh.edu.pl, dudek@agh.edu.pl, cieslik@agh.edu.pl

Abstract: The paper describes the experiment of assessing the chosen geometric characteristics of test models with simple geometry, shaped by the FDM (fused deposition modelling) method of different materials. The influence of the material grade and the degree of infill density on the shrinkage affecting their dimensional deviations and selected surface topography parameters of printed parts was examined and compared. Three different types of materials were used to fabricate the test models, namely HDGLASS and NANOCARBON, two new fibre reinforced composites available in the market and, additionally ABS, a popular monoplastic material. An infill density ratio of 10, 50 and 90% was assumed for each material. Three specimens were made on the same printer for each infill density, which allowed to assess the repeatability of the analysed characteristics. From among many possible shapes of models, a cube was chosen as representing the simplest geometry, facilitating the measurements themselves and the interpretation of the results. New fibre-reinforced materials are more attractive in industrial applications than pure plastics (ABS) due to their mechanical properties or appearance. They are characterized by a relatively low melting point and short cooling time, after which they can return to their original geometry; however, there is a lack of detailed data on the geometric accuracy of parts made of used composite materials. The presented work was to explanatorily broaden the knowledge about the properties of composite made parts. The practical purpose of the research was that on the basis of measurements, it would be possible to indicate among the materials used that particular material whose properties and method of application would allow obtaining the best quality surface and would be the most resistant to thermal loads. An attempt was also made to explain the possible causes of the differences in the observed characteristics of the tested materials.

Keywords: FDM, thermoplastic filament materials, geometrical accuracy

1. INTRODUCTION

Additive manufacturing (AM) is a popular alternative to subtractive manufacturing and formative manufacturing methodology. Products shaped by this technology, also called as 3D printing, are made from 3D model data, usually by adding layer upon layer (ISO/ASTM 52900:2015). Frequently chosen method is the Fused Deposition Modelling (FDM) method suitable for thermoplastic materials. Its advantages include a wide choice of materials, good strength properties of the parts built, as well as a simple process model that affects the simple construction and thus low cost of FDM machines. Products shaped by AM technology are more and more often used as end-use parts or functional elements ready for assembly. Appropriate surface quality (Adamczak, 2008) and form-dimensional accuracy (PN-EN ISO 286-1: 2011) become very important and allow to eliminate the costs of finishing operations.

With the exception of universal requirements for the proper functioning, durability and reliability of the product, the desirable product properties, regardless of the technology, are mainly due to its intended use.

The quality of the product is therefore conditioned by the characteristics related to the individual desired properties, so quality level is formed by three main factors: (1) product design; (2) material; (3) parameters and conditions of the manufacturing process (Bähr and Westkamper, 2018).

1.1. Project phase

For both end-use parts and parts that are elements of assemblies, a set of characteristics consisting of the specification established in the design phase is important. These are geometrical features, surface topography, concerning topological aspects of surfaces and the structure of the surface layer. These three attributes of the correct part geometry have been extensively studied for parts manufactured in conventional subtractive processes, based mainly on machining. Material removal process has a strong influence on the topological and structural changes to machined surfaces. Irregularities and deformations of the machined surface occur due to the existence of cutting forces and friction of the cutting tool while machining.

Topography and surface texture is considered the most important geometric feature among the geometric quantities and parameters describing the surface structure after shaping (Petropoulos et al., 2010). As numerous works have found, the condition of surface could directly affect the functional features of the product. In Hashimoto et al. (2016), the influence of surface characteristics after four types of fine-finishing on functional characteristics, including tribological parameters and stress, was examined. The relationship between the state of the surface and wear resistance, sealing properties and corrosion resistance of parts and fatigue was concluded in Zabala et al. (2018).

With the appearance of new technologies like AM, there was

a necessity to verify these dependences.

The geometry of the parts fabricated in 3D printing processes, as opposed to machining, is created additively by adding material. In the FDM method, the surface condition with a characteristic texture is also formed by various phenomena accompanying the cooling process, affecting the properties, structure and thermal stress of the material.

Until recently, in industrial practice, surface texture was treated as an indicator of process variability (e.g., due to tool wear or machine vibration). In case of a stable process, Ra – the basic 2D parameter – characterizing the roughness and surface texture quite well. In practice, most surface roughness tests are still based on profile measurements and 2D parameters, which have been well recognized. As discussed by Guillemot et al. (2014), 2D parameters are an important indicators of product and process quality, but insufficient, for example, for complex surface texture or its anisotropy. Meanwhile, in the case of FDM method, the surfaces exhibit a clear anisotropic, nonuniform texture; therefore, the way of measurement should be chosen to fully characterize and describe them (Triantaphyllou et al., 2015).

Modern surface metrology is increasingly referring to spatial measurements (Guillemot et al., 2014; Mathiaa et al., 2011; Singh and Vatsalya, 2015) and topographic characteristics as surface descriptors, which represent the state of the entire surface, not just its cross-section.

The knowledge of relationships between 2D/3D parameters versus functional parameters of parts produced by finishing machining allows predicting and obtaining the products with improved functional properties (Grzesik, 2016). According to the author, the knowledge of topography can be employed for typical or unconventional processes to optimize the process settings or tools.

To summarize, in modern research, in the assessment of the quality of AM surfaces, three directions can be distinguished:
− determining the relationships between surface quality and desired surface function;
− selection and measurements of a representative characteristic or set of surface characteristics;
− optimization of process settings to establish the best surface quality.

Relatively little studies have been found in subject literature considering nothing except the issue of dimensional and form accuracy. These include the work by Spoerk et al. (2019), where the properties of (PP) semi-crystalline polypropylene composites processed by SLS method were analysed. A simplified stress deformation model has been developed for the purpose of warp analysis (Wang et al., 2007). In other studies, only certain geometrical features were inspected as one of the others quality indicators of FDM fabricated parts (Alsoufi and Elsayed, 2018; Nuñez et al., 2015; Tomić et al., 2017; Umaras and Tsuzuki, 2017).

1.2. Material and its composition

Material is an important factor affecting the quality of a product fabricated by AM technology. Building material (a filament) is used nowadays, instead of classical materials from the group of metals or ceramics, as a construction material, whose geometric (type and diameter of filament) and technological properties (high strength, combined with low density) depend on the geometrical and mechanical properties of the product. It is not easy to choose the best material to meet the construction and strength require-

ments in a given application, and at the same time, take this important aspect of product suitability into account.

Thermoplastic filament materials commercially available in the consumer market are fabricated commonly from acrylonitrile butadiene styrene (ABS), polypropylene (PP), polycarbonate (PC), polylactic (PLA), polyether (PEI), and others (Ligon et al., 2017). Traditional mono-plastics are now more and more often replaced with composites and nanocomposites. They are formed on the basis of a polymer matrix with the addition of inorganic fillers in order to improve their mechanical, optical, electrical and thermal properties. These can be glass fibres, carbon fibres, calcium carbonate, talc and many more. In recent years, progress at AM is mainly associated with the development of new materials that will enable 3D printing of parts with better mechanical performance and quality (Roberson et al., 2015).

The latest research trends towards developing techniques for the production of new fibre reinforced polymer composites (ranging from nanoscale discontinuous to continuous fibres) are described in (Duo Dong Goh et al., 2019). Recent achievements and technologies in this field are presented, as well as a list of materials with their advantages and disadvantages. Other current work in this field (Hofstätter et al., 2019) discusses the problems of composite production, the effect of fibre length, their orientation, the share of additives in polymer matrix on the composite properties and requirements for its processing. This publication also provides an overview of the materials currently available in fibre reinforced materials technology. The final desired properties of a composite depend on not only the properties of its components, but also many factors associated with its fabrication, which is why the development of an appropriate technology becomes an important problem that is analysed in many works. Mohan et al. (2017) makes an extensive review on the fabrication methods of specimens using various composite materials and optimization of their processing parameters in the FDM method to improve various mechanical properties and other desirable properties of 3D printed parts.

Carbon fibres are the common polymer additives. The importance of carbon fibres to additive manufacturing owes to such advantages as low weight, high tensile strength and low thermal expansion (Al-Hariri et al., 2016). Techniques for reinforcing polymers are presented in the paper, among others by using two separate printheads, the first of which dispenses the polymer, such as nylon or PLA, while the second the carbon fibres.

Blok et al. (2018) investigates the impact of carbon fibre architecture in composites on mechanical properties (tensile strength and stiffness) and so-called processability (including melt viscosity, temperature, thermal conductivity, and others).

As a result of the research (Kaczyński et al., 2014), the wear mechanism of thermoplastic composites reinforced with unidirectional carbon fibres was found to increase strength and wear resistance. The authors state the possibility of using the height of fibres reinforcing the polyamide matrix and their angle of orientation to predict the wear resistance. The authors (Prusinowski and Kaczyński, 2017) are investigating the possibility of achieving the desired properties through the use of an appropriate extrusion head design in the FDM method by orienting reinforcing carbon fibres of the appropriate length. Another work (Roberson et al., 2015) demonstrates the production of composite materials for AM based on FDM technology, aimed at obtaining the properties expected in given electromagnetic and electromechanical applications. It is also possible as authors state to reduce disadvantageous features such as anisotropy of mechanical properties, as

well as consideration of an important aspect of surface finishing.

Research is also ongoing regarding the usage of glass fibres in polymer matrix (Duo Dong Goh et al., 2019). Experiments involving a composite based on Nylon 6 with various admixtures of glass fibres, described in the study by Kumar and Panneerselvam (2016), reveal a significant increase in abrasion resistance as the fibres' content in the composite increased. Along with the glass fibres' share, the wear indicator decreases and is the lowest at 30% glass fibres. The addition of glass fibres also reduces plastic deformation, and its dispersion in the matrix improves tensile strength and hardness.

1.3. Material extrusion process

The final quality of the 3D printed object is also affected by the speed of extrusion, bed and printing head temperature, nozzle diameter, ambient temperature, and slicer parameters (algorithm forming layers of the model), such as wall thickness, type of filling and so on (Calcagnile et al., 2018; Mohan et al., 2017; Umaras and Tsuzuki, 2017). Taking into account such a large number of factors influencing the process, the preparation of test artefacts is a common practice (Knoop et al., 2018; Liua et al., 2019; Spoerk et al., 2019), on the basis of which, it is possible to carry out tests and determine the effect of processing condition on the quality of the products.

An important aspect of producing high quality products is the cost of obtaining it (Dudek and Zagórski, 2017). A way to reduce the costs of producing FDM products is to shorten processing time and minimalize material waste by applying the appropriate density of laid layers, known as the degree of infill density. This parameter is characterized by the amount of material inside the volume of the 3D printed model, so when completely filled with solid material, it occupies 100% of the volume; for empty (not filled with material), it is 0% (Loncierz and Kajzer, 2016).

The dynamic progress observed in the production of composite materials is often ahead of research, thanks to which one can comprehensively learn about the geometrical properties of an object affecting its functionality or appearance. Rapid changes in the composition, the innovations of polymer blends mean that with the development of new filament products, it is necessary to re-examine the manufactured part characteristics, hence predicting the accuracy – as some experts consider – is still an open issue. This problem particularly applies to commercial versions of materials, that is, filaments. There is a need to continuously broaden the knowledge on commercially available versions of composite materials (Hofstätter et al., 2019) and conducting research.

The aim of the published work was to experimentally investigate the geometrical properties of FDM manufactured parts. This paper describes the experiment of assessing the accuracy of test models with simple geometry made of three different commercial filaments. The choice of material should be made before designing the object, taking into account the desired properties of the object. Therefore, the influence that the material or the degree of infill density has on the chosen surface texture parameters of the specimen surface as well as on the shrinkage was investigated and compared.

2. EXPERIMENT

Three different materials were chosen for the study, which are currently of great interest to manufacturers of 3D printed products.

The first is a widely used traditional ABS polymer material, that is, acrylonitrile butadiene styrene, a completely amorphous material (http://www.rp-tech.pl; Nuñez et al., 2015; Żuchowska, 2000). Products made of this material are characterized by good mechanical properties and a wide range of temperatures of use. It is willingly chosen by manufacturers due to its ease of processing and relatively low price.

The next two are new composites: HDGLASS and NANOCARBON.

NANOCARBON is a polyamide (mainly PA12) with filling of carbon fibres. It is a partially crystalline composite material, characterized by excellent mechanical properties and very high chemical resistance thanks to the addition of fibres (www.markforged.com).

The third material, HDGLASS, is a new glass-like filament, made from an unique blend of PETG (polyethylene terephthalate), a material that is rapidly growing in popularity. Polymer matrix belongs to the group of polyesters that have a tendency to form a crystalline phase (www.formfutura.com). It is particularly interesting because detailed information based on scientific research carried out is not found about the properties of this material yet. The composite is characterized by 90% light transmission, high hardness and strength, as well as high resistance to high temperatures. The part 'HD' in the filament name means 'Heavy Duty'. Its additional advantage is the fact that it is suitable for contact with food (FDA certificate).

2.1. Material properties

Selected thermoplastic filament materials are characterized by different melting temperature and different thermal stability (Tab. 1), which can affect the state of the material after polymerization due to temperature reduction (cooling process).

Tab. 1. 3D printing filaments – Manufacturer's specification

Material type	ABS	NANOCARBON	HDGLASS
Colour	Brilliance black	Matte black	White
Filament Diameter [mm]	0.2	0.2	1.75
Melting Temperature (the temperature of the extruder) [ºC]	220 ÷ 290 (240 ÷ 270)	245 ÷ 265	215 ÷ 225 (PETG: 265)
Coefficient of Linear Thermal Expansion [m/m x °K]	7.38×10^{-5}	No data (PA12: $12 \div 14 \times 10^{-5}$)	No data (PETG: $8 \div 10 \times 10^{-5}$)
Density [g/cm^3]	1.03 ÷ 1.05	1.02 ÷1.24	1.270 (PETG:1.4)
Young's Modulus E [MPa]	1900 ÷ 2600	2700 ÷ 7600	2147.6
Tensile Strength Rm [MPa]	34 ÷ 51	41 ÷ 165	No data
The Temperature of Product Use [°C]	-40 ÷ 85	-30 ÷ 80	No data

2.2. 3D printer

The test specimens were made on the PRUSA ORIGINAL i3 machine, with working range 250x210x200 mm (Fig. 1a). It is one of the most popular printer models.
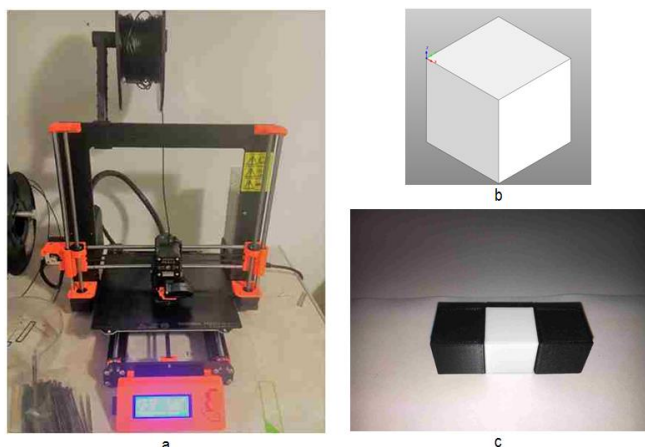
Fig. 1. Specimens manufacturing a) FDM machine; b) Printed model; c) Test specimens with different filament materials

According to users, this model combines good price with good print quality. The printer is equipped with a magnetic bed with the possibility of automatic levelling of the heating bed. The printer's advantages include a wide range of materials that can be used at work, from the most popular, such as ABS, to fibre reinforced composites.

2.3. Tested specimens

The specimens had the shape of a cube (Fig. 1b; Fig. 1c) with dimensions of 20x20x20 mm. The shape and dimensions of the tested specimens are important in determining mechanical properties while strength tests (Dikshit et al., 2017). Among many models, a cube was chosen as representing the simplest geometry, shortening time and facilitating the measurement and interpretation of results regarding geometric accuracy. For each material tested, three specimens were manufactured with a cross-fill rate (infill density) of 10%, 50% and 90%, which means that the material inside the cube, which forms the grid, occupies 10%, 50% or 90% of the internal volume. The 3D model was developed in Autodesk Inventor 2019 and then a G-Code was generated with Simplify 3D to control the printer. Tested specimens were printed at different extruder temperatures, bed temperatures and feed rates. The parameter values recommended by the machine manufacturer for the given material were used to ensure the correctness of process flow and good results. The levels of main process parameters are shown in Table 2.

Tab. 2. Factors settings of process 3D printing

Material	Nozzle temperature [°C]	Bed temperature [°C]	Printing speed [mm/s]
ABS	250	100	80
NANOCARBON	240	50	70
HDGLASS	210	90	65

The material consumption of each produced specimen was determined on the basis of weighing by AXIS electronic analytical balance. The device has a measuring range of 200 g and resolution 0.001 g. Table 3 below shows the average weight of three samples of each material.

Specimens were fabricated within two days at a constant am-bient temperature, using a filament from a single roll. They were then naturally cooled to room temperature of 25 ± 1°C.

Tab. 3. The specimens mass

Filament material/infill density	The average specimen mass 10^{-3}[kg]		
	10%	50%	90%
ABS	3.744	5.842	7.714
NANOCARBON	3.467	5.308	6.905
HDGLASS	4.826	7.254	9.449

All specimens were made with the same nozzle diameter. The thickness of the printing layer was set to 0.2 mm and was a constant for all specimens.

3. MEASUREMENTS

3.1. Measuring instrumentation stand

After the specimens were fabricated, the surface quality assessment was carried out on the basis of the chosen roughness parameters and areal surface parameters as well. Surface measurements were carried out using two methods: linear profiling (PN-EN ISO 4287: 2010; PN-EN ISO 4288: 1997) and spatial topography (ISO 25178-6:2011; Wieczorowski, 2013).
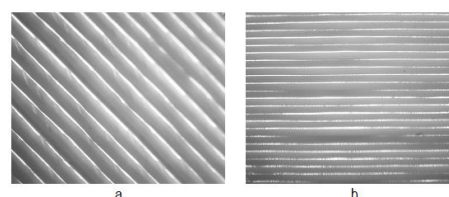

Fig. 2. Texture direction on: a) The top face of the cube; b) The side face of the cube

Figure 2 shows a microscopic representation of the structure of the upper face (a) and side face (b). The surface maps show typical traces of the specimen surfaces by positioning the strips of an extruded filament of a certain diameter and ovality. When applying one layer, a contour was created first and then the interior strips for each subsequent layer were rotated at 90 degrees from the previous arrangement. For the n-layer, the slope angle about the X-axis is –45°, and for the n+1-layer, the same angle is +45°. This arrangement of extruded filament strips shaped a surface with anisotropy texture character. This fact was taken into account in determining the cross-section of the analysed surfaces.

3.1. Profile roughness measurements (ISO 4285)

For roughness measurements using the profile method, FORMTRACER SV–C450 (Mitutoyo), a surface roughness/contour measuring system was used, equipped with a contact stylus (Fig. 3a). It has a measuring range of 800/800/8 um, straightness (0.5+0.001L) um, resolution 0.01/0.001/0.0001 um. Measurements were carried out on the upper surface, perpendicular to the direction of the extruded material path ('machining trac-

es'), and on each side of the cube perpendicular to the direction of the layers. Three measurements of roughness were taken on each surface except bottom face as it adheres to the base machine plate. During the profile assessment, the amplitude parameters were determined.
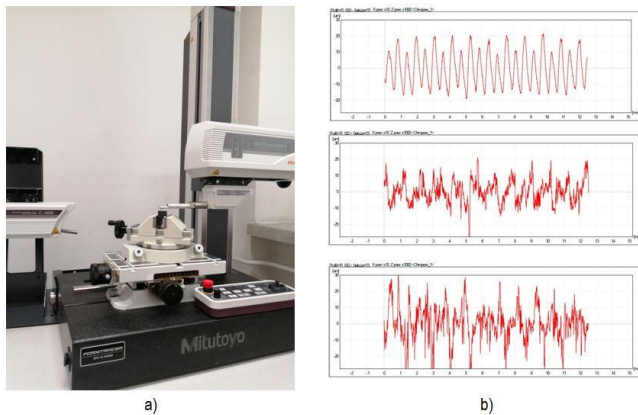

Fig. 3. Roughness measurement a) FORMTRACER SV–C450; b) Profiles of surface texture for three materials

Among others, R_a – an arithmetic mean deviation of the profile, R_q – mean square deviation of the profile, R_z – the highest height of the profile (Fig. 3b). The values of these parameters were then averaged. As a measure of the dispersion of the results obtained, the range, the difference between the largest and smallest values in the sample was considered.

3.2. Surface roughness measurements (ISO 25178)

Measurements of areal parameters were carried out using a contact instrument for measuring and analysing surface topography TOPO 01P IZTW, equipped with a rotational scanning table with 50x25 mm scanned area (Fig. 4a). The 3D parameters considered for analysis were following: S_a – an arithmetical mean height, S_q – root mean square height, S_z – maximum height of scale-limited surface.
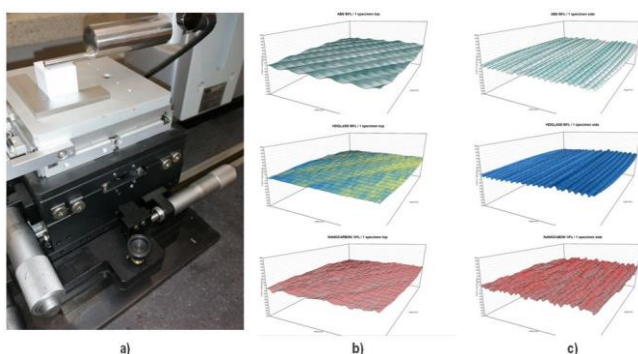

Fig. 4. Topography measurement a) Topo 01P profilometer, probe measurements range 250 um (S250 probe); b) Charts of surface texture of top faces; c) side faces

The measurements were performed on each surface except bottom side, as before. The obtained results – the graphs of surface topography – were analysed for top faces (Fig. 4b) and for side faces (Fig. 4c).

3.3. Geometric accuracy representation measurements

The dimensions and shape of the specimens had deformed due to shrinkage. There was a change in volume, created during cooling of polymeric materials and crystallization for semi-crystalline materials (Kwiatkowski and Kwiatkowska, 2012; Zawistowski, 2008).

The geometric–dimensional analysis was based on the measurements of specimen length as the distance between the central points of side walls in the X (1) and Y (2) directions and in the Z direction (3) – the direction of application of layers as the distance between the upper and bottom surface of the specimen. Mitutoyo 0.1/150 mm, MPe = 0.02 mm, the electronic calliper was used for measurements. The accuracy measure were deviations of the dimensions observed from the dimensions of the programmed model. The results of the measurements were averaged for each test case and the range in the observed values was taken as a measure of dispersion.

4. RESULTS

The experimental scenario excluded a comparative analysis of the results obtained, because the specimens were not formed in equivalent processes. For each series of three specimens, the optimal, but slightly different, set of process parameters for the specified material was applied. Furthermore, different measuring instruments were used to measure the specimens and the surface texture parameters were determined by their (different) software. Therefore, the obtained data do not meet the conditions of repeatability necessary for traditional analysis.

The analysis, therefore, focused on the comparison of the degree to which materials react to the phenomena of surface texture formation and the phenomenon of shrinkage, a fundamental issue, for example, in plastics processing.

In the publication, one restrained to presenting only two but commonly used parameters, that is, R_a and S_a.

Parameter R_a – arithmetical mean deviation of the assessed profile – is an arithmetic mean of the absolute ordinate values z(x) within a sampling length l (1).

$$R_a = \frac{1}{l}\int_0^l |z(x)|dx. \tag{1}$$

For the characterisation of surface texture, the areal parameter S_a was used (2), that is, an arithmetic mean of the absolute of the height within a definition area (A).

$$S_a = \frac{1}{A}\iint_A |z(x,y)|dxdy. \tag{2}$$

Unlike in other processes using thermoplastic materials, for example, during injection moulding, it was not possible to determine the processing shrinkage as a share of the product volume in the volume of the injection mould used to make it. In this paper, deviations δ from the dimension imposed by the design were analysed and linear (longitudinal) shrinkage was calculated according to Formula (3).

$$S_l = \frac{l_o - l}{l_o} = \frac{\delta}{l_o} \tag{3}$$

where: S_l – the value of the deviation in the selected direction (x, y, z), l_o–length of the model in the selected direction, l – observed dimension.

Halina Nieciąg, Rafał Kudelski, Piotr Dudek, Jacek Cieślik
An Exploratory Study on the Accuracy of Parts Printed in FDM Processes from Novel Materials

DOI 10.2478/ama-2020-0009

4.1. Roughness of surface texture

The differences in roughness are illustrated by the graphs of the R_a parameter (1), for the side faces (Fig. 5a) and upper faces of the specimens (Fig. 6a).

The graphs show that the roughness and topography of the side faces (Fig. 5a) for a specific material are stable for different degrees of infill density and the values of the surface texture parameters are slightly differentiated. The highest values have been noticed for NANOCARBON composite and the lowest values for HDGLASS.
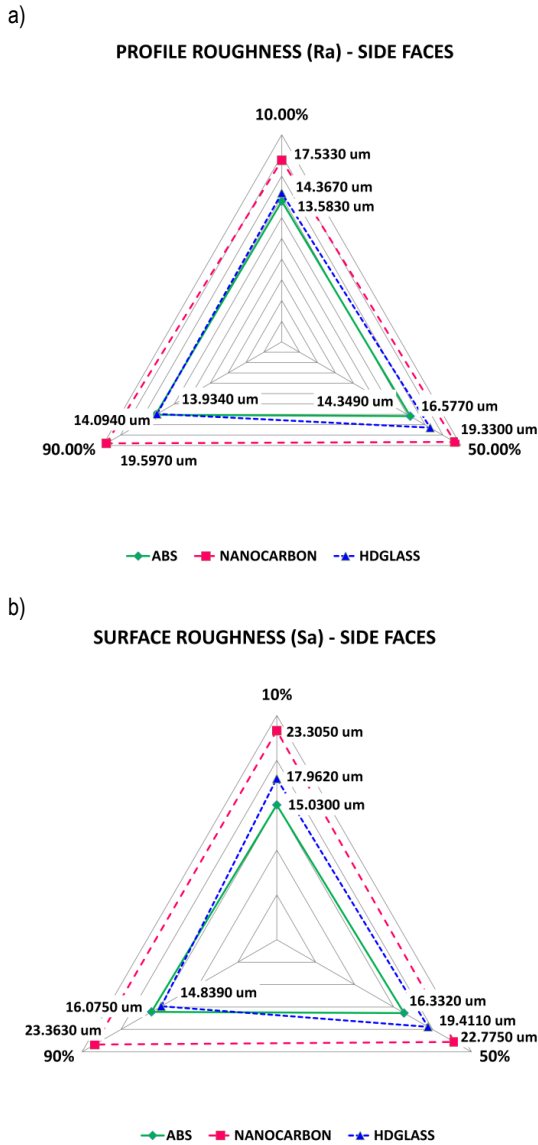
a)

Fig. 5. Roughness parameters versus infill density (%) for side faces:
a) Ra [um]; b) Sa [um]

A similar relation can be observed when analysing the upper surface on which the layers have been laid. The NANOCARBON surface turned out to be the least smooth, while for the remaining two materials (ABS and HDGLASS), the measured surface irregularities were smaller. This is probably due to the presence of carbon fibres in the NANOCARBON material, which produce a roughness effect felt by the fingers.
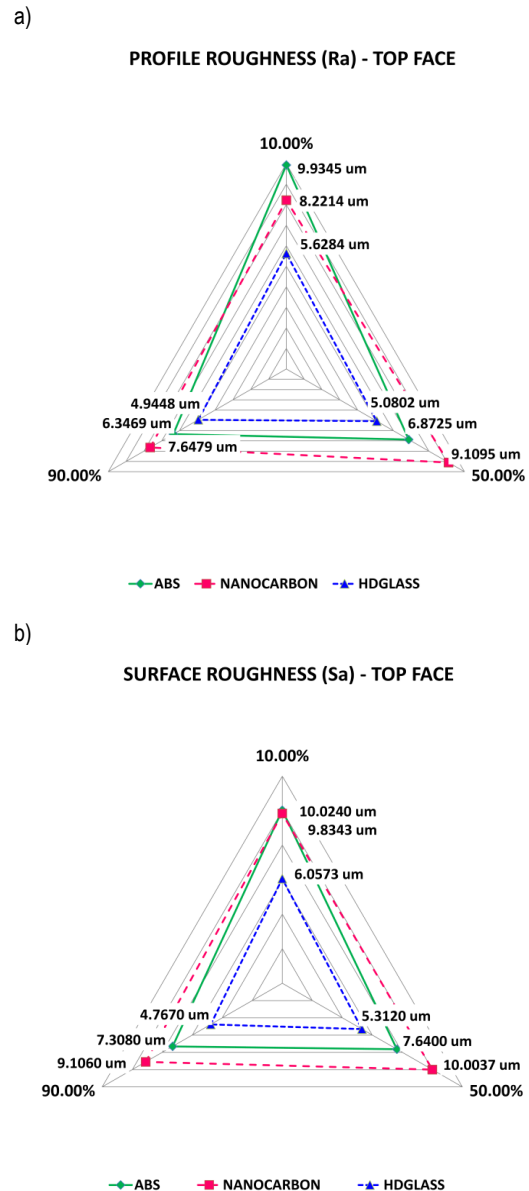

Fig. 6. Roughness parameters versus infill density (%) for top faces
a) Ra [um]; b) Sa [um]

The view of intensity images captured by Marsurf CM Expert focus microscope show the difference between surface structures of the two composites (Fig. 7). There was a large difference between the surface texture parameters of the side faces and the upper face, which was much less uneven. The biggest difference was observed for HDGLASS composite.

However, additionally, an interesting observation was the different effect of the infill density on the roughness of the materials. HDGLASS material was characterized by similar R_a values, regardless of the infill density, and the ABS material turned out to be the most sensitive to the infill density (increasing the level of infill density from 10% to 90% reduces the R_a parameter about 1.6 times).

The topography of the surface was also evaluated on the basis of amplitude areal parameter (2), for the side faces (Fig. 5b) and upper faces of the specimens (Fig. 6b). The values in relation to the profile parameters were generally higher, which could be a consequence of the enlargement of the area (surface areas) for

which they were determined, that is, the fact that the measurement of the profile did not take into account any irregularities situated outside the chosen cross-section.

However, the ratio of the values of surface parameters to profile parameters was different for the three materials. For NANOCARBON material, the surface parameters were about 19% higher than the profile parameters; for other materials, the differences were smaller (for ABS did not exceed 15%, for HDGLASS was less than 10%).
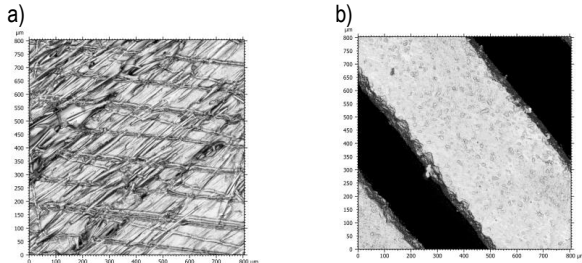

Fig. 7. Intensity image of: a) NANOCARBON; b) HDGLASS

The graph in Figure 8 illustrates an important argument proving the validity of multi-parametric evaluation by extending the set of profile parameters by 3D parameters of surfaces shaped in the FDM technology.
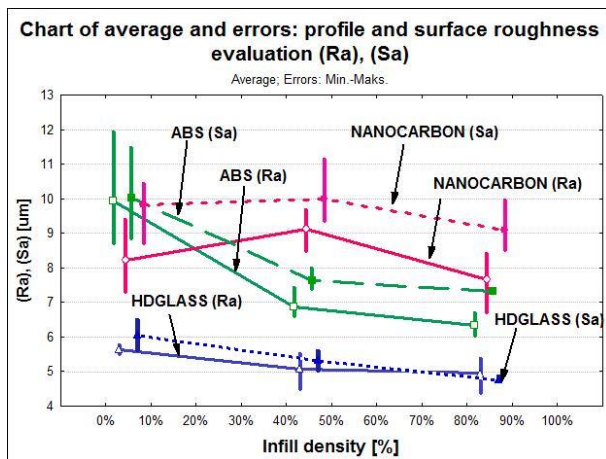

Fig. 8. Summary analysis results of profile and surface roughness measurements for the three types of filament material

The observation of the curves shows that in all the studied materials, the profile evaluation results in a larger dispersion of parameters, while the spatial parameters have a smaller dispersion. The dispersion characterizes in fact the actual variation of irregularities of the surfaces due to factors such as unstable values of process parameters. The smallest change in process parameters may lead to a change in product properties, but noticeably higher values of profile parameters range in relation to spatial parameters spread may be the result of the method of measurement and imprecise determination of the direction of measurement of the texture having clear anisotropy features.

4.2. Dimensional deviations by thermal affects

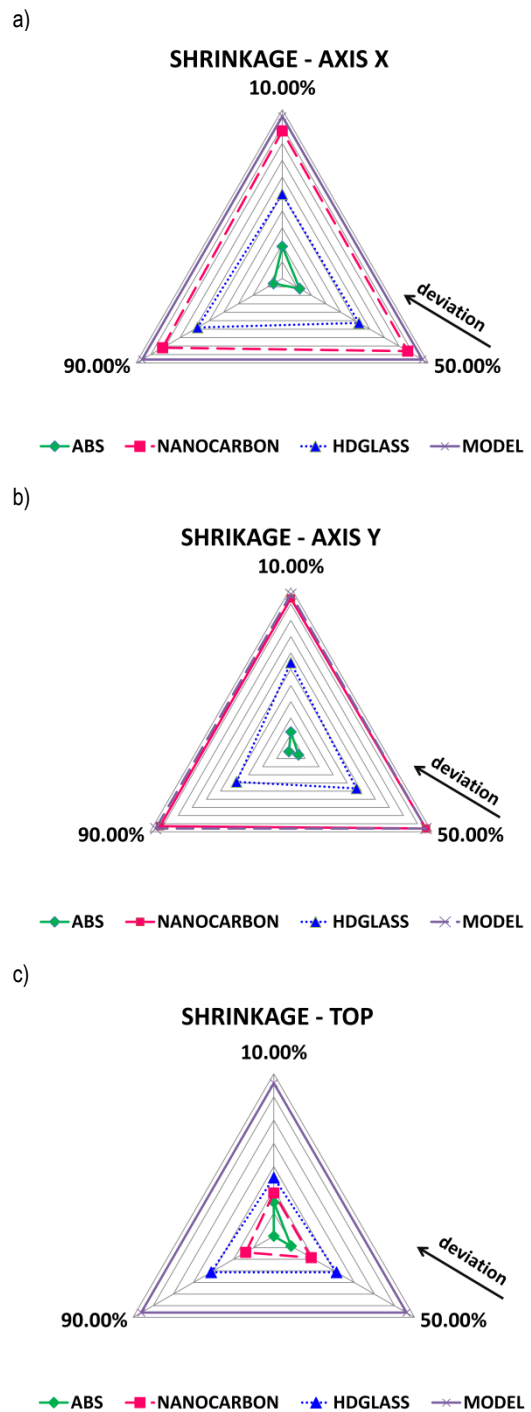The measured dimensional deviations are shown in the diagrams in Fig. 9 and Fig. 10.

Fig. 9. Effect of type of filament material on thermal deviations δ [mm] for: a) X axis; b) Y axis; c) Z axis

As the dimensions of the 3D model are the same for all specimens, they represent the same tendency as linear shrinkage (3).

The dimensional deviations of the side surfaces for composite materials are evenly distributed in X, Y and Z directions (all three axes of the printer) for all density levels. The situation is different with ABS material. In accordance with the tendency for processing shrinkage reported by Nuñez (2015), the specimens made of this material were characterized by negative dimensional deviations on the lateral surfaces and at the same time, there was seen a visible dependence of shrinkage on the infill density. At 90% level (in case of almost full model), the dimensional accuracy deter-

Halina Nieciąg, Rafał Kudelski, Piotr Dudek, Jacek Cieślik
An Exploratory Study on the Accuracy of Parts Printed in FDM Processes from Novel Materials

DOI 10.2478/ama-2020-0009

mined by a negative deviation from the model dimension is the worst. For the highest density of the upper surface, the linear contraction was almost 0.73%.

a)

b)

c)

Fig. 10. Effect of infill density on thermal deviations δ [mm] for: a) ABS; b) NANOCARBON; c) HDGLASS

The diagrams in Figure 9 show how deviations for individual materials were distributed in directions. The anisotropy of ABS plastic deviations in relation to the tested directions (machine axes) was distinguished.

The analysis of dimensional deviations also shows a special effect of 50% infill density in case of ABS deviations. This degree of infill density results in the greatest change in the size and surface texture parameters. For composite materials, the changes of geometric form were found to have more anisotropic character.

5. DISCUSSION

It should be noted that the research was concerned with two groups of materials: amorphous thermoplastic and composites based on semi-crystalline material matrix. Investigating the material properties but in another process, that is, injection moulding process (Kwiatkowski and Kwiatkowska, 2012; Zawistowski, 2008), the authors drew that thermoplastics, partly crystalline (1÷5%), have higher shrinkage values, while amorphous thermoplastics (0.3 ÷ 1%) have smaller ones, which could be explained by the arrangement of macromolecules of the structure, denser than for amorphous plastics.

However, the studies presented in this publication prove that the addition of fibres to the polymeric matrix changes this relation and improves some geometric properties of the product, as was a case with HDGLASS. The improvement consists in the reduction of shrinkage, more even distribution of shrinkage values, as well as surface texture parameters in relation to the infill density and direction, additionally in the case of composites with the addition of glass fibres, and also in the reduction of surface irregularities.

The mechanism of improving the properties of composites is complex and difficult to explain without an analysis of physical and thermal phenomena accompanying the thermoplastic materials processing. It is determined by various factors, physicochemical and viscoelastic properties. The influence of inter-phase interactions between polymer chains and fibres (Barczewski et al., 2012; Gołębiowski, 2004) and the formation of new chemical bonds is also considered.

The processes of additive fused deposition for amorphous and semi-crystalline plastics are not homogeneous. Application of ABS layers requires a plastic state: viscous. Depending on the viscosity, the material is integrated along the extruder paths. Within the active layer applied, macromolecules may still partially move. As a result, the shaped surface does not reproduce the filament stripe contours because they are blurred. The resulting irregularities – in accordance with the course of the process – will depend on its parameters: among other things, the feed rate (pathway adhesion surface) and temperature reduction rate.

The process of applying layers has a different effect on the phenomenon of shrinkage.

ABS material remains amorphous in the solid state also after exceeding the glass transition temperature, T_g (Żuchowska, 2000). From the moment T_g is exceeded until the product reaches the ambient temperature, the product undergoes thermal shrinkage as a solid object. This process takes place layer by layer. The highest, near-surface layers may still be in the glass transition state, which is characterized by elasticity (characteristic for amorphous polymers), while the lower layers may already be solidified; therefore, in the cross section of the product, there are inner stresses that may simultaneously lead to contour deformations of the product such as buckling.

In the polymer matrix of composites, when the T_k crystallisation temperature is exceeded, solidification occurs by ordering the molecules and forming crystallites. These semi-crystallisation materials are characterized by the lack of elastic phase, but between T_k temperature and melting temperature, cold crystallization can occur.

The examined properties of HDGLASS composite can be then attributed to the conditions of the cooling process. The addition of glass fibres to the main polymer matrix groups hinders the free
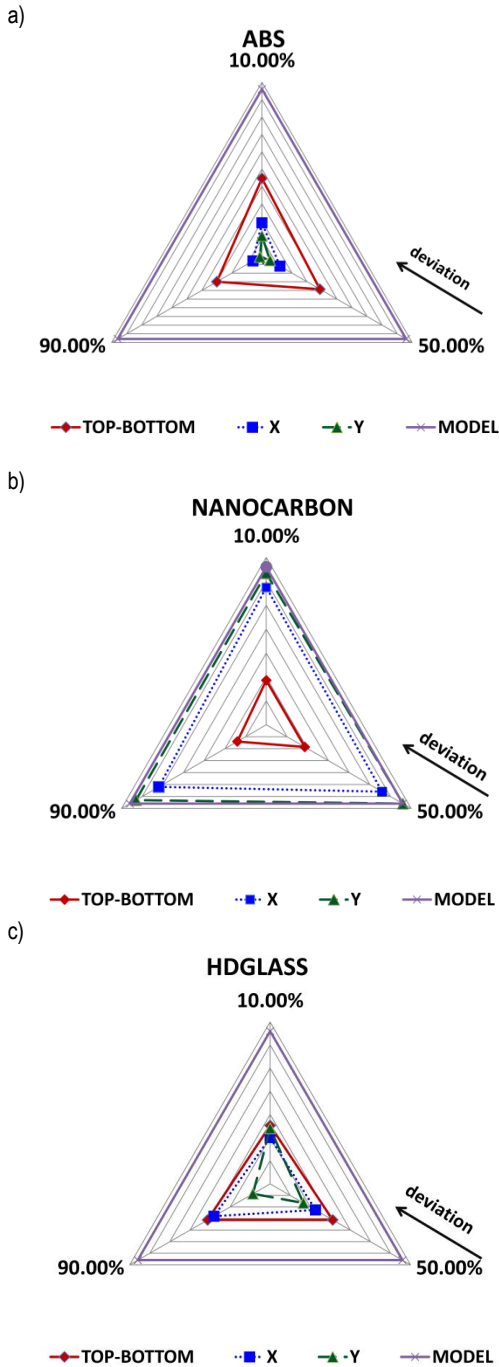
movement of macromolecules, affect nucleation and growth of primary crystalline structures and then promotes the formation of a fully developed crystalline structure with the same cooling rate as in homogeneous plastics.

6. CONCLUSIONS

The obtained results can have a cognitive and utilitarian character. The practical aim of the research was to determine the material on the basis of test specimens' measurements, whose properties and application method allow to obtain products of the best quality.

− It was found that the quality of products shaped by FDM technology depends on the type of filament used for building as on the infill density.
− On the process completion, all the printed specimens reduce their volume during cooling, but not equally. The smallest linear shrinkage was found in NANOCARBON specimens, the largest in ABS. The best results were obtained for HDGLASS with an infill density of 90%.
− The description of surface texture with areal parameters gives higher estimates of spatial features. The highest diversity of analysed roughness as well as areal parameters was observed for NANOCARBON.
− The heterogeneous structure of surfaces shaped with the FDM method requires multiparametric evaluation, which was achieved by using two methods of analysing the surface irregularities that together characterize the tested specimens.
− Modification of thermoplastic filament materials by adding fibres may improve not only their mechanical but also geometrical properties of the fabricated parts. The composites studied were characterized by higher resistance to thermal phenomena and smoother surface than ABS monoplastic.
− Further exploring the processability of composites are planned among others by employing thermal analysis.
− Our exploratory research, thanks to the initial recognition of the problem, will allow us to determine the best research project on evaluate of geometric quality of parts fabricated from HDGLASS and NANOCARBON composites.

REFERENCES

1. **Adamczak S.** (2008), *Surface geometric measurements – in Polish*, WNT, Warszawa.
2. **Al-Hariri L. A., Leonhardt B.**, **Nowotarski M., Magi J., Chambliss K., Venzel T., Delekar S. and Acquah S.** (2016), Carbon Nanotubes and Graphene as Additives in 3D Printing. Carbon Nanotubes, *Current Progress of their Polymer Composites*, 221–251, https://scholarworks.umass.edu/chem_faculty_pubs/1448.
3. **Alsoufi M. S., Elsayed A. E.**, (2018), Surface Roughness Quality and Dimensional Accuracy - A Comprehensive Analysis of 100% Infill Printed Parts Fabricated by a Personal/Desktop Cost-Effective FDM 3D Printer, *Materials Sciences and Applications*, 9, 11–40.
4. **Bähr F., Westkamper E.** (2018) Correlations between Influencing Parameters and Quality Properties of Components Produced by Fused Deposition Modeling, *Procedia CIRP*, 72, 1214–1219.
5. **Barczewski M., Chmielewska D., Sterzyński T., Andrzejewski J.** (2012), The assessment of properties of nucleated isotactic polypropylene modified with silsesquioxanes – in Polish, *Przetwórstwo Tworzyw*, 5, 409–413.
6. **Blok L. G., Longana M. L., Yu H., Woods B. K. S.** (2018), An investigation into 3D printing of fibre reinforced thermoplastic, *Additive Manufacturing*, 22, 176–186.
7. **Calcagnile P., Cacciatore G., Demitri C., Montagna F. and Corcione C. E.** (2018), Fused Deposition Modeling 3D PrinterA Feasibility Study of Processing Polydimethylsiloxane–Sodium Carboxymethylcellulose Composites by a Low-Cost Fused Deposition Modeling 3D Printer, *Materials*, 11, 1578, 1–14.
8. **Dikshit V., Nagalingam A., Yap Y. L., Sing S. L., Yeong W. Y. and Wei J.** (2017), Investigation of quasi-static indentation response of inkjet printed sandwich structures under various indenter geometries, *Materials*, 10 (3), 290, 1–18.
9. **Dudek P., Zagórski K.** (2017), Cost, resources, and energy efficiency of Additive Manufacturing, *E3S Web of Conferences*, ISSN 2267-1242, 14, 1–8.
10. **Duo Dong Goh, Yee Ling Yap, Shweta Agarwala, and Wai Yee Yeong** (2019), Recent Progress in Additive Manufacturing of Fiber Reinforced Polymer Composite, *Adv. Mater. Technol.*, 4, WILEY-VCH Weinheim, 856–863.
11. **Gołębiowski J.** (2004), Polymer nanocomposites. Structure, synthesis and properties – in Polish. *Przemysł Chemiczny*, 83, 1, 15–20.
12. **Grzesik W.** (2016), Prediction of the Functional Performance of Machined Components Based on Surface Topography: State of the Art, 25(10), 4460–4468.
13. **Guillemot G.,Bigerelle M., and Khawaja Z.** (2014), 3D Parameter to Quantify the Anisotropy Measurement of Periodic Structures on Rough Surfaces, *Scanning*, 36, 127–133.
14. **Hashimoto F**. (2016), Characteristics and Performance of surface created by various finishing methods, *Procedia CIRP*, 45, 1–6.
15. **Hofstätter T., Pedersen, Bue D., Tosello G., Nørgaard H.** (2019), State-of-the-art of fiber-reinforced polymers in additive manufacturing technologies, *Journal of Reinforced Plastics & Composites*, 36(15), 1061–1073.
16. **ISO/ASTM 52900:2015**, Additive manufacturing – General principles – Terminology.
17. **Kaczyński R., Wilczewska I., A. Sfiridienok** (2014), Peculiarities of the wear mechanism of polymers reinforced with unidirectional carbon fibers, *Friction and Wear*, 35 (6), 449–454.
18. **Knoop F., Kloke A., and Schoeppner V.** (2018), Quality improvement of FDM parts by parameter optimization, *AIP Conference Proceedings*, 190001-1–190001-5.
19. **Kumar S., Panneerselvam K**. (2016), Two-body Abrasive Wear Behavior of Nylon 6 and Glass Fiber Reinforced (GFR) Nylon 6 Composite, *Procedia Technology*, 25 (2016) 1129–1136.
20. **Kwiatkowski D., Kwiatkowska M.** (2012), Numerical analysis of volume shrinkage of polyacetal composites with glass fibre – in Polish, *Przetwórstwo Tworzyw*, 5, 452–455.
21. **Ligon S.C., Liska R. ,Stampfl J., Gurr M. and Mulhaupt R**. (2017), Polymers for 3D Printing and Customized Additive Manufacturing, *Chemical Review*, 117, 10212−10290.
22. **Liua Z., Lei Q., Xinga S.** (2019), Mechanical characteristics of wood, ceramic, metal and carbon fiber-based PLA composites fabricated by FDM, *Journal of Materials Research and Technology*, 8(5), 3741–3751.
23. **Loncierz D., Kajzer W. (2016),** Influence of 3D printing parameters in the FDM technology on mechanical and utility properties of objects made of PLA – in Polish, *Aktualne Problemy Biomechaniki*, No. 10, 43–48.
24. **Mathiaa T. G., Pawlus P., Wieczorowski M**. (2011), Recent trends in surface metrology, *Wear*, Vol. 271, No. 3–4, 494–508.
25. **Mohan N., Senthil P., Vinodh S. & Jayanth N.** (2017), A review on composite materials and process parameters optimisation for the fused deposition modelling process, *Virtual and Physical Prototyping*, Vol. 12, No. 1, 47–59.
26. **Nuñez P. J., Rivas A., García-Plaza E., BeamudE., Sanz-Lobera A.** (2015), Dimensional and surface texture characterization in Fused Deposition Modelling (FDM) with ABS plus, The Manufactur-

ing Engineering Society International Conference MESIC 2015, *Procedia Engineering ,*132, 856–863.

27. **Petropoulos G., Pandazaras C. N., Davim P.** (2010), Surface Texture Characterization and Evaluation Related to Machining. Surface Integrity in Machining, *Springer*, 37–66.

28. **PN-EN ISO 25178-6** (2011), Geometrical product specifications (GPS) — Surface texture: Areal — Part 6: Classification of methods for measuring surface texture – in Polish.

29. **PN-EN ISO 286-1** (2011), Geometrical product specifications (GPS) – ISO code system for tolerances on linear sizes – Part 1: Basis of tolerances, deviations and fits – in Polish.

30. **PN-EN ISO 4287:1999/A1** (2010), Geometrical Product Specifications (GPS) - Surface texture: Profile method - Terms, definitions and surface texture parameters – in Polish.

31. **PN-EN ISO 4288** (1997), Geometrical Product Specifications (GPS) — Surface texture: Profile method — Rules and procedures for the assessment of surface texture - in Polish.

32. **Prusinowski A., Kaczyński R.** (2017), Simulation of processes occurring in the extrusion head used in additive manufacturing technology, *Acta Mechanica et Automatica,* 11 (4), 317–321**.**

33. **Roberson D.A., Shemelya C. M., MacDonald E., Wicker R. B.** (2015), Expanding the Applicability of FDM-type Technologies Through Materials Development, *Rapid Prototyping Journal*, 21 (2),137–143.

34. **Singh R., Vatsalya** (2015), Evolution of 3D Surface Parameters: A Comprehensive Survey**,** *The International Journal of Engineering and Science*, 4 (2), 4–10.

35. **Spoerk M., Holzer C., Gonzalez-Gutierrez J**. (2019), Material extrusion-based additive manufacturing of polypropylene: A review on how to improve dimensional inaccuracy and warpage, *J. Appl. Polym. SCI*, DOI: 10.1002/app.48545, 1–14.

36. **Tomiċ D., Fuduriċ A., Mihaliċ T., Simuniċ N.** (2017), Dimensional accuracy of prototypes made with FDM technology, *Journal of Energy Technology*, 2, 51–59.

37. **Triantaphyllou A., Giusca C., Macaulay G., Roerig F. , Hoebel M., Leach R., Tomita B., Milne K.** (2015), Surface texture measurement for additive manufacturing, *Surface Topography: Metrology and Properties*, 3, 1–8.

38. **Umaras E.,Tsuzuki M. S. G**. (2017), Additive Manufacturing - Considerations on Geometric Accuracy and Factors of Influence**,** *IFAC PapersOnLine*, 50 (1), 14940–14945.

39. **Wang T.- M., Xi J.-U., Jin Y**. (2007), A model research for prototype warp deformation in the FDM process, *The International Journal of Advanced Manufacturing Technology*, 33, 1087–1096.

40. **Wieczorowski M.** (2013), Theoretical basis of spatial analysis of surface asperities – in Polish, *Inżynieria Maszyn,* 18(3), 7–34. **www.formfutura.com** (access 07.09.2019).

41. **www.markforged.com** (access 07.09.2019).

42. **www.rp-tech.pl** (access 07.09.2019).

43. **Zabala A., Blunt L.,** *Wilson* **W., Aginagalde A., Gomez X. and Mondragon I. L.** (2018), The use of areal surface topography characterisation in relation to fatigue performance, *MATEC Web of Conferences*, 165, 1–6.

44. **Zawistowski H.** (2008), Basics of the theory of shaping the properties of products in the process of injection of thermoplastics – in Polish, *Mechanik*, 4, 274–280.

45. **Żuchowska D.** (2000), *Constructional polymers* – in Polish, WNT, Warszawa